

Nanoscale Lithography and Thermometry with Thermal Scanning Probes

THÈSE N° 9060 (2018)

PRÉSENTÉE LE 14 DÉCEMBRE 2018

À LA FACULTÉ DES SCIENCES ET TECHNIQUES DE L'INGÉNIEUR
LABORATOIRE DE MICROSYSTÈMES 1
PROGRAMME DOCTORAL EN MICROSYSTÈMES ET MICROÉLECTRONIQUE

ÉCOLE POLYTECHNIQUE FÉDÉRALE DE LAUSANNE

POUR L'OBTENTION DU GRADE DE DOCTEUR ÈS SCIENCES

PAR

Samuel Tobias ZIMMERMANN

acceptée sur proposition du jury:

Prof. L. G. Villanueva Torrijo, président du jury
Prof. J. Brugger, directeur de thèse
Prof. F. Perez-Murano, rapporteur
Dr A. Knoll, rapporteur
Prof. V. Subramanian, rapporteur



ÉCOLE POLYTECHNIQUE
FÉDÉRALE DE LAUSANNE

Suisse
2018

To my parents...

Acknowledgements

I am deeply grateful to Prof. Jürgen Brugger for giving me the opportunity to do a PhD in his group and providing me with his support, time and trust to work on different interesting subjects, which broadened my horizon.

I am indebted to Dr. Giovanni Boero for many discussions, his helpful advice and for correcting parts of the thesis manuscript. I truly admire his deep passion for science and physics in particular, which has clearly rubbed off on me over time.

It has been an invaluable experience to be part of a great team of highly motivated, skilled and good-hearted people. Therefore, I would like to thank all current members of LMIS1 for their help and all the good moments we spent together. I would like to thank, in particular, Henry Shao-Chi Yu who fabricated the microwave antennas for me in the clean room when my time became sparse in the last year of the thesis, Ya Wang for showing me how to extract silk fibroin from cocoons, Chris Tse for taking pictures of the thermometry setup and Lorenz Hagelücken for German spellchecking.

Furthermore, I would like to thank Dirk Balkenende, Anna Lavrinova and Prof. Chris Weber from the Adophe Merkle Institute at the University of Fribourg for the fruitful collaboration with the supramolecular polymer. I am very grateful for the AFM force spectroscopy measurements and the fluorescence images which were taken by Anna and Dirk.

I would also like to thank the staff from the Center of MicroNanoTechnology (CMi) and the Atelier de l'Institut de Microtechnique at EPFL for their excellent services.

Over the course of my doctorate, I had the pleasure to supervise six extremely motivated students, who assisted me in the advancement of my experiments. I would like to thank Biwei Zhang, Vincent Paratte, Pierre Chevalier, Pascal Oberholzer, Aleksandra Markovic (dry-etching of silk fibroin) and Nikita Rudin for their invaluable effort.

I would like to warmly thank Prof. Christian Degen from ETH Zürich for his advice in the planning phase of the optical setup and sharing information about his tools.

I am also deeply grateful to Prof. Emer. Franz-Karl Reinhart from EPFL, who advised me in his free time in the initial phase of building the optical setup for thermometry measurements.

Special thanks go to Qiyuan Jang, who worked with me over more than half a year on the optical setup.

Acknowledgements

I would like to thank the SwissLitho team for their excellent support on our thermal scanning probe tool and for organizing the legendary Thermal Probe Workshop. In particular, I'd like to thank Colin Rawlings for providing me his comprehensive source code for simulating resistively-heated thermal probes. I would like to thank also Felix Holzner, Philip Paul, Simon Bonnani and Martin Spieser for many discussions throughout my PhD.

Over the course of my doctorate I made an extensive use of excellent free software (free as in freedom) and open-source programs, such as: Gimp, Inkscape, Python (including many packages), FEniCS, rStudio, LibreOffice, Blender and many more. I would like to acknowledge the work of all these outstanding people who are contributing in developing free and open software tools.

In June 2018 shortly before my thesis submission, I suffered from a foot injury during climbing, which considerably reduced my mobility for more than six weeks. I would like to thank orthopedist Dr. Pagano from Morges and the physiotherapists at Dino in Renens, who supported me in recovering from the injury as fast as possible, which allowed me to conduct the last experiments in the lab.

During my PhD a colleague suspiciously often was throwing paper balls at me. That's how I met my true love Kaitlin Howell. I would like to deeply thank her for many discussions about my research and for proof reading all chapters and manuscripts. Especially, I would like to thank her for taking so good care of our home during the intensive thesis writing phase despite her own tight schedule.

Last but not least, I would like to thank my parents Erika and Heinrich Zimmermann for their endless support during all my studies. Without them, I would not have reached this far.

Lausanne, November 23, 2018

Samuel Zimmermann

Abstract

Thermal scanning probe lithography (t-SPL) is an advanced lithography technique in which a heated atomic force microscope tip locally modifies a sample material. Due to the nanometer-sized tip apex diameter, t-SPL enables patterning of sub-10 nm structures at a low cost compared to electron beam or extreme ultraviolet lithography techniques. In the first part of this dissertation, two novel materials are investigated as a resist for t-SPL, which have in common that fast heating and cooling rates are required to modify them.

The first material is a fluorescent supramolecular polymer, which exhibits thermoresponsive luminescence due to reversible aggregation of excimer-forming fluorophores. At temperatures above 180 °C under ultraviolet light, the material fluoresces in green. When the polymer is cooled down to room temperature, a spectral shift towards red emission takes place due to aggregation of the fluorescent moieties. Unlike at the macroscale, where the fast aggregation of the fluorophores prevents kinetical trapping of the green fluorescent high-temperature state, the heating and cooling rates (on the order of 10^8 K/s) accessible by t-SPL are fast enough to freeze the green fluorescent state. The thermomechanical properties of the supramolecular glass are analyzed by nanoindentation with a heated probe and the self-healing behavior of the material is used to selectively write and erase indents. It is demonstrated that t-SPL patterning enables the fabrication of topographical and fluorescent structures with interesting properties.

The second material is silk fibroin, a protein extracted from silk produced by the larvae of *Bombyx mori* moths or certain spiders. Silk fibroin exhibits at least two polymorphic structures with different water-solubility. In this work, water-insoluble silk fibroin thin films are fabricated by spin coating and immersion in ethanol. During t-SPL patterning of the films, local heating of silk fibroin at high heating rates induces water-solubility. The resolution and line edge roughness are compared to the molecular size of the resist, which poses the ultimate resolution limit. In addition, grayscale lithography with silk is demonstrated. Silk fibroin is also explored as a resist for dry etching by demonstration of a pattern transfer from t-SPL fabricated patterns into silicon oxide.

A second part of the thesis concerns the planning and assembly of a setup for nanoscale thermometry in combination with thermal scanning probes as well as implementation of the necessary software. The construction of a dedicated setup to perform nanometer scale thermometry at the tip of a cantilever is motivated by the difficulty to measure

Acknowledgements

or calculate the temperature at the tip during operation. Among many nanoscale thermometry techniques, fluorescence-based thermometry using nanodiamonds with nitrogen vacancy defects has been evaluated as promising. The components and the assembly of the setup, consisting of a excitation laser, an inverted optical microscope, a single photon detector and stages for scanning, are described and discussed. Initial results of thermometry with micrometer particles are presented and measurements with nanoparticles on a heated tip are shown. Good agreement with experiments from literature was found.

Keywords: Thermal Scanning Probes, Grayscale Lithography, Supramolecular Polymer, Silk Fibroin, Nanoscale Thermometry, Nitrogen Vacancy Center, Nanodiamonds

Zusammenfassung

Thermische Rastersondenlithographie (TRSL) ist eine fortgeschrittene Fabrikationstechnik, bei welcher mit einer geheizten Rasterkraftmikroskopspitze ein Material lokal verändert wird. Die scharfe Spitze in der Größenordnung von wenigen Nanometern ermöglicht es, TRSL-Strukturen in Materialien mit einer Auflösung von weniger als zehn Nanometern zu schreiben. Dank dem relativ einfachen Aufbau eines TRSL-Geräts sind die Anschaffungskosten im Vergleich zu einem Elektronen-Raster-Scan-Lithographie-Gerät oder Extrem-Ultraviolett-Lithographie-Gerät gering.

Im ersten Teil dieser Dissertation werden zwei neuartige Resistmaterialien für TRSL untersucht. Eine Gemeinsamkeit beider Materialien ist, dass die Kontrastbildung durch die hohen Heiz- und Kühlraten, welche mit dem TRSL-Gerät erzeugt werden können, ermöglicht wird.

Das erste Material ist ein fluoreszierendes supramolekulares Polymer, welches eine thermisch-induzierte Änderung der Fluoreszenz aufweist, die durch reversible Aggregation von Excimer-formenden Fluorophoren hervorgerufen wird. Bei Temperaturen über 180 °C emittiert das Material im grünen Spektralbereich unter Belichtung von ultraviolettem Licht. Wenn das supramolekulare Material auf Raumtemperatur abgekühlt wird, verschiebt sich die spektrale Emission in den roten Bereich aufgrund der Aggregation der fluoreszierenden Moleküle. Bei Kühlraten, welche in der makroskopischen Größenordnung erzielt werden können, haben die Moleküle genügend Zeit um sich von der Hochtemperaturphase anzuordnen, sodass das Material bei Raumtemperatur immer eine rote Emission aufweist. Es hat sich jedoch gezeigt, dass aufgrund kleiner thermisch veränderter Volumina in TRSL die Kühlrate (10^8 K/s) ausreicht, um den grün fluoreszierenden Zustand einzufrieren.

Das zweite Material ist Fibroin, ein Faserprotein welches aus der Seide der *Bombyx Mori* Larven oder gewisser Spinnen gewonnen werden kann. Dank der polymorphen Struktur von Fibroin kann das Protein sowohl in eine wasserlösliche amorphe als auch wasserunlösliche kristalline Form gebracht werden. In dieser Arbeit wurden Fibroin-Dünnschichten mittels Rotationsbeschichtung auf Siliziumscheiben aufgebracht und anschließend in Ethanol eingetaucht, welches die Kristallisation induziert und das Material wasserunlöslich macht. Anschließend wurden die Kristalle mittels TRSL selektiv in Kontakt mit der heißen Spitze aufgeschmolzen, wodurch das thermisch modifizierte Material wasserlöslich wurde. Die laterale Auflösung der geschriebenen Strukturen sowie die Kantenrauigkeit werden

Acknowledgements

untersucht und mit der Größe der Fibroinmoleküle, welche die maximale Auflösung darstellt, verglichen. Des Weiteren wird gezeigt, dass Graustufenlithographie auch mit Fibroin möglich ist und dass das Material als Ätzmaske in einem Trockenätzprozess verwendet werden kann, um Strukturen von Fibroin in Siliziumdioxid zu erzeugen.

Der zweite Teil dieser Doktorarbeit befasst sich mit der Planung und Implementierung eines Gerätes zur Messung der Temperatur von geheizten Rasterkraftmikroskopspitzen. Dies ist begründet durch die Schwierigkeit, die Temperatur an der Spitze vor und nach dem Kontakt mit einem Substrat zu bestimmen. Verschiedene Thermometrietechiken, welche die Temperatur im Nanometerlängenbereich bestimmen können, werden evaluiert, wobei Fluoreszenzthermometrie mit Stickstofffehlstellen-besetzten Nanodiamanten die vielversprechendste ist. Das benötigte Gerät besteht aus einem Laser um die Fluoreszenz der Nanopartikel anzuregen, einem inversen konfokalen Mikroskop, einem Einzelphotonendetektor, einem Objektisch und einer Rasterkraftmikroskopvorrichtung. Der Aufbau der einzelnen Komponenten des Geräts wird in der vorliegenden Arbeit diskutiert und charakterisiert. Abschließend werden erste Resultate zur Temperaturmessung an den thermischen Spitzen gezeigt, welche in Übereinstimmung mit Messungen aus der Literatur sind.

Stichwörter: Thermische Rastersondenlithographie, Graustufenlithographie, Supramolekulares Polymer, Fibroin, Seide, Temperaturmessung auf der Nanoskala, Stickstofffehlstelle, Nanodiamanten

Contents

Acknowledgements	v
Abstract	vii
Zusammenfassung	ix
Table of Contents	xiv
List of Figures	xvi
List of Tables	xvii
1 Introduction	1
1.1 Background and Motivation	1
1.2 Thermal Scanning Probe Lithography	4
1.2.1 A Brief History of t-SPL	4
1.2.2 State of the Art	6
1.2.3 Conclusion	10
1.3 Wide-Range Thermometry at the Nanometer Scale	11
1.3.1 State of the Art	11
1.3.2 Conclusion	21
1.4 Thesis Outline	22
2 t-SPL of a Stimuli-Responsive Fluorescent Supramolecular Polymer	23
2.1 Introduction	23
2.2 Materials and Methods	25
2.2.1 Sample Fabrication	25
2.2.2 AFM Force Spectroscopy	25
2.2.3 Thermal Scanning Probe Indentation and Lithography	26
2.2.4 Estimation of the Contact Temperature	26
	xi

Contents

2.2.5	Evaluation of Thermomechanical Indents	28
2.2.6	Indentation Force Calibration of Electrically Actuated Cantilevers	28
2.2.7	Fluorescence Microscopy	30
2.3	Results and Discussion	31
2.3.1	Thermomechanical Indentation	31
2.3.2	Correlation Between Pitch Size and Pattern Quality	34
2.3.3	Correlation Between Fluorescence Intensity and Pitch Size	34
2.3.4	Spatial Resolution	37
2.3.5	Hidden in Plain Sight	38
2.3.6	Fluorescence Change at Ambient Conditions	39
2.3.7	Reversible Thermomechanical Indentation	40
2.3.8	An Attempt to Pattern Supramolecular Polymer on a Paper Substrate	42
2.4	Conclusion	43
3	Silk Fibroin as a Resist for t-SPL	45
3.1	Introduction	45
3.2	Materials and Methods	47
3.2.1	Sample Fabrication	47
3.2.2	Thermal Scanning Probe Lithography	48
3.2.3	Calculation of the Line Edge Roughness	49
3.2.4	Dry-Etching of Silk Fibroin	49
3.3	Results and Discussion	49
3.3.1	Contrast Formation Mechanism in Thermally Modified Silk Fibroin	49
3.3.2	Resolution	54
3.3.3	Temperature Distribution Around the Tip Apex	56
3.3.4	Grayscale Lithography	59
3.3.5	Dry Etching of Silk Fibroin in He/H ₂ /C ₄ F ₈ Chemistry	60
3.4	Conclusion	62
4	Nanoscale Thermometry on a Heated t-SPL Probe	65
4.1	Introduction	65
4.1.1	Theory	65
4.2	Materials and Methods	70
4.2.1	Diamond Nanoparticles and Sample Preparation	70
4.2.2	Fabrication of the Microwave Antenna	71
4.3	NV ⁻ Thermometry Setup	71

4.3.1	Laser	71
4.3.2	Confocal Laser Microscope	72
4.3.3	Fluorescence Detection	73
4.3.4	Sample Stage	74
4.3.5	Positioning and Resistive Heating of the Thermal Probe	75
4.3.6	Microwave Magnetic Field Generation	75
4.3.7	Software	76
4.4	Characterization and Calibration	79
4.4.1	Optical Alignment	80
4.4.2	Laser Power Calibration	81
4.4.3	Electrical Characterization of the Cantilevers	81
4.4.4	Surface Detection and Surface Metrology with Thermal Scanning Probes	82
4.4.5	Tip Alignment with Respect to the Laser Beam	83
4.4.6	Calculation of the Magnetic Field Produced by the MW Antenna .	84
4.4.7	Localization of Fluorescent Particles and Optically Detected Mag- netic Resonance	86
4.5	NV ⁻ Center-Based Thermometry on Heated Probes	87
4.6	Conclusion	91
5	Conclusion and Outlook	93
5.1	t-SPL on a Fluorescent Supramolecular Polymer	93
5.2	Silk Fibroin as a Resist for t-SPL	94
5.3	Nanoscale Thermometry on Heated Probes Using NV ⁻ Centers	96
A	Appendix	97
A.1	Effect of Thermal Spreading and Tip Shape on Resolution	97
A.2	Script for Rim Detection	98
A.3	Script to Compute the Line Edge Roughness	100
A.4	Script to Simulate Temperature Distribution around the Tip	101
A.5	Script to Compute the Magnetic Field from a Wire	110
Bibliography		124
Acronyms		130
Photographic Credits		131

Contents

Curriculum Vitae

133

List of Figures

1.1	Overview of nanoscale fabrication techniques based on resolution and throughput	2
1.2	Overview of scanning probe lithography techniques	5
1.3	Overview of nanoscale thermometry techniques	12
1.4	Thermal scanning probe microscopy techniques	14
1.5	Scanning near-field thermometry techniques	17
1.6	Thermometry using fluorescent nanoparticles	20
2.1	Concept of nanolithography with a fluorescent supramolecular polymer . .	24
2.2	Thermal resistance model of a heated AFM tip in contact with a substrate	27
2.3	t-SPL pattern for the evaluation of nanoscale indents	28
2.4	Indentation force calibration curve for a thermal scanning probe	30
2.5	Proof-of-concept thermal patterning of a fluorescent structure	31
2.6	Thermomechanical indentation of a supramolecular polymer	32
2.7	Influence of indent distance on the quality of patterns	35
2.8	Correlation between fluorescence intensity and pitch size	36
2.9	Comparison between optical resolution and the resolution achieved by t-SPL	38
2.10	Nanoscale patterns with distinct topography but same fluorescence intensity	39
2.11	Color change during cooling of a fluorescent supramolecular polymer . . .	40
2.12	Writing and erasing thermomechanical indents on a supramolecular polymer	41
2.13	t-SPL on paper coated with a fluorescent supramolecular polymer	43
3.1	Concept of silk patterning by t-SPL	47
3.2	Determination of the line edge roughness	48
3.3	Contrast formation in t-SPL on silk fibroin	50
3.4	Reversibility of t-SPL treated silk fibroin by ethanol immersion	51
3.5	Pyrolysis of silk fibroin in an oven	52
3.6	Correlation between temperature and shrinkage	53

List of Figures

3.7	Observation vs. explanation diagram for the contrast mechanism	54
3.8	Resolution and LER of t-SPL pattern in silk fibroin	55
3.9	Simulation domain for the heat transfer from a tip to the substrate	56
3.10	Simulating the temperature distribution around the tip in silk fibroin	59
3.11	Grayscale lithography on silk fibroin and rim-depth correlation	60
3.12	Dry-etch rate of silk fibroin in He/H ₂ /C ₄ F ₈ chemistry	61
3.13	Pattern transfer from silk fibroin into silicon dioxide	62
4.1	Orbital diagram of the NV ⁻ center	66
4.2	Comparison between temperature dependence of the ZFS and the fluorescence intensity found in literature	69
4.3	Layout and process flow of the microwave antenna	70
4.4	CAD drawing of the NV thermometry setup	72
4.5	Photography of the laser and the scanning stages	73
4.6	Schematic overview of the NV thermometry setup with the electronics	74
4.7	Electrical connection of the cantilever	76
4.8	Diagram of the software to operate the NV thermometry setup	77
4.9	SubVI for scanning of the stages	79
4.10	User interface of the software to perform ODMR experiments	80
4.11	Laser power calibration	81
4.12	Current-Voltage characteristics of the cantilever	82
4.13	Tip approach curve and topography scanning	83
4.14	Alignment of the cantilever to the laser	85
4.15	Numerical calculation of the field created by the microwave antenna	87
4.16	Localization of fluorescent particles and ODMR	88
4.17	NV ⁻ center-based thermometry with a 1 μ m particle	89
4.18	NV ⁻ center-based thermometry with 40 nm particles	90
5.1	Lift-off with silk fibroin and thermal contact lithography	95
A.1	Influence of thermal spreading and tip shape on resolution	98

List of Tables

1.1	Overview of materials and possible applications in t-SPL	8
-----	--	---

1 Introduction

1.1 Background and Motivation

Conventional photolithography at a wavelength of 193 nm has been the driving technology in large-volume metal-oxide-semiconductor fabrication, but has reached a limit in minimal achievable pitch size in a single fabrication step at 80 nm. To further miniaturize the lithographic features into the single-digit nanometer range, multiple-step patterning techniques have been introduced at the expense of higher production costs.¹ To considerably increase the resolution of optical lithography, shorter wavelengths are required. The long predicted introduction of extreme ultraviolet lithography (EUVL) into large-volume manufacturing is only now becoming reality. EUVL, working at a wavelength of 13.5 nm, can significantly reduce the number of processing steps, but poses technical challenges such as handling of optical power up to 250 W, cooling due to heat generation and requires the development, fabrication and maintenance of new masks. Only recently, major chip producers such as Samsung, TSMC and Intel started producing chips with a 7-nm EUV process for consumers.² However, for smaller node sizes of 3 nm and 1 nm, a higher light power of 500 W and 1000 W are required, which makes the tools even more expensive. As a consequence of the high cost and technical complexity of optical lithography techniques with sub-10 nm resolution, alternative fabrication techniques have been explored over the last decades.

Figure 1.1a shows an overview of nanofabrication techniques, which are arranged in a resolution vs. throughput graph.¹ The blue ovals represent electron-beam lithography (EBL) techniques, which involve electrons to modify or add material to a substrate. The red ovals represent mask-based optical lithography techniques which induce chemical modifications in a material through light interactions. Nanoimprint lithography (NIL) techniques, combined in the orange oval, use a master stamp to create replicates, either by direct molding of the material of interest or by transferring material from the stamp on the sample. The green ovals represent scanning probe lithography (SPL) techniques, which have in common a sharp atomic force microscopy (AFM) tip to add, remove or

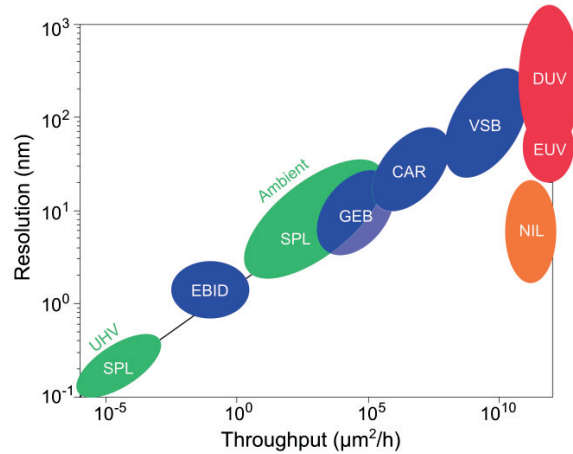


Figure 1.1 – Overview of nanoscale fabrication techniques based on resolution and throughput. The red ovals represent deep ultraviolet (DUV) and extreme-ultraviolet (EUUV) lithography, the blue ovals electron beam techniques variable shaped beam (VSB), chemically-amplified resists (CAR), gaussian electron-beam (GEB) and electron-beam-induced deposition (EBID) lithography, the green ovals are ambient and ultra-high vacuum (UHV) scanning probe lithography (SPL) techniques and the orange oval represents nanoimprint lithography (NIL). Reprinted with permission from [1].

modify a material.

The graph depicts a fundamental challenge in lithography which was first described by Tennant as the resolution/throughput trade-off.³ He found an empirical relation which holds true over 18 orders of magnitude between areal throughput A and resolution R of nanofabrication techniques:

$$A = 4.3R^5. \tag{1.1}$$

The relation implies that increasing the resolution by a factor of 2 reduces the areal throughput by a factor of 32. The R^5 relation can be explained by two factors: first, in serial writing processes such as EBL and SPL, the areal throughput scales with R^2 . Second, higher resolution usually requires more “careful” handling, alignment, patterning etc., which accounts for the R^3 . For example, in EBL it takes longer to expose a smaller pixel because a higher resolution requires higher electron energies, which decreases the interaction of the electrons with the resist. As a consequence, longer exposure times are required. Other factors which can limit the throughput are the data transmission rate of the electronics or the stage speed to scan the substrate such as in SPL. In general, the throughput/resolution trade-off manifests itself because fabricating something faster, inevitably leads to more mistakes or the other way around, achieving high precision takes a longer time.⁴ Interestingly, it can be seen in Figure 1.1 that EUV and NIL do not

to follow the same trend. For EUV, the increase in resolution (while maintaining the throughput) was only possible due to heavy investments in research and development of new EUV light sources and reflective optics. NIL has made great advances towards volume production due to a switch from rigid to soft stamps and tool improvements for step and repeat patterning.⁵ It has been demonstrated, that sub-10 nm resolution can be achieved at a throughput of up to 60 wafer per hour and stamps can be reused for at least 600 imprints without observable degradation.⁵ A systematic study on the reliability and wear of NIL for high-volume fabrication is yet to come.

Due to economic considerations, a throughput of 100 wafers per hour (or 10^{12} $\mu\text{m}^2/\text{h}$) is required in high-volume manufacturing.^{1,6} As can be seen from Figure 1.1, currently only mask-based nanofabrication techniques are meeting this demand. As an example, an array of 10^7 scanning probes working independently would be required to meet a similar throughput. Despite the low throughput, only maskless lithography techniques such as EBL and SPL enable the fabrication of high-precision masks. Between SPL and EBL, the latter is well established in research, small volume and mask fabrication. SPL is currently only used in research, but poses several advantages over electron-beam lithography: First, a direct feedback during patterning is possible since the probe can simultaneously image the topography during patterning. This so-called closed-loop lithography makes it possible to optimize the patterning stimulus during treatment of the material. Second, the ability to image and pattern with the same tool allows markerless alignment, which is a unique feature in the universe of nanofabrication techniques.⁷ Third, parallelization of the patterning process is facilitated by the simple implementation of the scanning probes and can significantly increase the patterning speed.^{8,9} Fourth, fabrication of single-digit nanometer structures can be performed at ambient pressure.¹⁰

Figure 1.2a shows a graph with different SPL techniques, classified by the dominant tip-surface interaction. The driving mechanisms in SPL are mechanical, thermal, diffusive and electrical processes, or combinations of these.¹ In mechanical SPL, the probe is used to selectively remove material from a surface by applying a force to create a topographical contrast or to locally remove self-assembled monolayers. The working principle of bias-induced SPL is based on high electric fields between the tip apex and the sample to induce electrochemical processes on the surface of the sample. Oxidation SPL makes use of the water meniscus which forms at ambient conditions between a tip and a surface, and laterally confines the oxidation reaction on the surface. Dip-pen SPL can be used to transfer molecules, polymers or colloidal particles from the tip to a substrate by diffusion. In thermal SPL (t-SPL) and thermochemical SPL (tc-SPL), a heated probe is used to remove or chemically modify a sample material.

The motivation of this work is to explore new material systems that can be used in combination with t-SPL to create micro- to nanometer-sized patterns at sub-100 nm resolution. The choice of t-SPL as the patterning technique is based on the versatility of heat interactions with matter. During t-SPL experiments, the temperature at the tip apex

or at the tip-sample contact is experimentally unknown and depends on many parameters such as the tip-sample thermal contact resistance, the tip apex size or the sample thermal conductivity. Therefore, a second part of this thesis concerns the evaluation, planning and construction of a setup for nanometer scale thermometry in combination with thermal scanning probes and measurements thereof.

The remaining part of this introduction is divided in two sections: The first section is about t-SPL, where the history and the state of the art is reviewed with an emphasis on materials that have been explored with t-SPL and their applications. In the second section, the state of the art of wide-range nanoscale thermometry is reviewed. The different techniques are evaluated in view of their applicability for nanoscale temperature measurements at the apex of a heated probe or at the sample surface.

1.2 Thermal Scanning Probe Lithography

Thermal scanning probe lithography lines up with the other scanning probe techniques, whereby thermal interactions between the probe and a material play a key role. Heat provided by a scanning probe can remove material by e.g. degradation or desorption or trigger a chemical reaction that alters the surface chemistry of the sample as illustrated in Figure 1.2b. One refers to thermal scanning probe lithography (t-SPL) when material is removed from the substrate and thermochemical scanning probe lithography (tc-SPL) when the heat induces a change in the substrate chemistry. Throughout the thesis, the term t-SPL will be used for both techniques to describe thermal scanning probe lithography in general and the context will make clear which type of sample modification is referred to. A third technique involving heated probes is thermal dip-pen lithography, where the heat from a coated probe is used to assist the transfer of the loaded material to the substrate as depicted in Figure 1.2b.¹¹⁻¹³ This technique will not be covered in this thesis.

The state of the art of SPL in general has been reviewed in several excellent papers by Tseng *et al.*¹⁴ and more recently by Garcia *et al.*¹ However, an overview of t-SPL techniques and materials does not exist and for this reason will be reviewed here.

1.2.1 A Brief History of t-SPL

The origins of t-SPL date back to the 1990s, when H. J. Mamin and D. Rugar performed their first experiments at IBM Almaden on thermomechanical indentation of polymers with heated atomic force microscopy probes (AFM). The motivation behind the invention, which later became the so called *Millipede* project, was to increase data storage capabilities for hard discs by thermomechanical indentation with a heated tip into a polymeric substrate at an unprecedented storage density on the order of a few Tb/in². The

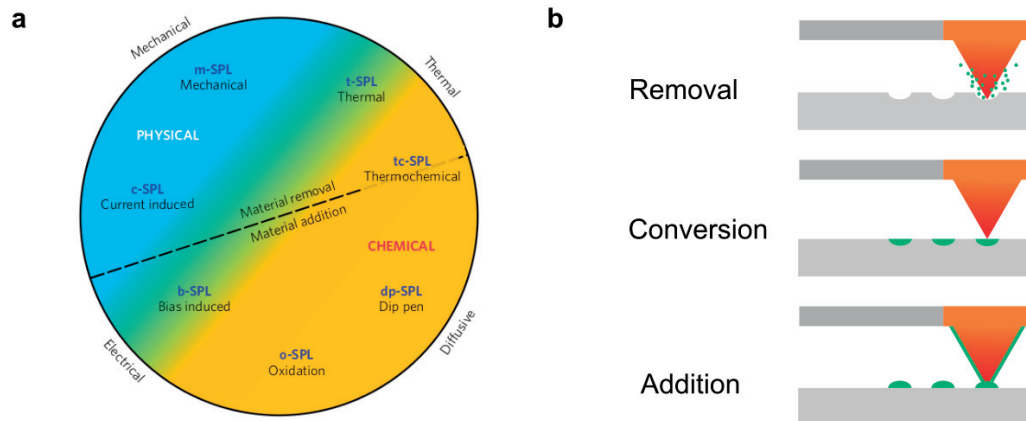


Figure 1.2 – (a) Overview of scanning probe lithography techniques, classified by surface interaction mechanism. Reprinted with permission from [1]. (b) Sketch of the three types of modification that can be achieved with t-SPL: Removal of material by evaporation or thermal degradation, chemical or physical conversion and addition of material by thermally controlled diffusion of material from the tip to the substrate.

initial setup included an AFM tip and a rotating polymer disc made out of poly(methyl methacrylate) (PMMA). The tip was heated with a focused infrared laser through the transparent PMMA disc and was actuated towards the polymer through a piezoelectric actuator to form an indent.¹⁵ To decrease the size of the setup, the cantilever design was continuously optimized by replacing the external laser with integrated resistive heater and a thermoresistive height sensor for direct readout of the written indents.^{16,17} Writing and readout speed was further increased by parallelization of the probes;¹⁸ writing and erasing were enabled by reducing the thickness of the PMMA layer to 40 nm. At the peak of the *Millipede* project, a prototype data storage unit at a size of $10 \times 10 \text{ mm}^2$ and a storage density of 1 Tb/in^2 with 4096 cantilevers in parallel was demonstrated.¹⁹

While the technology developed in the *Millipede* project for data storage did not find its way into a consumer product, it led to the development of t-SPL. A major breakthrough towards nanoscale mask-less lithography with heated probes was achieved by the development of thermal resists that fully desorb from the substrate upon heating at short time scales but are sufficiently resistant during dry-etching. One class of materials that fulfills these requirements are organic glasses, which are composed of molecules that stabilize via hydrogen interactions to form a solid at room temperature. At temperatures above the evaporation temperature, the molecules have sufficient energy to overcome the binding energy and desorb from the surface. Molecular glasses were successfully used to transfer 8 nm deep patterns into a 3-nm thick silicon oxide hard mask via a dry etching process.²⁰ A second approach is to use a polymer with a low ceiling temperature, where one degradation event in the polymer is amplified via unzipping of the entire chain.^{21,22} Poly(phthalaldehyde) (PPA) is such a resist, initially developed for dry-development

in electron-beam and microlithography.²³ The advantage of a resist like PPA that fully volatilizes upon heating is that development in a liquid can be avoided, which reduces the risk of contamination after patterning. The concept of nanoscale thermal patterning of self-amplified depolymerization polymers was successfully demonstrated by Knoll *et al.*²²

While different thermal scanning probe lithography systems evolved over time,^{22,24–28} currently only one technology has been commercialized into a high-speed thermal lithography product for academic research and industrial use (NanoFrazor, Swisslitho AG).

1.2.2 State of the Art

In this section, the state of the art in thermal scanning probe lithography is reviewed with a focus on different materials systems and potential applications. Table 1.1 gives an overview of materials and applications that have been reported in the context of probe based thermomechanical indentation, thermochemical lithography and thermal lithography.

Organic Materials

Most organic materials have been initially investigated for thermomechanical data storage applications. In particular, the fundamental questions of nanoscale wear, reliability and resolution were addressed. Later, the focus shifted towards thermochemical modification of materials or removal of the material by degradation or desorption. Following the evolution of material processing by t-SPL, the literature in this section is grouped by t-SPL induced material changes.

Thermomechanical indentation of polycarbonate (PC) and poly(methyl methacrylate) (PMMA) thin films was performed in the early thermal scanning lithography experiments for data storage applications.¹⁷ Thermal indentation and reflow posed an innovative system to write and erase data at a high density. The indentation behavior of SU8, a commercial resist used in photolithography, has also been investigated under ballistic nanoindentation using a heated probe with potential applications in data storage.²⁹ Polystyrene (PS) thin films were used with heated probes to demonstrate the applicability of local thermal analysis at the nanometer scale.³⁰ The relaxation behavior of crosslinked PS has been investigated by thermal indentation and subsequent quenching of the polymer at rates up to 10^8 K/s. It was found that the relaxation behavior of this material evolves logarithmically over 10 orders of magnitude in time.³¹ PS was further used as a substrate in wear and stress studies of a few nanometers thick norbornene layer. It was found that the norbornene layer increases wear-resistivity by protecting the PS underneath from heat and pressure of the tip, therefore allowing more reliable thermomechanical indentation.³² Crosslinking of poly(hydroxyl styrene) based films were investigated by thermomechanical indentation with a heated probe, whereby it was found that a high density of crosslinks

1.2. Thermal Scanning Probe Lithography

is desirable for structures to reduce pile-up formation during indentation and minimize thermal deformation of the material.²⁸ Poly(aryl ether ketone) (PAEK) was tested by thermomechanical indentation with a heated probe for data storage applications. It was demonstrated that the data density is determined by nonlinear interactions between adjacent indents and that the size of the indent radius is limited to the correlation length of the polymer. Therefore, a lower limit for thermomechanical indentation of 5 nm in diameter was predicted.³³ A study by Gotsmann *et al.* showed that by optimization of the crosslink density of PAEK, thermomechanical datastorage devices could reach lifetimes of up to 10 years at storage densities of 1 Tb/in².³⁴ Thermomechanical writing of a 80 nm thin fluorocarbon film was performed to demonstrate reading and writing with 5 thermal probes in parallel at a speed of 0.5 $\mu\text{m/s}$.⁹

Thermally-induced crystallization of poly(ethylene terephthalate) (PET) was studied by Duvigneau *et al.* to investigate the thermal transport around the nanoscale contact area between a heated AFM probe and the sample. The heat of the probe induced crystallization of the initially amorphous PET, making it possible to image the spread of heat in a polarized light microscope.⁴³

AZ5214E, a commercial resist, was used as a negative resist for t-SPL by thermally inducing cross-linking, but a long conversion time of up to 2 seconds per indent was required.³⁵ Reversible cross-linking at much shorter time scales on the order of 10 μs was achieved using a Diels-Alder polymer, which can be reversibly depolymerized into low molecular-weight oligomers upon heating and re-crosslink upon cooling.³⁶ Potential applications of this material system in data storage and dry lithography were shown.

Poly(p-phenylene vinylene) (PPV) nanostructures were fabricated from a precursor via a thermally induced chemical reaction. PPV is a widely studied conducting polymer with potential applications in organic electronics, nanophotonics and biosensing devices.^{24,27,64-66} A similar methodology was adopted to create pentacene nanostructures from a precursor material by thermochemical conversion with a heated probe at 120-200 °C. Pentacene, a semiconducting organic material has potential applications in organic thin-film transistors or light emitting diodes.⁶⁸

Graphene oxide sheets have been reduced by scanning of a heated atomic force microscope tip to create nanometer sized lines of conducting reduced graphene oxide. The interest in reduction of graphene oxide by thermal probes lies in its conductivity change from an electrical insulator to a semiconductor or semimetal in the reduced form. Due to structural defects, the electrical properties are not comparable with graphene but similar to doped conductive polymers.³⁸

The reverse conversion from graphene to graphene oxide by a heated probe was also demonstrated. By scanning a heated tip at speeds on the order of a few $\mu\text{m/s}$, 300-1200 nm wide structures of graphene oxide were obtained. Similar experiments were performed by

Chapter 1. Introduction

Table 1.1 – Overview of materials and their applications that have been patterned with heated AFM probes. Top rows are organic materials and bottom rows are inorganic materials.

Material	Applications	References
AZ5214E		[26, 35]
Diels-Alder polymer	Lithography, Data storage	[36]
Fluorocarbon		[9]
Fullerene-based		[37]
Graphene oxide	Nanoelectronics	[24, 38]
Molecular glass	Pattern transfer	[20, 39, 40]
PAEK	Data storage	[33]
PC	Integrated circuit, Bioengineering, Data storage	[17, 41]
PC-IV		[28]
PE		[42]
PET	Nanoscale thermal analysis	[43]
PHOST		[28]
PMMA	Lift-off, Data storage	[15, 44–50]
PMMA/BPO/Ag ₃ N	Plasmonics	[51]
PMMA/MA		[37]
PPA	Templating, Lift-off, Photonics, Data preservation, Pattern transfer, Grayscale lithography	[21, 22, 52–63]
PPC	Biodegradable resist	[37]
PPV precursor	Cryptography, Photonics, Single photon emitter, Semiconductor, Nanoscale LED, NEMS, Quantum electronics, Sensors	[24, 27, 64–66]
PS	Local thermal analysis, Data storage	[30, 32]
PS-BCB	Data storage	[31]
Pb-PtBA	Chemical functionalization	[67]
Pentacene precursor	Organic transistor	[68]
Polyacetal-based PK12	Positive tone resist	[37]
Polythioaminal		[69]
QSR-5	Pattern transfer	[37]
SAMs		[28]
Silk fibroin	Pattern transfer, Photonic structures	This work
SU-8	Data storage	[29]
THP protected polymers	Chemical gradient	[25, 70–73]
UPy-OPV-UPy	Multilevel security features	This work
Ge ₂ Sb ₂ Te ₅	Data storage	[74]
GeTe	Nanofluidics, Metamaterials, Data storage	[75]
In ₁₅ Sn ₂₀ Sb ₆₅	Data storage	[17]
Pb(Zr _{0.52} Ti _{0.48})O ₃	Energy harvesting, Actuator, Sensor	[76]
PbTiO ₃		[76]
Ru/IrMn/CoFeB	Magnetic computing, Spintronics	[77]
Titanium		[26]

1.2. Thermal Scanning Probe Lithography

the same group on a titanium film to produce 87 nm wide lines of TiO₂. However, the results indicate that thermal oxidation of titanium does not produce reliable patterns.²⁶

An approach to locally increase the temperature around the tip apex, is to use an energetic reagent which decomposes in an exothermic reaction, triggered by the thermal probe. PMMA films, preloaded with silver nitrate and benzoyl peroxide, were thermally treated with a heated probe to induce the formation of silver nanoparticles for plasmonic applications. Benzoyl peroxide decomposed in an exothermic reaction, adding additional energy for the silver nanoparticle formation.⁵¹

Molecular glasses are low-molecular weight organic compounds, which stabilize at room temperature via hydrogen interactions to form a solid. At temperatures, that are sufficiently high to overcome the hydrogen bonding energy, the molecules desorb from the surface. The phenolic resist that was investigated by t-SPL had a PVD temperature of ~220 °C and desorbed locally from the substrate in contact with the heated tip. In one application, a pattern was transferred in a dry-etching process from the resist into a SiO₂ hard mask and further etched into silicon, producing 15 nm sized structures.²⁰ A systematic study on the performance of supramolecular glasses for SPL was performed by Neuber *et al.* It was shown that these resists can be used for c-SPL and t-SPL and that they exhibit high etch selectivity towards SiO₂ in a dry-etch process.^{39,40}

One of the earliest publications on thermal scanning probe induced degradation for lithography applications, has been performed on cross-linked PC films. Hua *et al.* studied the influence of crosslinking on film stability during indentation. It was found that crosslinking of the polymer film prior to thermal lithography prevents melting of the polymer before degradation and considerably reduces the formation of a pile-up. However, this comes at the cost that the fraction of non-decomposed material increases with the degree of crosslinking.⁴¹ As discussed in Section 1.2.1, these side effects were mitigated by introducing PPA. PPA is a resist that decomposes via a self-amplified decomposition mechanism, meaning that scission of a bond in the polymer's backbone results in complete decomposition of the polymer chain into its monomers.²¹ The most important applications of PPA in t-SPL are grayscale lithography,^{22,53,58} data preservation,⁵⁹ pattern transfer,^{52,57} lift-off process⁶¹ and templating.^{55,60,63,78}

Thermally induced functionalization of surfaces is another interesting aspect of t-SPL. A successful approach is the thermal deprotection of functional groups to create nanoscale features with a distinct chemical contrast with respect to the untreated surface. Tert-butyl ester-protected carboxylic acid-functionalized acrylate and methacrylate films were treated by a thermal scanning probe with the goal to create nanoscale bio(reactive) interfaces.^{67,79} Methacrylate copolymers containing tetrahydropyran (THP) carbamate groups, which can be thermally deprotected with a heated probe at temperatures between 105-220 °C to unmask the primary amines, were investigated for biological applications.⁷² Functionalization of the unmasked amines with specific molecules makes it possible to

selectively bind nano-objects to the patterned surface.²⁵ By repeating the deprotection and subsequent functionalization with a different molecule, multiplexed patterns can be obtained. This approach opens a wide range of applications in nanobiotechnology to actively control the surface position of individual proteins or nanoparticles. It was shown, that using this approach, chemical gradients at a spatial resolution of 20 nm can be produced.⁷¹

Inorganic Materials

A majority of the materials that have been studied in t-SPL are organic materials due to the low temperatures to induce a phase change or a chemical reaction. Yet, there are a few interesting examples where inorganic materials have been patterned by t-SPL.

One of the earliest experiments was performed by Mamin *et al.* on an optical phase change material (PCM) $\text{In}_{15}\text{Sn}_{20}\text{Sb}_{65}$, where they induced crystallization of the amorphous thin film with the heated probe for data storage applications.¹⁷ Later, a germanium tellurium based PCM ($\text{Ge}_2\text{Sb}_2\text{Te}_5$) was used in combination with a laser-heated tip to write, read and erase bits at a storage density of 3.3 Tb/in².⁷⁴ In a more recent study, GeTe PCMs have been patterned by t-SPL. These chalcogenide PCMs are explored for emerging applications in RF devices and metamaterial surfaces in the visible and infrared range.⁷⁵

Thermal fabrication of ferroelectric materials with heated probes was investigated by Kim *et al.*, motivated by a lack of CMOS compatible fabrication techniques. The ferroelectric nanostructures were fabricated from $\text{Pb}(\text{Zr}_{0.52}\text{Ti}_{0.48})\text{O}_3$ and PbTiO_3 sol-gel precursor films deposited on plastic, glass and silicon substrates.⁷⁶

Re-programmable magnetic nanostructures have been created by scanning heated probes on Ru/IrMn/CoFeB multilayer structures, which opens a new fabrication route to the development of novel metamaterials with finely tuned magnetic properties.⁷⁷

1.2.3 Conclusion

Thermal scanning probe lithography is a versatile nanofabrication technique which has been applied on a variety of inorganic and organic substrates. A strength of t-SPL is the short times required to induce a material change (few microseconds), which results in high patterning speeds (few $\mu\text{m/s}$ to mm/s). Most materials can be patterned in a single step and no subsequent development is required, which avoids cross-contamination. In contrast to EBL, t-SPL does not require sophisticated equipment and can be upscaled to increase throughput by parallelization of the probes. A disadvantage of t-SPL is tip deterioration due to wear or contamination, which decreases the resolution and eventually makes the tip unusable. Upscaling of the fabrication process by parallelization for lithography has yet to be implemented on an industrial scale to be compatible with

the demanded throughput, but some attempts are ongoing.⁵⁴

1.3 Wide-Range Thermometry at the Nanometer Scale

A second focus of this thesis is nanoscale thermometry. The question about the temperature at the tip apex of the heated probe or the temperature of the material during thermal processing naturally rises during t-SPL. Examples in the previous section about thermal scanning probe lithography have shown that often the thermal response of a material at the nanometer scale is different than at the macroscopic scale. An example is the glass transition temperature of many polymers, when measured by local thermal analysis with a heated tip, is different than the corresponding bulk values.⁸⁰

Extensive review papers on nanoscale thermometry have been written by Cahill *et al.*,⁸¹ Brites *et al.*⁸² and a more recently by Marta Quintanilla and Luis Liz-Marzán.⁸³ A review on nanoscale scanning thermal microscopy (SThM) was published by Gomès *et al.*⁸⁴ While most of the review papers focus on the spatial resolution and the sensitivity of thermometry techniques, few articles discuss the temperature range of nanoscale thermometers and their limitations. In view of a thermometry technique for thermal scanning probe lithography, the important criteria are: high spatial resolution down to a few tens of nanometers, an operation temperature between room temperature and 400-500 °C, within which the glass transition or thermal degradation of organic substrates occurs^{20,22,43} and operation at atmospheric pressure.

1.3.1 State of the Art

In this section, the state of the art of a broad range of nanometer scale thermometry techniques is reviewed in view of their applicability for nanoscale temperature measurements in combination with organic materials and heated probes. The measurement techniques that allow *in situ* measurement of the temperature while approaching the substrate are discussed in more detail. Techniques to solely measure the physical properties of materials, such as the thermal conductivity, are not considered.

Figure 1.3 provides an overview of the temperature and spatial resolution range that has been reported in the literature for nanometer scale thermometry techniques: resistive scanning thermal microscopy (r-SThM),⁸⁵⁻⁸⁷ thermoelectric scanning thermal microscopy (te-SThM),⁸⁸⁻⁹⁰ scanning tunneling microscopy (STM),⁹¹ plasmon energy expansion thermometry (PEET),⁹²⁻⁹⁴ infrared thermometry,^{95,96} Raman thermometry,⁹⁷⁻⁹⁹ luminescence thermometry¹⁰⁰⁻¹⁰⁹ and color center defects.¹¹⁰⁻¹¹⁴ In the following sections, the most interesting publications for this work are going to be discussed.

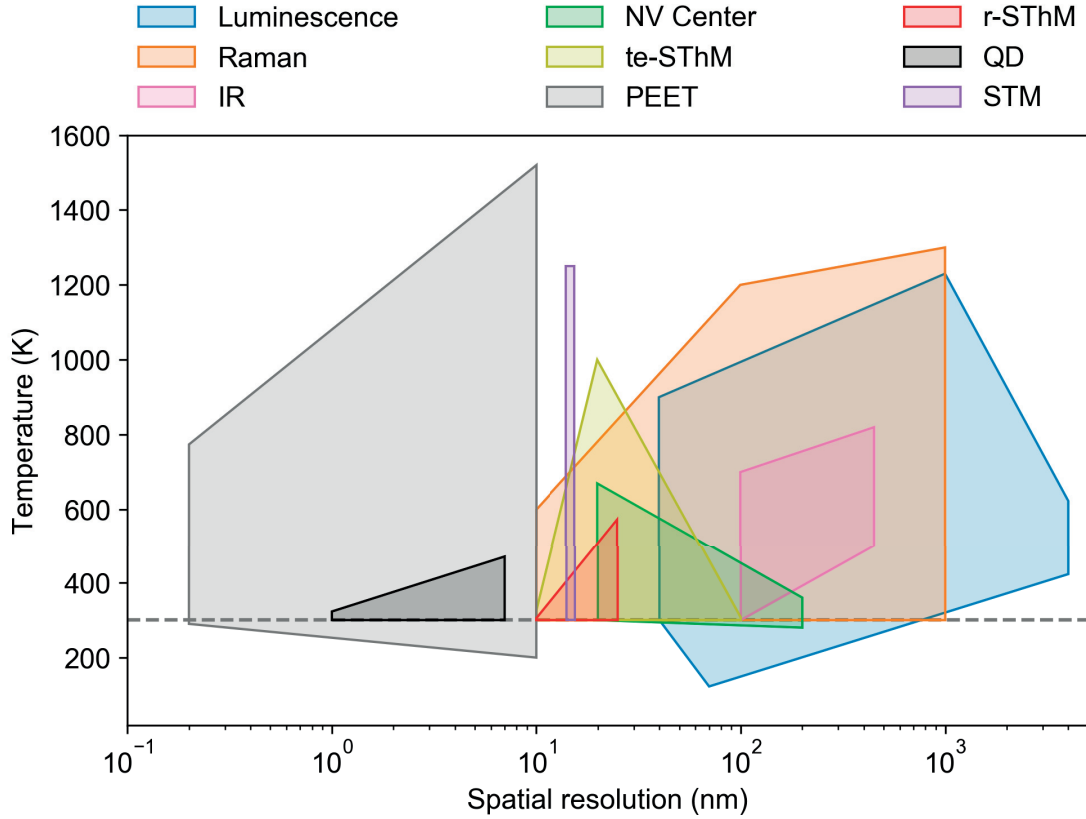


Figure 1.3 – Comparison of nanoscale thermometry techniques, based on their spatial resolution and the temperature range over which they have been applied in literature.

Resistive Scanning Thermal Microscopy

The temperature dependence of the electrical resistance is a commonly used principle for thermometry. For a calibrated thermometer, the temperature can be inferred by measuring the electrical resistance and converting it into a temperature using the calibration curve. At the nanometer scale, resistive thermometry is accomplished by raster scanning a dedicated probe in contact with the substrate and measuring the thermometer’s resistance change as a function of the tip location. In the literature, metallic or doped silicon probes have been used, which can be either run in passive or active modes.

In passive mode, a small probing current is applied to the cantilever to sense electric resistance changes due to the heat flow from a heated substrate into the probe. As a first-order approximation, the temperature can be calculated from the resistance change by $R(T) = R_0(1 + \alpha(T - T_0))$, where $R(T)$ is the electrical resistance of the probe at sample temperature T , R_0 is the electrical resistance at T_0 and α is the temperature coefficient of the electrical resistivity. A major limitation of this approach is that, due to

1.3. Wide-Range Thermometry at the Nanometer Scale

a high thermal boundary resistance on the order of 10^{-7} to 10^{-9} $\text{m}^2\text{K}/\text{W}$, the resistive thermometer cannot equilibrate with the surface.⁸⁴

In the active mode, the probe is heated and the tip-sample contact resistance can be determined by measuring the change in heat-flux \dot{Q}_{ts} between the in-contact and out-of-contact position $R_{ts} = \frac{T_h - RT}{\dot{Q}_{ts}}$, where T_h is the heater temperature and RT is the room temperature. Typically, quantitative experiments are performed under vacuum to avoid heat losses through the air and to avoid lateral heat transfer via convection from the heated sample to the tip, which reduces the spatial resolution. The temperature of a heated sample T_s is then inferred from the additional heat flux $\Delta\dot{Q}_{ts} = \frac{-\Delta T_s}{R'_{ts}}$. If ΔT_s is large, the assumption that R_{ts} is temperature independent does not hold and instead the apparent change in thermal resistance $R'_{ts} = (T_h - RT)/(\dot{Q}_{ts} + \Delta\dot{Q}_{ts})$ is used and the sample temperature can be calculated from⁸⁶

$$\Delta T_s = (T_h - T_s) \left(1 - \frac{R_{ts}}{R'_{ts}} \right). \quad (1.2)$$

Contact-related effects can complicate the calculation of R_{ts} , introducing artifacts in the temperature mapping of non-uniform samples due to changes in tip-sample contact area. Menges *et al.* developed a procedure to separate temperature-related and topographic effects by modulating the driving voltage of the heated device. Figure 1.4a shows the heated scanning probe, which is used to scan the surface topography of the sample and map the temperature of a 100 nm wide gold interconnect. By modulating the amplitude of the bias across the gold nanowire, the sample temperature and the tip-sample resistance can be calculated simultaneously.⁸⁷ A limitation with regards to quantitative measurements is that experiments have to be performed under vacuum since the resistive temperature sensor is typically located a few hundred nanometers away from the tip apex in contact with the sample and convective heat losses would introduce an error in the measurement.

Thermoelectric Scanning Probe Microscopy

In thermoelectric scanning probe microscopy, the temperature sensor is directly brought into contact with the sample, which provides an advantage over resistive thermometry but requires more sophisticated tip designs. The thermoelectric effect is based on leveling of the Fermi energy between two metals when brought into contact, where electrons from the material with the higher Fermi energy are transferred to the material with the lower Fermi energy. As a consequence, the material with the lower Fermi energy is negatively charged, which results in a contact potential between the two materials.¹¹⁵ This contact potential is temperature dependent and can be expressed by $\Delta V = S\Delta T$.

To use the thermoelectric effect as a means to measure temperature at the nanometer

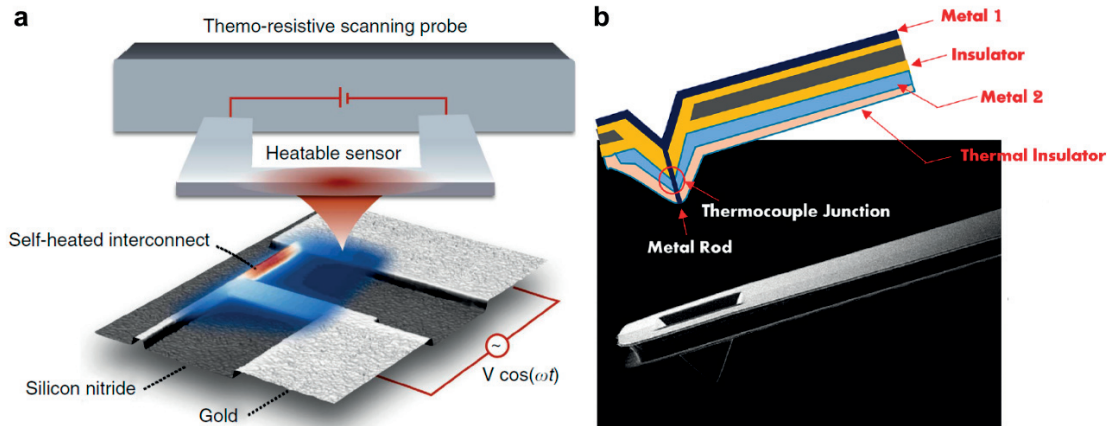


Figure 1.4 – Thermal scanning probe microscopy techniques. (a) The temperature measurement of a 100 nm wide, AC heated gold nanorod with a resistively heated thermal scanning probe is shown. The setup allows to measure temperature, tip-sample contact resistance and the surface topography. Reprinted from [87]. (b) The cantilever design and a SEM image of a thermoelectric scanning probe is shown. The design of the cantilever enables measuring the surface temperature at the nanometer scale at ambient pressure due to a thermal insulation layer between the thermocouple junction and the sample. Reprinted with permission from [90].

scale, a small probe composed of a thermocouple junction is typically used. As in resistive scanning probe microscopy, the heat flux through the surrounding gas reduces the spatial resolution of the temperature measurement, and the non-uniform thermal contact resistance can create artifacts in the temperature measurement. Therefore, most measurements are performed in vacuum with an active thermal feedback to maintain the tip temperature equal to the sample surface. This procedure is time consuming because for every position of the scanning probe the zero flux temperature of the heater has to be determined. Chung *et al.* developed a method that does not require the probe temperature to be equal to the sample temperature, but instead uses two measurements of heat flux at two different probe temperatures.¹¹⁶ A drawback of this technique is, that it requires two scans. More recently, Shekhawat *et al.* presented a thermocouple thermal sensor that can be operated at ambient pressure over a broad temperature range from room temperature up to 1000 K at sub-10 nm resolution by adopting an innovative cantilever design.⁹⁰ As illustrated in Figure 1.4b, the thermal probe is composed of a hollow silicon tip with a vertically integrated metallic nanowire, which forms a thermocouple with a second metal layer. The two metal layers are electrically isolated from each other except at the contact with the metallic nanowire. A thermal insulation layer shields the thermocouple junction from lateral heat flow. It has to be noted that the authors do not disclose the materials used for the cantilever fabrication in the publication. The thermal resolution was estimated to be ~ 0.04 K (at an acquisition time of 2 ms/pixel). This design opens a variety of applications that have not been possible with previous SThM tools such as thermometry on biological samples since no vacuum is required and it can be operated

1.3. Wide-Range Thermometry at the Nanometer Scale

in temperature mapping mode as well as in thermal conductivity mapping mode when a laser is used to heat the thermocouple.⁹⁰

Tunneling Current Thermometry

Another scanning probe technique that can measure the temperature over a broad temperature range at a high resolution is scanning tunneling microscopy. The linear temperature dependence of the relative Fermi-level shift between two conductors separated by a small distance, can be used as a direct measure of the absolute temperature. Andrei Pavlov demonstrated that the energy difference ΔE between a copper oxide sample and a platinum tip, which are separated by a gap of a few Å, linearly shift with temperature T in the range from 300 to 1250 K and can be described by $\Delta E(T) \propto k_B T$, where k_B is the Boltzmann constant. The spatial resolution obtained with this technique is on the order of a few nanometer. However, tunneling current thermometry measurements have to be performed in vacuum.⁹¹

The scanning probe techniques described above require a thermal contact between sample and the tip, which means that measuring the temperature can disturb the temperature of the sample. Despite the advances in fabrication of ultra-sharp probes with a tip apex diameter in the sub-nm range, the spatial resolution is limited by the size of the probe and establishing a contact between probe and sample can cause wear of the tip and sample. Contactless thermometry techniques can avoid these limitations as discussed in the following sections.

Plasmon Energy Expansion Thermometry

Plasmon energy expansion thermometry (PEET) is a contactless thermometry technique, whereby electrons are accelerated towards thin metal layers or conducting nanoparticles. A fraction of the transmitted electrons lose energy due to excitation of bulk plasmons at a specific energy. For the free electron model, the energy E to excite a bulk plasmon is $E = \hbar \sqrt{\frac{4\pi n e^2}{m}}$ where \hbar is the Planck constant, n is the number density of valence electrons, e the elementary charge and m the electron mass. By exciting a plasmon, the electrons lose energy, which can be detected by analyzing the transmitted beam with an electron-energy spectrometer. The temperature dependence in the energy loss originates from a change in the free electron density due to thermal expansion of the material at higher temperatures.⁹² Mecklenburg *et al.* used this technique to perform temperature measurements on sub-10 nm length scales on 100 nm thick aluminum wires in the temperature range from 300 - 500 K.⁹² In another study, the same group measured the temperature distribution in silicon nanoparticles from room temperature to 1530 K.⁹³

Despite the excellent temperature range and spatial resolution, a limitation of transmission electron-based thermometers is the necessity to perform the experiments in vacuum.

Other non-contact thermometry techniques that can be used at ambient pressure are discussed in the following sections.

Infrared Thermometry

Any body at a temperature above 0 K emits thermal radiation due to movement of electric charges. The intensity and spectral distribution of thermal emission depend on the temperature of the emitter. The emitted power is described by the Stefan-Boltzmann law of thermal emission $W = \sigma\epsilon T^4$, where σ is the Stefan-Boltzmann constant, ϵ is the emissivity of the body and T the absolute temperature. By measuring the total emitted power from a body, one can directly infer its temperature. In practice however, the emissivity changes with temperature and therefore calibration is required. Often calibration of the sensor is required too, since the sensitivity of optical sensors is wavelength dependent. By careful calibration of the emissivity of the sample and considering the sensitivity of the detector, the emitted power can be calculated by integrating the spectral density of thermal radiation as described by Planck's law:

$$P_{(\lambda,T)} = \frac{2\pi c}{\lambda^4 \left(\exp\left(\frac{hc}{\lambda k_B T}\right) - 1 \right)}, \quad (1.3)$$

where c is the speed of light, λ is the wavelength of the thermal emission, h is Planck's constant and k_B is the Boltzmann constant. Infrared thermometry has been performed over a broad temperature range from cryogenic temperatures up to 6000 K.¹¹⁷ A disadvantage of IR thermometry with regards to nanothermometry is that the spatial resolution is diffraction limited. The wavelength at which the thermal emission is maximum, is inversely proportional to the temperature described by Wien's displacement law: $\lambda_{max} = 2900 \mu\text{mK}/T$. As a consequence, only for temperatures above 3000 K, the peak wavelength is in the nanometer range.

Teysieux *et al.* performed near-infrared thermometry with a CCD camera at a temperature range from 560 to 720 K, selecting only the near-infrared range of the spectrum and therefore improving resolution but reducing the detectable temperature range.⁹⁵ To overcome the diffraction limit, near-field optical microscopy techniques have been explored. Goodson *et al.* developed a scanning near-field optical thermometer, made of a aluminum-coated tapered single-mode optical fiber, that was scanned over the sample at a distance of 5 nm to 3 μm above the emitting surface.¹¹⁸ More recently, Weng *et al.* developed an imaging systems that measures fluctuating electromagnetic evanescent waves scattered by a tip, which is placed in proximity to the sample, and detected in the far field by an infrared phototransistor as depicted in Figure 1.5a. The spatial resolution was estimated to be <100 nm with a temperature resolution of ~ 2 K over a temperature

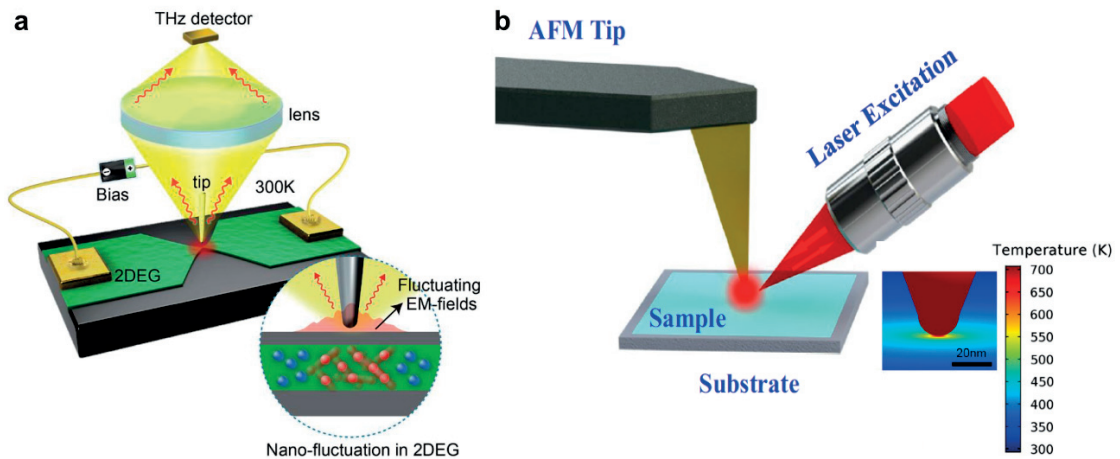


Figure 1.5 – Scanning near-field techniques to improve spatial resolution of infrared and Raman thermometry. **(a)** Nanothermometry system to measure electromagnetic evanescent waves from local current fluctuations using a modulated tungsten tip. Reprinted with permission from [119]. **(b)** Schematic design of a setup that enables near-field heating by a laser and tip-enhanced Raman thermometry. Reprinted with permission from [120].

range from 300 to 690 K. The key elements of this technique are a charge-sensitive infrared phototransistor as a detector, which is two orders of magnitude more sensitive to infrared radiation than conventional HgCdTe detectors, and a sharp tip that vibrates at 27 Hz with an amplitude of 100 nm in order to modulate the near-field radiation, thereby filtering out the much stronger far-field background radiation by using a lock-in amplifier.⁹⁶

Raman Thermometry

In Raman spectroscopy, inelastic scattering of monochromatic light is used to measure vibrational, rotational and other low-frequency modes of atoms, molecules and crystals. Typically, a laser is used to illuminate the sample and the scattered light is detected with a spectrometer. Besides a main peak, which appears at the same frequency as the laser due to elastic Rayleigh scattering, peaks at lower and higher frequencies appear in the spectrum. These shifts originate from inelastic scattering of light with the molecules. Laser light at a frequency ν_0 excites the molecule into a virtual state from which it can relax into an energy level above ground state under emission of light at a lower frequency $\nu_0 - \nu_{vib}$ (Stokes shift). During this process, a part of the energy from the laser is absorbed by the molecule and increases its vibrational energy. Alternatively, a molecule from a higher energy level can be excited into a virtual state and relax into the ground state under emission of a photon with a higher energy $\nu_0 + \nu_{vib}$ (Anti-Stokes shift).¹²¹

In Raman based thermometry, three temperature-dependent signals are typically used: (i) the temperature dependence of the Raman shift, (ii) the intensity ratio between the anti-Stokes and the Stokes shift $\frac{I_S}{I_{AS}} \propto e^{h\nu_{vib}/k_B T}$, and (iii) the Stokes line shift broadening

As with all optical techniques, the spatial resolution in Raman thermometry is diffraction limited. To improve the diffraction-limited spatial resolution of Raman based thermometers, the field enhancement of the electromagnetic radiation at a tip apex can be used. Tip-enhanced Raman spectroscopy for thermometry was first employed by McCarthy *et al.* using a two-laser setup to heat an AFM tip and probe its temperature.¹²² It was shown that the intensity of the Raman Stokes and anti-Stokes components were significantly higher compared to those obtained on a bulk sample, which was attributed to the presence of the tip. In more recent publications, tip-enhanced Raman spectroscopy was used to measure the temperature of the tip of heated cantilevers,^{123,124} and measurement of the contact temperature between a tip and the sample.^{98,120}

A different strategy to improve the spatial resolution of non-contact techniques is to place a nanometer-sized object in the region of interest, which transmits a temperature-dependent signal to a detector placed sufficiently far away from the sample to reduce perturbation of the measurement. Luminescent nanoparticles have been found as suitable nanometer-scale temperature sensors and will be discussed in the following sections.

Luminescence Thermometry

Luminescent thermometers exist in a broad variety such as organic fluorescent dyes, quantum dots and lanthanide based particles. Because organic fluorescent molecules, polymers and proteins are only stable in a narrow temperature range around room temperature they will not be further discussed. Fluorescent quantum dots are interesting as nanothermometers due to their small size (below 10 nm in diameter) and tunable emission range, but suffer from portability between different systems and environments.⁸³ Therefore, quantum dots are not considered in this work.

Lanthanide-based nanoparticles have been extensively investigated as stable temperature sensors over a broad temperature range. Lanthanide nanoparticles consist of a crystalline host material (e.g. PbF_2 or Gd_2O_3), which is doped with a certain concentration of lanthanide ions such as Er^{3+} , Yb^{3+} or Tm^{3+} to incorporate energy states into the crystal gap.¹²⁵ Lanthanide ions are interesting as thermometers because of their electronic configuration with the 4f orbital only being partially filled and shielded from the environment by completely filled 5s, 5p and 6s orbitals which are located further away from the core. As a consequence, lanthanide-based thermometers are less sensitive to environmental changes such as magnetic fields or the surrounding medium.⁸³ Three temperature-sensitive signals can be used for thermometry: (i) emission peak broadening due to lattice vibrations, (ii) intensity decrease with temperature due to non-radiative spin relaxation, assisted by

1.3. Wide-Range Thermometry at the Nanometer Scale

lattice phonons of the host and (iii) a shortening of the lifetime of radiative transitions due to non-radiative relaxation.⁸³ From the experimental point of view, the peak broadening can be very small and therefore requires high-resolution spectrometer equipment. Similarly, radiative lifetime measurements require a time-resolved photon detection system.¹²⁵ As a consequence, many lanthanide-based thermometry techniques are based on emission intensity. Due to the complex electronic band structures involving multiple excitation bands, the overall emission behavior of lanthanide-based nanoparticles is difficult to evaluate. Therefore, typically the emission intensity ratio between two thermally coupled energetic bands are chosen as the temperature sensitive signal, which follows Boltzmann statistics and can be expressed by the following equation:

$$\frac{I_2}{I_1} = C e^{-\Delta E/k_B T}, \quad (1.4)$$

where I_1 and I_2 are the intensities of two optical transitions in the fluorescence spectrum, C is a constant that depends on the experimental system and spectroscopic parameters, ΔE is the energy difference between the two bands and T the temperature.¹²⁵

A concern in using lanthanide-doped nanoparticles as high-temperature thermometers is their stability. A strategy commonly applied to increase the temperature range is to encapsulate the particles with a thin inert shell. Geitenbeek *et al.* used NaYF₄:Yb,Er nanocrystals with a diameter of ~20 nm and coated them with a 10 nm thick silica shell. This protection layer stabilizes the particles from room temperature up to 900 K.¹⁰⁵ To increase the measurable temperature range, particles that exhibit multiple optical transitions at high and low temperatures are selected. In doing so, Brites *et al.* achieved for Sr₂GeO₄ crystalline powders a detectable temperature range of 17 - 600 K through intra- and interconfigurational transition of Pr³⁺.¹²⁶

The spatial resolution of thermometry with fluorescent nanoparticles is constrained by the optical diffraction limit. However, if a single particle at a size below the diffraction limit can be precisely placed and its location be determined by other than optical means, the spatial resolution depends on the size of the particle. Aigouy *et al.* used a fluorescent nanocrystal attached to an AFM tip as shown in Figure 1.6a to measure the temperature distribution of an operating CMOS integrated circuit.¹⁰⁰

Color Center Defects

Color center defects in diamond, in particular the negatively charged nitrogen vacancy center, have been extensively investigated for nanoscale thermometry. Color centers are crystallographic point defects in an optically transparent crystal, where a lattice position is filled with one or more unpaired electrons. These electrons tend to absorb

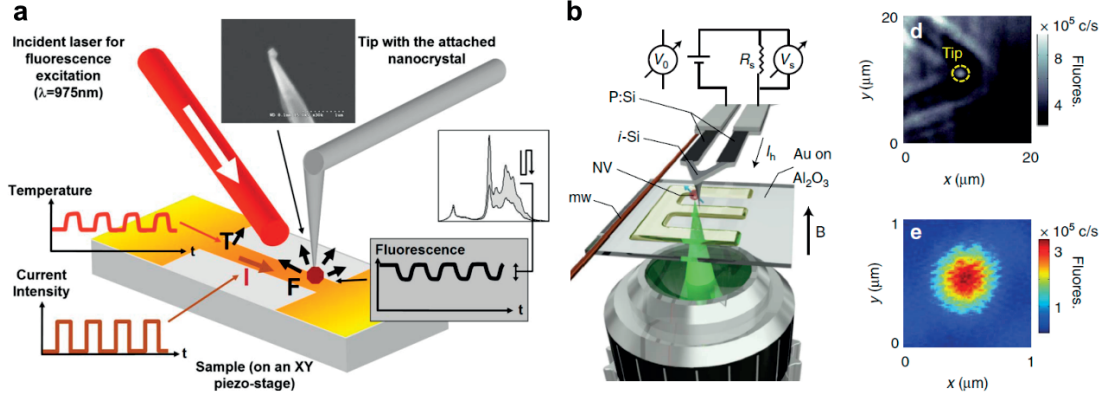


Figure 1.6 – Thermometry using fluorescent nanoparticles. **(a)** Measuring resistive heating of a microheater with an $\text{Er}^{3+}\text{Yb}^{3+}$ codoped nanoparticle on a tip. Reprinted with permission from [100]. **(b)** NV center thermometry with a heated scanning probe to measure the thermal conductivity of a substrate. Reprinted with permission from [111]

light, whereby the electrons are excited from the ground to a higher energy state and relax via emission of a photon.¹²⁷

The nitrogen vacancy (NV) color center has attracted great attention in the recent years due to its superior properties in terms of quantum yield (0.7-0.9)¹²⁸ and photostability.¹²⁹ The nitrogen vacancy is formed by substitution of a carbon atom in the diamond crystal lattice with a nitrogen atom and a lattice vacancy in the vicinity of the nitrogen atom.¹²⁹ In particular, the negatively-charged NV center (NV^-) is of interest for sensing temperature, pressure and magnetic fields. Typically, three optically-detectable, temperature-dependent signals are used for thermometry: (i) the fluorescence intensity, (ii) the optically detected magnetic resonance and (iii) the Debye-Waller factor. The emission intensity has been used to determine the temperature in a range from 300 to 670 K. It was found that the relative intensity of the photoluminescence linearly depends on the temperature, but varies considerably between different particles.¹¹⁰ A widely used property of the NV^- center is its optically detectable magnetic resonance (ODMR), which makes it possible to determine the NV^- center's temperature from the shift in the zero-field splitting (ZFS) with temperature. In a typical ODMR experiment, a diamond, which contains a single or multiple NV^- center defects, is illuminated with a green laser while a microwave field (MW) is applied with a nearby antenna. A decrease in the optical intensity of the NV^- center can be observed around 2.87 GHz at room temperature when the microwave field drives the spin transition between the $m_s=0$ and the $m_s=1$ spin states. The coupling coefficient of the shift is $\partial D/\partial T = -74$ kHz/K near room temperature. The ZFS shift as a function of temperature is due to thermal expansion and vibronic interactions, which shift the spin's energy levels.^{130–132} To improve the sensitivity of NV^- center fluorescence thermometry, the quantum coherence of single spins has been increased by applying deliberate laser and microwave pulse sequences, enabling a resolution down to 10 mK/Hz^{1/2}.¹³² Temperature imaging of photo-heated gold nanoparticles

1.3. Wide-Range Thermometry at the Nanometer Scale

with a diamond nanoparticle (~100 nm in diameter), which was mounted on the apex of a AFM tip, has been performed over a temperature range from room temperature to 40 °C.¹³³ Thermometry using diamond nanoparticles attached to a heated AFM tip has been used to measure the thermal conductivity of various substrates, such as diamond and glass as shown in Figure 1.6b.¹¹¹ Time-resolved luminescence thermometry at time scales of tens of microseconds on gold nanorods which were placed on a glass surface has been performed by measuring the temperature dependence of zero-field line of NV⁻ centers between room temperature and 110 °C.¹³⁴

While ODMR experiments require a microwave field to drive the spin transition, an all-optical approach has been proposed by Plakhotnik *et al.* They investigate the temperature dependence of the optical Debey-Waller factor, which is the ratio of the area under the zero phonon line and the total emission band. For temperatures larger than the Debey temperature $T \gg T_D$, the Debey-Waller factor can be modeled by an exponential $DWF = e^{-S(1+\frac{2}{3}\pi^2T^2/T_D^2)}$, where S is a parameter defining the electron-phonon coupling strength.¹³⁵ An upper limit of diamond for wide-range thermometry is its tendency to graphitize in air at temperatures between 600-700 °C.^{136,137} The physics of NV⁻ center thermometry will be further discussed in Chapter 4.

More recently, other color center defects have been explored as temperatures sensors, such as the germanium-vacancy color center¹³⁸ in an all-optical approach at a resolution of 0.1 K in a temperature range from 4 to 400 K, or the silicon-vacancy color center at temperatures between 290 and 300 K.¹³⁹ In NV⁻ center thermometry, external magnetic fields can interfere with temperature measurements. In a recent publication, neutral divacancy-defect spins in silicon carbide have been investigated in the temperature range from 20 to 300 K as thermometers, which possess a self-protecting mechanism against magnetic noise.¹⁴⁰

1.3.2 Conclusion

To date, a broad range of nanoscale thermometry techniques exist. Every technique has its unique advantages for specific applications. In this work, nanoparticles containing NV⁻ centers are chosen for tip-based thermometry due to several reasons: It can be operated at ambient pressure and can be used in a temperature range from room temperature up to 700 K and is well described in literature. Nanodiamonds with high densities of NV⁻ centers are commercially available down to a diameter of 20 nanometers,¹⁴¹ in contrast to many lanthanide based nanoparticles, which would have to be synthesized. The temperature signal can be decoupled from the illumination intensity of the laser or the collection efficiency of the measurement setup and can be monitored live during operation of the probe. A further advantage of using particles as probes, is that they can be placed at different locations, such as at the tip apex to measure the tip temperature¹¹¹ or on the substrate to measure the substrate temperature when approaching with the tip.

A further motivation to use NV⁻ center thermometry is that future thermal probes could be made out of diamond,¹⁴² due to the possibly high thermal conductivity of diamond at the nanometer scale compared to silicon¹⁴³ and its superior resistance to wear.¹⁴⁴ Incorporation of NV⁻ centers at the tip apex, would add even more functionality to the probes as nanoscale sensors.¹⁴⁵

1.4 Thesis Outline

In this thesis, two materials are investigated for the use as thermal scanning probe resists, whereby fast heating and cooling rates of t-SPL are a key parameter. In a second part, an approach towards a versatile nanometer scale thermometer for in-situ temperature measurements is presented.

In Chapter 2, a fluorescent supramolecular glassy polymer, which exhibits two distinct fluorescence states, is modified with a thermal scanning probe. Due to fast heating and cooling of the supramolecular polymer with the thermal probe on the order of 10^8 K/s, the high-temperature green fluorescent state can be quenched and micro- to nanoscale fluorescent patterns can be created with the scanning probe.

In Chapter 3, silk fibroin as a biocompatible material is investigated as a resist for t-SPL, whereby also here the fast heating and cooling plays a crucial role to induce a solubility contrast in the material.

Chapter 4 presents a setup for nanometer-scale temperature measurements using fluorescent nanodiamonds containing NV⁻ center defects. Preliminary results on NV⁻ center based thermometry are presented and discussed.

The last chapter concludes the thesis and gives a brief outlook for future work in the field of thermal scanning probe lithography and nanometer scale thermometry.

2 t-SPL of a Stimuli-Responsive Fluorescent Supramolecular Polymer

Parts of this chapter have been published in ACS Applied Materials and Interfaces.¹⁴⁶ After the manuscript was published, I discovered a mistake in the fitting of the Williams-Landau-Ferry equation to the experimental data, which requires a correction to the manuscript. A corrigendum will be communicated to the journal and the corresponding parts have been corrected in the results presented here.

2.1 Introduction

Supramolecular glassy polymers are an emerging category of stimuli-responsive materials that exhibit a high elastic modulus at room temperature in the solid state.^{147–149} These materials can be converted into low-viscosity liquids when heated above their glass transition temperature (T_g) on account of the thermally driven reversible disassembly into the parent low-molecular-weight building blocks.¹⁵⁰ Supramolecular polymers find applications in the field of sensing¹⁵¹ and self-healing.¹⁵² The concept of supramolecular polymers has been recently extended to mechanoresponsive luminescent (MRL) and thermoresponsive luminescent (TRL) supramolecular polymers by synthesizing a MRL/TRL dye with supramolecular binding motifs. Self-complementary hydrogen-bonding ureido-4-pyrimidinone (UPy) groups were used to promote the self-assembly¹⁵³ of an excimer-forming cyano-substituted oligo(p-phenylenevinylene) (cyano-OPV) derivative^{154–156} into a supramolecular polymer (UPy-OPV-UPy, Figure 2.1a).¹⁵⁷ This material has the following characteristics: (i) it can be readily molded into self-supporting objects of various shapes, (ii) it displays the thermomechanical characteristics of a supramolecular glassy polymer, (iii) it offers three different emission colors in the solid state, and (iv) it exhibits both MRL and TRL behavior due to stimuli-induced modification of the molecular packing, which in turn impacts the material's emission characteristics (Figure 2.1b).¹⁵⁷

While the ability to control the fluorescence color of blends of cyano-OPVs and glassy amorphous polymers via the extent of dye aggregation was exploited before in three-

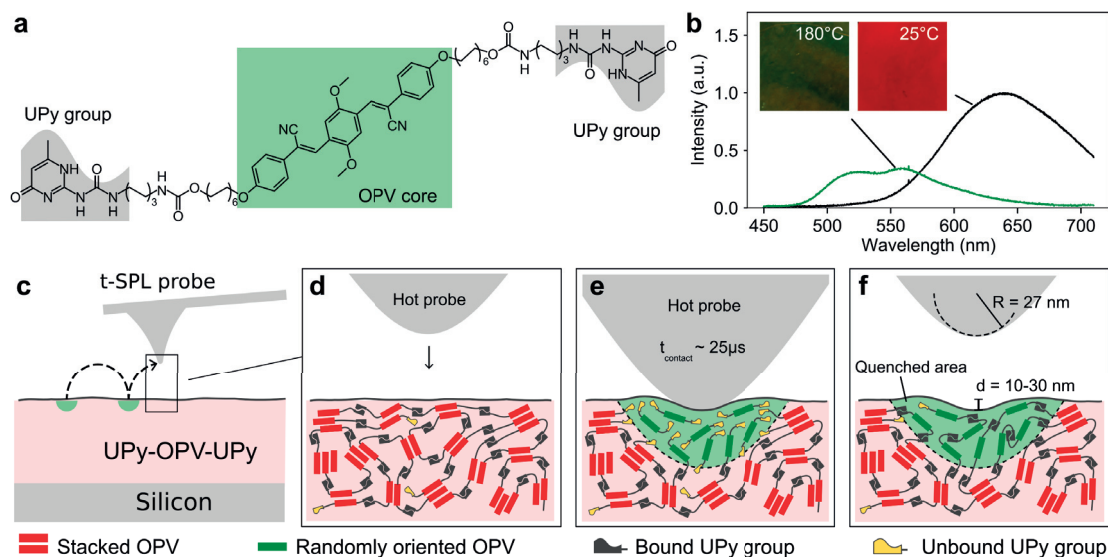


Figure 2.1 – Nanolithography with a color-switchable fluorescent supramolecular polymer resist. (a) The chemical structure of the UPy-OPV-UPy building block is shown, with the excimer-forming fluorescent OPV core and the supramolecular UPy binding motifs highlighted. (b) Fluorescence spectra of a bulk sample of UPy-OPV-UPy at 180 and 25 °C with two insets of the sample under UV illumination. (c) Schematic representation of the single-step fabrication of multicolor patterns using t-SPL. (d) Illustration of the polymer film topography and molecular assembly, with the OPV cores aggregated in excimer-forming stacks and the UPy binding motifs dimerized. (e) Indentation with a hot t-SPL probe locally liquefies the material due to dissociation of the building blocks, which results in a green fluorescence. (f) Upon rapid probe removal, the high-temperature state is quenched so that a green fluorescent area is retained.

dimensional optical data storage systems, heat-transfer processes did not permit a voxel with dimensions of less than a few micrometers.¹⁵⁸ In a more recent publication, a quaternary data storage system using thermoresponsive cyano-OPV and a photoresponsive dye in a polymer matrix was proposed to create a material selectively responsive to heat and light.¹⁵⁹ While this material allowed four different colors to be obtained under activation with light, heat, or a combination of both, the resolution was limited to 200-300 μm . To overcome such limitations in resolution, the capability of t-SPL to apply extremely fast heating rates on the order of 10^8 K/s is exploited. In addition, well controlled mechanical forces in the range of 200-500 nN at the probe-sample contact point are exerted simultaneously. This concept is demonstrated by reversibly switching the state of assembly and therefore the fluorescence characteristics of UPy-OPV-UPy under extremely short heat and force pulses created by a heated t-SPL probe (Figure 2.1c-f). It is hypothesized that kinetic trapping of the green fluorescent high-temperature OPV dissociated state is facilitated due to short contact and fast heat dissipation after the heated probe is removed.

In the following sections, the results on atomic force microscopy (AFM) force spectroscopy of UPy-OPV-UPy films, nanoindentation and nanopatterning by t-SPL, and the maximum achieved resolution are presented. Applications of the supramolecular polymer as multi-level fluorescent/topographical anticounterfeiting nanosystems are presented as well as UPy-OPV-UPy's capability of reversible patterning for data storage applications.

2.2 Materials and Methods

2.2.1 Sample Fabrication

UPy-OPV-UPy was synthesized as previously described and an in-depth structural characterization of the molecule was recently reported.⁷⁵ Films for the studies were fabricated by melting UPy-OPV-UPy in powder form on a silicon chip mounted on a hot plate at 180 °C and doctor-blading the hot melt over the substrate. The samples were then cooled under ambient conditions (1.3 °C/s) to room temperature, thus allowing sufficient time for the cyano-OPV moieties to aggregate into their thermodynamically favored stacked arrangement. Alternatively, and in order to obtain smooth and uniform samples, the supramolecular polymer was hot-pressed with a poly(dimethyl siloxane) (PDMS) coated silicon chip, which was found not to be sticking to the melt. The chip with the stamp was cooled at room temperature and then removed from the sample. As expected, cooling was accompanied by a fluorescence shift from green to red owing to the aggregation of cyano-OPV as depicted in the spectra and images in Figure 2.1b. The thickness of the resulting films was $20 \pm 10 \mu\text{m}$, as measured by a mechanical profilometer (Alpha-Step 500, KLA-Tencore, USA). The large deviation in film thickness between different films originates from the manual fabrication and could be improved by using a hot-press with pressure control at the expense of the simplicity of the manual coating. Despite the occurrence of thickness variations on the order of hundreds of nanometers over the entire sample, the surface of the films was smooth over an area relevant for t-SPL. A typical root-mean-square surface roughness of $5.7 \pm 3.0 \text{ nm}$ was measured over an area of $50 \times 50 \mu\text{m}^2$.

2.2.2 AFM Force Spectroscopy

Before t-SPL experiments are performed and to determine the thermomechanical properties of UPy-OPV-UPy films, AFM force spectroscopy on heated samples was performed using a Nano Wizard II AFM tool (JPK Instruments AG, Germany) equipped with a cantilever for nanoindentation (DNISP, Bruker AFM Probes, USA) and a heating stage (HTHS, JPK Instruments AG, Germany). The samples were heated from 20 to 75 °C as monitored with an Optris PI infrared camera. Between each temperature change, enough time was given for the UPy-OPV-UPy film to thermally equilibrate until the temperature reached a steady state. An indentation depth of 30 nm was targeted for the

AFM force spectroscopy measurements on the bulk-heated sample so that it matches typical values used hereafter in t-SPL. The force-distance curves were analyzed (JPK Software) and all force spectra were corrected for cantilever deflection. The unloading part of the force-distance curves were fitted (upper 50% of the curve) and analyzed according to the Hertz theory to obtain the elastic modulus.

2.2.3 Thermal Scanning Probe Indentation and Lithography

After the nanoindentation experiments with a cold probe and the sample on a hot plate, experiments with a heated probe on a sample stage that is kept at room temperature are performed. t-SPL was carried out using a commercial tool (NanoFrazor, SwissLitho AG), which controls a silicon cantilever (Frazor-HPL1, Swisslitho AG) with an integrated heater in close proximity to the tip for thermal patterning. UPy-OPV-UPy-coated silicon chips were mechanically clamped to the XY piezoelectric positioning stage of the tool with a metallic pin, which served as an electrical contact required for electrostatic actuation of the cantilever to exert the local force between probe and substrate. The governing patterning parameters for the t-SPL process, temperature, force, and heating time were investigated for UPy-OPV-UPy by consecutive variation of a single parameter in a series of experiments as shown in Figure 2.6. The material response was determined by scanning the patterned surface and evaluating the depth of the indent and the height of the rim formed around the indent (pileup). A script was written that computes the average depth of the indents and the height of the pileup from the AFM topography scan (as described in Section 2.2.5). The t-SPL tool was operated in pulsed heating mode, whereby the heating of the tip occurred only shortly before and during contact with the substrate; this procedure increases the tip lifetime and also the thermal patterning reliability on the supramolecular polymer. Typical settings for heat pulses and electrostatic force pulses were 5-20 and 5-10 μs , respectively. The patterning speed was varied between 200 and 800 $\mu\text{m/s}$.

2.2.4 Estimation of the Contact Temperature

To explain the response of the sample to thermomechanical indentation, the material temperature is of great interest. However, the temperature at the contact between the polymer and the tip apex is not *a priori* known and has to be calculated based on a model as depicted in Figure 2.2. The model assumes that if the heater and substrate temperature and the thermal resistances are all known, the temperature at every interface can be computed. Typically, the substrate temperature and the temperature of the resistive heater can be measured. In the t-SPL tool, the heater temperature is automatically computed by the software by fitting the knee point, the temperature at which the resistance is highest in a current-voltage experiment, with the theoretical value for doped silicon.¹⁶⁰ A newer version of the NanoFrazor software (version 2.7) uses the electrical

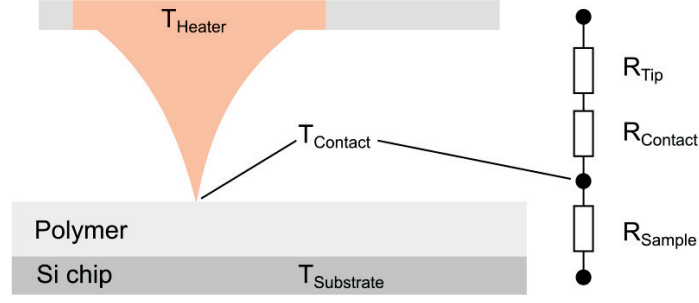


Figure 2.2 – Thermal resistance model for the heat transfer between a heated AFM probe and a sample. The model for calculating the tip-sample contact temperature, based on the thermal resistance of the tip, the tip-polymer contact and the sample is used, as drawn on the left side.

power dissipated in the cantilever as a calibration to determine the heater temperature, which reduces the measurement error to less than 25 K over the whole temperature range from room temperature to 1100 °C.¹²⁴

The thermal resistance of the tip R_{Tip} is dominated by phonon boundary scattering at the lower end of the cone, where its diameter is on the order of the mean free path of phonons in silicon. Typical values are between $10^7 - 10^8$ K/W.¹⁶¹ The contact resistance $R_{Contact}$ highly depends on the effective contact area and the thermal boundary resistance, which originates from not perfectly smooth surfaces. Experimentally measured values of the boundary resistance are between $5 \cdot 10^{-9}$ and $5 \cdot 10^{-8}$ m²K/W.¹⁶² The thermal spreading resistance typically depends on the contact diameter of the tip, the thickness of the resist and the thermal conductivities.¹⁶² From the thermal resistances and the temperatures at the heater and the substrate, the contact temperature can be calculated as follows:^{161,162}

$$T_{Contact} = c \cdot (T_{Heater} - T_{Substrate}) + T_{Substrate} \quad (2.1)$$

where the heating efficiency c is the ratio of the thermal resistances:

$$c = \frac{R_{Sample}}{R_{Tip} + R_{Contact} + R_{Sample}}. \quad (2.2)$$

The heating efficiency for a polymeric substrate and a silicon probe was estimated between 0.4 and 0.7.^{161,162} The broad range of values for the heating efficiency imposes a large uncertainty on the contact temperature. In the following experiments, we use a heating efficiency of $c = 0.5$ as chosen for similar polymers and probes.³⁶

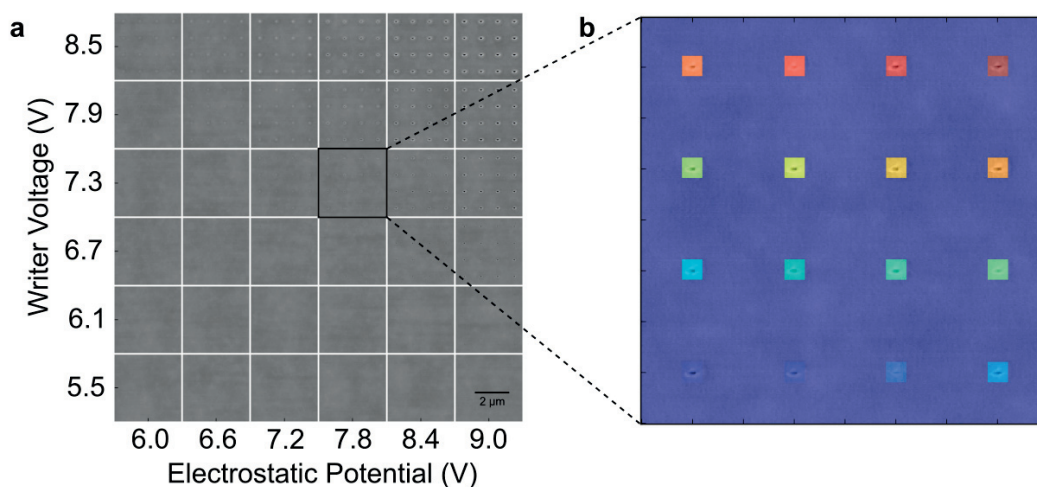


Figure 2.3 – Automated detection of indents. (a) Collection of 36 topography images obtained from t-SPL patterning at 6 different tip temperatures (writer voltage from 5.5 to 8.5 V) and indentation forces (electrostatic potential between cantilever and substrate: 6.0 to 9.0 V) (b) Magnification of one topography image with 16 labeled indents as detected by the computer.

2.2.5 Evaluation of Thermomechanical Indents

The threshold temperature at which a material change can be detected by AFM upon indentation with the heated probe was determined by performing a series of indents at different indentation forces and heater temperatures as shown in Figure 2.3a. The recorded AFM topographies of the indents were then analyzed using a software script, which detects the indents as shown in Figure 2.3b and extracts the height of the pileup and the depth of each indent. For a set of 16 indents, the average value and the standard deviation of the indent depth and pile-up height are computed.

2.2.6 Indentation Force Calibration of Electrically Actuated Cantilevers

Currently in the commercial t-SPL tool, the indentation force is controlled by setting a voltage for the electric potential between cantilever and substrate, which actuates the tip towards the sample. In order to convert the voltage into an indentation force, the cantilever must be calibrated. The strategy employed here to experimentally measure the deflection of the cantilever as a function of applied potential and temperature, is to place the cantilever at a well defined distance away from the sample surface and increase the voltage until the tip touches the substrate. Since the cantilever deflection depends also on the temperature due to a bimorph bending, the calibration needs to be performed in the corresponding heater temperature range. For calibration a simplified mechanical model for the patterning force similar to Holzner *et al.*¹⁶¹ is employed. The main difference is that the commercial tool does not allow a direct readout of the cantilever bending as

a function of the applied voltage and temperature as in the reference. Therefore, the calibration procedure is modified as described in the following. The electrostatic force that bends the cantilever towards the substrate is in first approximation proportional to the square of the applied potential $F_{el} \propto V^2$. According to Hook's law, the restoring force due to the bending Δz of the cantilever is $F_k = k_s \Delta z$ with k_s being the spring constant of the cantilever. For the type of cantilevers used in this work, the spring constant is typically 0.9 nN/nm and is assumed to be linear for deflections in the range from 50 to 450 nm.¹⁶¹ Knowing the spring force and the deflection of the cantilever, the magnitude of the electrostatic force can be found at the equilibrium position of the cantilever according to Newton's law $\Delta z k_s + F_{el} = 0$. In a real experiment however, the electrostatic force acting on the cantilever is a complex function due to its geometry and additional contribution to the bending due to heating of the tip has to be included $\Delta z \propto T^2$. As a consequence, the deflection of the cantilever has to be experimentally determined for different forces and temperatures, and fitted to a model as shown in Equation (2.3) in order to compute the indentation force.¹⁶¹

$$\Delta z(V, T) = f_v(V - f_{V,offset})^2 + f_T(T - T_{RT})^2 \quad (2.3)$$

where f_v , $f_{V,offset}$ and f_T in the equation are the fitting parameters. In contrast to Holzner *et al.* where the cantilever bending was detected with a sensor, here PPA serves as a means to detect when the tip touches the substrate. Since it volatilizes via self-amplified decomposition upon heating, a mark is created when the tip touched the surface.^{21,22} For the calibration procedure, the cantilever was positioned at a distance of 450 nm between the tip apex and a silicon chip, which is coated with a \sim 300 nm thick layer of PPA. A pattern composed of indents as shown in Figure 2.3b is written with the t-SPL tool at an electrostatic potential V starting from 2 V and a cantilever temperature starting from 650 °C. After this, the sample is scanned with the cold tip in AFM mode and if no indent is detected, the procedure is repeated with a higher V until an indents is detected. The electrostatic potential at which the tip is in contact with the substrate and a mark in the polymer is detected is plotted as one data point in Figure 2.4a. The procedure is then repeated for smaller tip-sample distances down to 80 nm and higher temperatures up to 920 °C. By doing so, a set of data points for $\Delta z(V, T)$ as a function of V and T is obtained as shown in Figure 2.4a. The data is fitted to Equation (2.3) using a numerical optimization package (*scipy*). The parameters for the model which describe the measurements best are $f_v = 7.80 \pm 0.06$ nm/V², $f_{V,offset} = 0.8 \pm 0.3$ V and $f_T = 2.0 \pm 0.1 \cdot 10^{-4}$ nm/K² with a corresponding $R^2 = 0.97$. The fitted curves are plotted in Figure 2.4a in solid lines. The patterning force, which is the force pulling the tip into the sample is then the difference between the electrostatic force and the spring force, which is necessary to pull the cantilever into contact: $F_{patt} = F_{el} - F_{contact} = k_s \Delta z(V, T) - k_s z_{piezo}$ where z_{piezo} was 200 nm for all experiments performed. Figure 2.4b shows the patterning

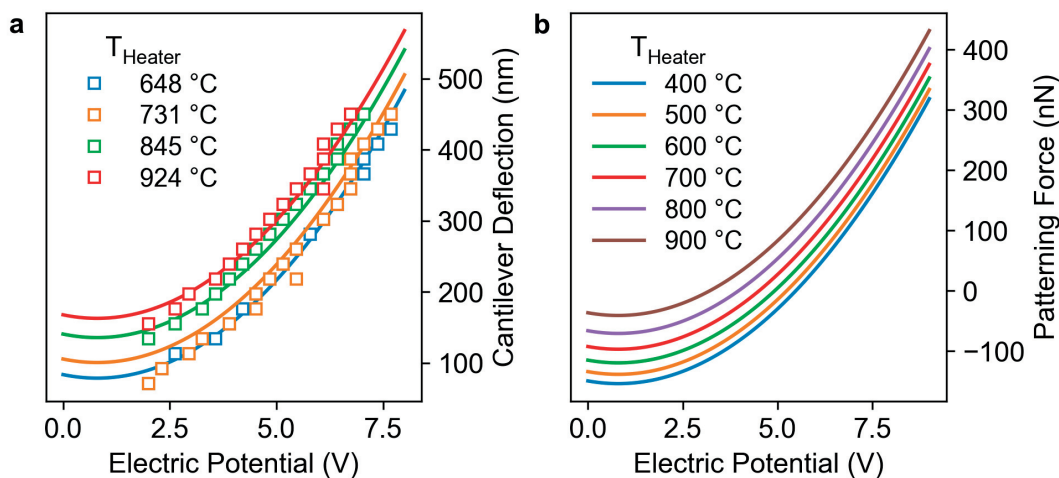


Figure 2.4 – Calibration of the indentation force by detection of cantilever deflection. (a) Plot of the cantilever deflection as a function of the electrostatic potential between tip and substrate for different tip temperatures and the corresponding fitted curve (not all curves plotted for better visibility). (b) Plot of the computed patterning force as a function of the electric potential between tip and substrate for different temperatures. A negative patterning force means that the tip is not in contact with the substrate.

force as a function of the electric potential for different temperatures, whereby a negative patterning force means that the deflection due to the electrostatic force is not large enough to touch the substrate. It can be noted that the method mentioned here neglects effects such as the interaction of the tip with the substrate while in contact and that not all tips have the same spring constant due to variations in geometry which occur naturally in the fabrication process. Nevertheless, the model represents the order of magnitude of the governing forces and displays the relation between indentation force, electric tip actuation potential and heater temperature. Similar indentation forces in the range from tens to hundreds of Nanonewtons have been reported in the literature.^{44,161}

2.2.7 Fluorescence Microscopy

Optical fluorescence microscopy images were acquired with an Olympus BX51 microscope, equipped with a mercury lamp at a wavelength of 365 ± 15 nm (I-line) as an illumination source; the emission was detected at wavelengths larger than 420 nm. The illumination intensity of the fluorescence microscope was carefully adjusted to a level where no bleaching occurred.

For a better contrast of the fluorescence images, a short-pass filter was used to block the red background fluorescence from the unmodified supramolecular UPy-OPV-UPy. To demonstrate the benefit from a short-pass filter, an unfiltered fluorescence image in Figure 2.5a is compared with a filtered image in Figure 2.5b. The contrast of fluorescence

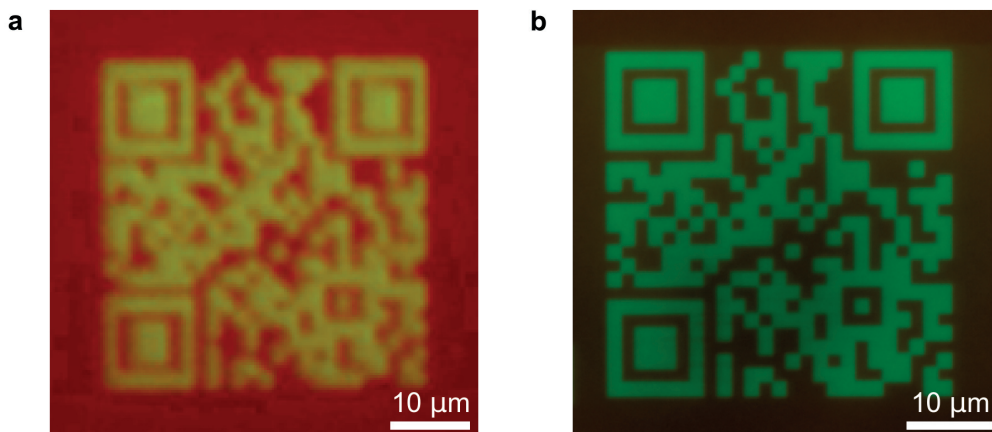


Figure 2.5 – Proof-of-concept thermal patterning of a fluorescent structure. **(a)** Corresponding fluorescence image shows a weak contrast between modified (green fluorescent) and pristine (red fluorescent) substrate. **(b)** Corresponding fluorescent structure with a red filter to enhance the contrast.

images was normalized by means of an editing program (GIMP, www.gimp.org), for better visibility. All written t-SPL patterns were labeled by an adjacent pattern to be clearly visible by optical microscopy for identification during fluorescence microscopy.

2.3 Results and Discussion

2.3.1 Thermomechanical Indentation

While thermomechanical properties, such as the temperature-dependent elastic modulus and the glass-transition temperature, for relatively thick (2 mm) UPy-OPV-UPy films have been discussed in a previous publication,¹⁵⁷ no thermomechanical data is available for nanoindentation of melt-processed films and fast heating rates as is achievable in t-SPL. Since the tip temperature in t-SPL is not *a priori* known and the tip geometry is not well-defined, here both conventional AFM force spectroscopy and t-SPL are performed as a comparison to determine the thermomechanical properties of the supramolecular polymer. The elastic modulus of $20 \pm 10 \mu\text{m}$ thick UPy-OPV-UPy films measured by AFM-based force spectroscopy is shown in Figure 2.6a as a function of the substrate temperature. An elastic modulus of 1.5 ± 0.2 GPa is measured at 20 °C. The modulus linearly decreases with increasing substrate temperature until 68 °C, where it sharply drops by a factor of 20 to 10.5 ± 2.5 MPa. Above 73 °C, indentation experiments were no longer possible due to adhesion of the viscous melt to the tip. The AFM force spectroscopy results mirror the measurements on bulk UPy-OPV-UPy films.¹⁵⁷

In addition to the above-mentioned experiments with a cold probe and a heated substrate,

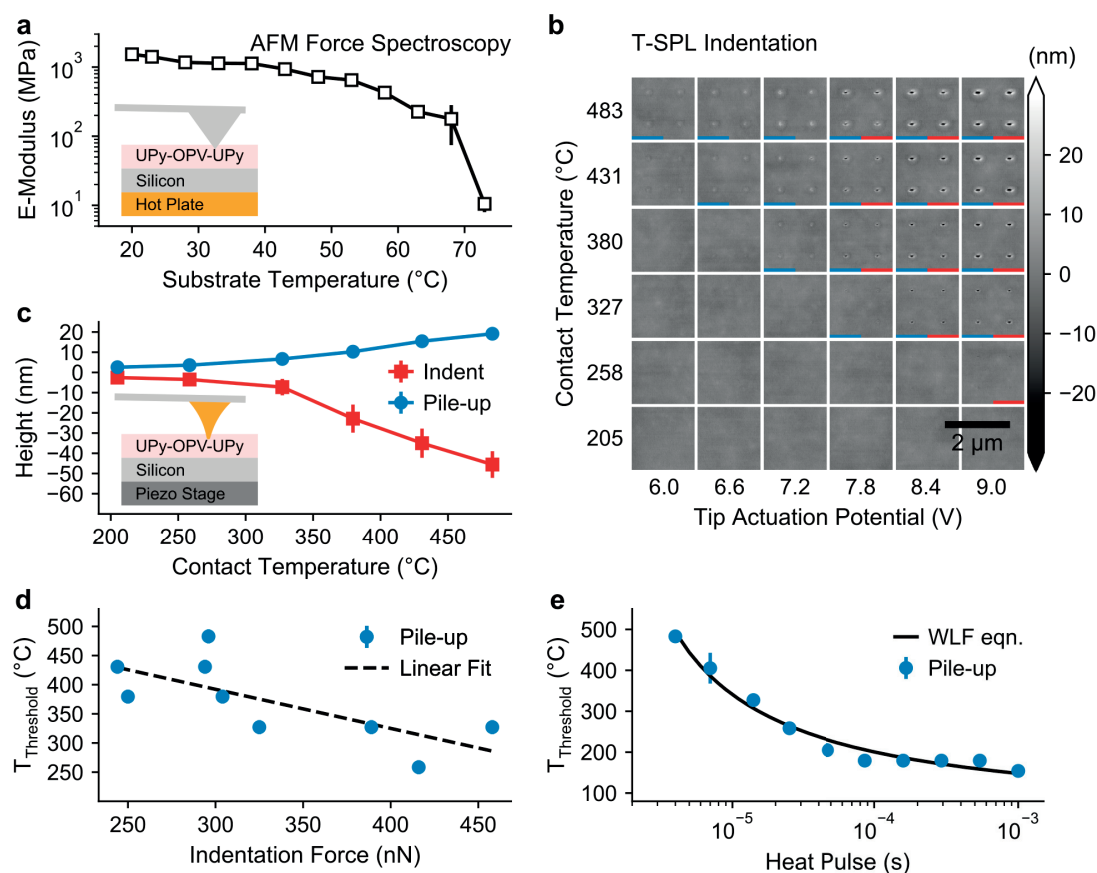


Figure 2.6 – Thermomechanical indentation of the TRL supramolecular polymer. **(a)** The elastic modulus of $20 \pm 10 \mu\text{m}$ thick UPy-OPV-UPy films obtained from AFM-based force spectroscopy is plotted against the sample temperature. The inset depicts the experimental setup. **(b)** AFM topography images obtained from t-SPL indentation by varying the tip temperature between 200 and 500 °C and the indentation force between 200 and 500 nN (tip actuation potential 6.0-9.0 V). The colored bars indicate whether an indent was formed (*red*) or a pileup (*blue*). **(c)** The indentation depth and height of the pileup around the indent from thermomechanical indentation with a hot probe are plotted against the tip temperature. **(d)** The threshold temperature above which a pileup is formed is plotted against the indentation force and fitted with a linear function. **(e)** The temperature threshold to form a pile-up is plotted against the heating time and fitted using the Williams-Landel-Ferry equation for a constant tip actuation potential of 7.8 V.

a heated t-SPL probe and a sample at room temperature are used to test the thermomechanical properties of UPy-OPV-UPy. In a series of experiments, the indentation depth was measured as a function of probe temperature, indentation force, and heating time. Figure 2.6b shows a grid of AFM topography images obtained from t-SPL indentation, which were created at tip-sample contact temperatures in the range of 200-500 °C and a tip actuation potential ranging from 6.0 to 9.0 V, which corresponds to an indentation

force of 100-500 nN. The contact temperature was calculated from Equation (2.1) using a heating efficiency of 0.5. Two main observations can be made from Figure 2.6b: first, to thermally modify the supramolecular polymer with the heated probe, a minimum temperature (threshold temperature) is necessary at a given tip actuation potential; second, if the tip actuation potential is below 7.8 V, only a pileup is formed, whereas at higher voltages an indent with a surrounding rim can be observed. A small colored bar at the bottom of each topography image in Figure 2.6b indicates whether an indent (*red*) or a pileup (*blue*) is formed. The formation of a pileup without an indent can be attributed to a sufficient high temperature to melt the material but a force too low to penetrate it.

In Figure 2.6c, the average indent depth and height of the pileup from 16 indents are plotted as a function of the tip temperature at a tip actuation potential of 7.8 V and a heating time of 8 μ s, which is a trade-off value between patterning speed and temperature as will be explained later. The indentation depth increases with temperature above 320 $^{\circ}$ C and as a consequence the pile-up height increases due to displacement of the molten material. To systematically detect this temperature by AFM, we define a threshold value for the indent depth and pile-up height of 4 times the root-mean-square roughness of the sample topography, which is usually in the range between 3 and 6 nm. The threshold value is chosen sufficiently high to avoid false positive detection of an indent or pileup. The indentation experiment as shown in Figure 2.6b was performed ten times with the same tip on different samples. All patterns were clearly visible and the indents well reproduced. Three experiments were discarded due to surface topography anomalies, which stem from the manual sample fabrication and caused large variations in the data points. These surface irregularities can be avoided in future experiments by using compression molding of UPy-OPV-UPy on a substrate instead of doctor-blading the melt. In Figure 2.6d, the average threshold temperature from the seven consecutive indentation experiments is plotted as a function of the indentation force. The temperature necessary to form a modification in the material T_{Thres} decreases linearly with the indentation force F : $T_{Thres}(F) = 590 \text{ }^{\circ}\text{C} - 6.7 \text{ }^{\circ}\text{C/nN} \cdot F$. A linear dependence between threshold temperature and indentation force has been observed for polymers.³⁶

To determine the effect of heating time on the threshold temperature, the tip-substrate contact time was varied over 3 orders of magnitude as shown in Figure 2.6e. As expected, the temperature required to induce a material deformation decreases with the heating time, known as time-temperature superposition, which is a typical behavior found in polymers. The study shows that also in supramolecular polymers, which differ considerably in their molecular assembly from regular polymers, the temperature T at which material softening occurs during thermal indentation can be described by the empirical Williams-Landel-Ferry (WLF) equation: $\ln(t_T/t_r) = -c_1(T - T_r)/(c_2 + (T - T_r))$, with a heating time t_T and a reference time t_r at a reference temperature T_r . The curve was best described with $c_1 = 3.6 \pm 0.6$ and $c_2 = 238 \pm 4 \text{ }^{\circ}\text{C}$ at a reference temperature of $T_r = 270 \text{ }^{\circ}\text{C}$, similar values to that have been found for thermal indentation with PMMA and SU-8.³⁶ These

findings confirm that supramolecular polymers follow WLF behavior over a temperature range from 200 °C to 500 °C.

2.3.2 Correlation Between Pitch Size and Pattern Quality

Thermal patterning of polymers with a low degree of cross-linking by t-SPL is challenging due to softening of the polymer, which leads to plastic deformation around the indent and adhesion of viscous melt to the tip.⁴¹ For the supramolecular polymer, it was found that the pitch size is a crucial parameter to obtain reproducible patterns. Figure 2.7 shows AFM topographies of patterns that have been written at pitch sizes from 20 to 100 nm. One can observe in Figure 2.7a that at a pitch size of 20 nm, material is displaced in the fast scan direction (left to right). The trench at the left side of the square, the irregular surface and the pileup indicate that the tip displaced material in the fast scan direction. The pileup decreases with increasing pitch size up to 80 nm, where the individual indents become visible as shown in the magnified topographies in Figure 2.7b. Similar observations have been reported in a study which was investigating the limitations in storage density with thermomechanical probes.³³ Due to the finite size of the tip apex, during consecutive indentation at a pitch size which is smaller than the tip apex diameter, material is displaced into the previous indent. For an indent depth of 70 nm, it can be estimated that for a tip opening angle of 30°, overlap of indents occurs below a pitch of 37 nm. However, due to softening of the material around the indent, the effective size of the thermoplastically deformed area is larger than the theoretical indent. From the observations, a model for the indentation and the displacement of material is sketched in Figure 2.7c. At a pitch between 20 - 40 nm at an indentation depth of 70 nm, after each indent, some plastically deformed material from the pileup around the previous indent is dragged in the scan direction, which leads to inhomogeneous patterns. A transition occurs at a pitch around 60 nm where the neighboring indents are partially filled due to the deformed material or due to reflow from heating. At larger pitch sizes, clearly separated indents are formed without displacement of the pileup. It can be concluded that the same limitations in terms of indent density apply for the supramolecular polymer as described for other polymers.³³

2.3.3 Correlation Between Fluorescence Intensity and Pitch Size

In the previous section, the effect of pitch size on the pattern quality was investigated. It was found that for a pitch larger than 60 nm, reliable patterning can be achieved. Since the resolution of the fluorescence contrast created between the thermally modified and the unpatterned area is diffraction limited, features smaller than 250 nm cannot be resolved by optical microscopy. This provides a degree of freedom between 60 and 250 nm to modify the fluorescence intensity of the green emission. In the following section, the variation in green fluorescence intensity is investigated as a function of the pitch size and

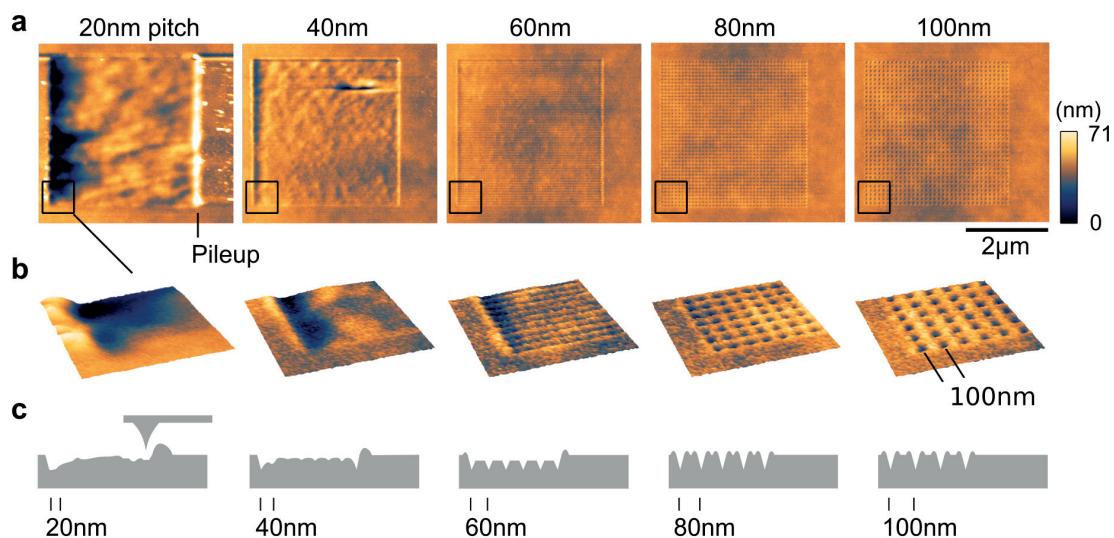


Figure 2.7 – Influence of the indent distance on the quality of patterns. **(a)** AFM topography images of squares written by t-SPL into the UPy-OPV-UPy resist, using indent distances between 20 and 100 nm. **(b)** Magnified 3D topography images reveal the transition from plowing with the tip towards visibility of individual indents by increasing the spacing between individual indentations. **(c)** Schematic representation of the thermal indentation process and the influence of the indent distance on the topography.

a model is developed which describes relation between the two.

Areas of the supramolecular polymer film were written at a pitch size ranging from 20 nm to $2.56 \mu\text{m}$ and subsequently imaged directly by the NanoFrazor's probe, as shown in Figure 2.8a. A comparison between the topography and fluorescence image (Figure 2.8b) reveals that the green fluorescence intensity can be tuned over a broad range by varying the indent density, but the indentation pattern itself is not visible because the t-SPL resolution is higher than the diffraction limit of optical microscopy. The fluorescence intensity, normalized with respect to the intensity at a pitch of 20 nm, is plotted as a function of the pitch size in Figure 2.8c. The fluorescence intensity sharply decreases with increasing pitch and drops below 10% for pitch sizes above 400 nm.

The inset in Figure 2.8c show the surface topography of indents at a pitch of 320 nm and 160 nm. The FWHM sizes of the indents with a pitch of 320 nm are 93 ± 12 and 46 ± 6 nm in the fast-scan direction (*horizontal*) and in the slow-scan direction (*vertical*), respectively. The asymmetry of the indent can be explained with contaminations on the tip or an irregular shape of the tip cone from fabrication, since for other cantilevers the shape of the indents was circular. At a pitch of 160 nm, the shape of the indents becomes more circular since material is plastically deformed and pushed into the neighboring indents.

In the following, it is aimed to create a model that can explain the observed fluorescence

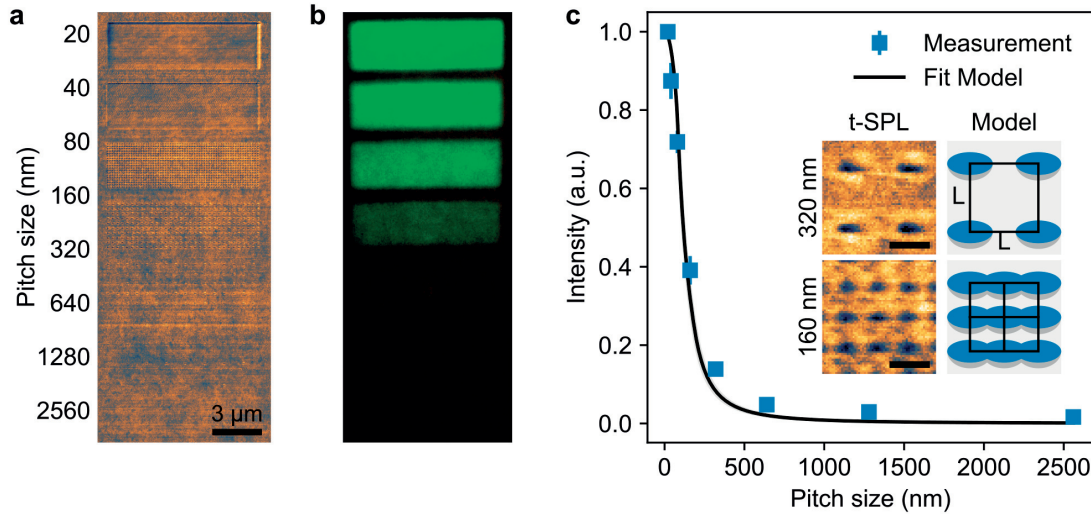


Figure 2.8 – Correlation between fluorescence intensity and pitch size. (a) AFM topography image for different indent pitch sizes varying from 20 nm to 2.56 μm. (b) Corresponding fluorescence microscopy images acquired during irradiation with UV light (scale bar 2 μm). (c) Plot of the normalized fluorescence intensity as a function of the pitch size. The inset shows the surface topography of indents at a pitch size of 320 and 160 nm and the corresponding model used to fit the green emission per unit area (scale bar 200 nm).

as a function of the pitch size and the indent geometry. It is assumed that the thermally modified volume is composed of the topographical indent and the surrounding material which was heated above the glass transition temperature and can be approximated with a semi-ellipsoidal shape. This assumption is justified by the elliptic shape of the indents measured from the AFM topography (Figure 2.8c inset). The amount of green fluorescence intensity per unit volume is the ratio between a semi-ellipsoid's volume and the volume of the unit cell as depicted in the insets in Figure 2.8c. As long as the half-pitch size $L/2$ is larger than the semi-major axis of the semi-ellipsoid, the intensity is inversely proportional to the square of the pitch size (Figure 2.8c at a pitch of 320 nm). If the half-pitch is smaller than the major axis, the ellipsoids start to overlap as visualized in the inset at a pitch of 160 nm. As a consequence, the overlapping volume does not contribute to further increasing the fluorescence intensity. In the limit of the pitch size approaching zero, the whole unit cell is filled and the normalized intensity is one. The following function is used to model the normalized fluorescence intensity as a function of the pitch size, and ellipsoidal shape:

$$I(L, a, b) = \frac{V_{\text{ellipsoid}}/8}{V_{\text{unit cell}}} \quad (2.4)$$

$$= \frac{4}{L^2} \int_0^{\min(\frac{L}{2}, a)} \int_0^{\min(\frac{L}{2}, \sqrt{1-(x/a)^2})} \sqrt{1 - \left(\frac{x}{a}\right)^2 - \left(\frac{y}{b}\right)^2} dy dx \quad (2.5)$$

where a and b are the two principle axes of the semi-ellipsoid, which are in plane. L is the pitch size and x and y are the integration variables. It should be noted that the normalized intensity is independent of the indent depth and hence the third principle axis does not appear in the equation. To numerically evaluate the integral and fit the fluorescence intensity, the numerical optimization package *scipy* was used. The model was fitted to the measured intensity with one free parameter, by fixing the ratio between a and b . The aspect ratio of the indents ($r_a = 2.2 \pm 0.6$) can be determined from the surface topography and should be similar for both, the topological indent and the fluorescent area, due to isotropic spreading of heat. The fitted curve is plotted in Figure 2.8c. From the fit on the fluorescence intensity, the indent length of 189 ± 12 nm can be extracted, which is in agreement with the value obtained by measuring the peak-to-peak indent length from the topography (184 ± 31 nm).

From the results presented above, one can draw two conclusions: first, the relative green fluorescence intensity of the supramolecular polymer can be controlled from 20% to 100% at pitch sizes below the diffraction limit of conventional optical microscopes and second, the disaggregation of the fluorophores due to the heat provided by the tip is confined to only a few nanometers around the indent and the resolution is mainly limited by the tip apex size. For future experiments, the intensity could be tailored by choosing different lattice geometries, such as a hexagonally packed lattice to increase the indent density, or to vary the indent depth, which affects the absolute intensity.

2.3.4 Spatial Resolution

Another essential benchmark for UPy-OPV-UPy as a thermal resist is the spatial resolution, which was determined by patterning structures composed of bars ranging from $1.92 \mu\text{m}$ in width down to a vertical line. The maximum resolution is governed by the lateral tip apex diameter (27.7 ± 9 nm), the opening angle (30°), and the indentation depth (10-30 nm). Figure 2.9a shows the AFM topography of the pattern obtained, whereby the patterned area can be distinguished from the unpatterned area due to an increase in the surface roughness. For a vertical line of consecutive indents at a pitch size of 20 nm, a FWHM resolution of 86 ± 6 nm is obtained. As a comparison to literature, in two-photon laser lithography the voxel size was previously limited to a volume of $3 \times 3 \times 6 \mu\text{m}^3$ due to heat diffusion from the heated spot.¹⁵⁸ In Figure 2.9b the corresponding fluorescence microscopy images of the pattern is shown.

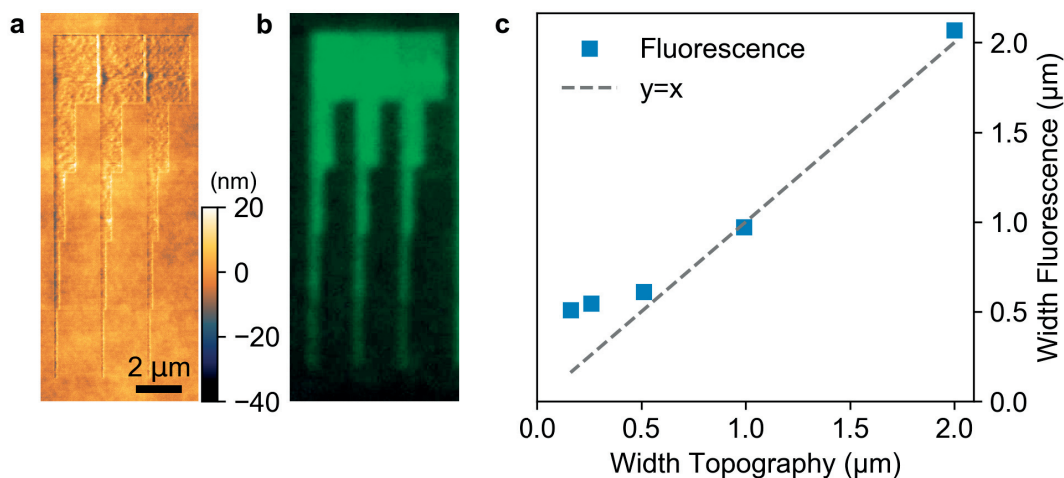


Figure 2.9 – Comparison of the resolution achieved by t-SPL patterning of the fluorescent supramolecular polymer and optical readout with a fluorescence microscope. **(a)** AFM topography image of patterns that were written with t-SPL with features ranging from a vertical line (86 ± 6 nm) to 1920 nm in width. **(b)** Fluorescence microscopy image of the same patterns acquired under irradiation with UV light. **(c)** FWHM width of the profiles extracted from the fluorescence intensity image plotted against the width obtained from the surface topography. The gray dashed line indicates the case where both measurements are equal.

To compare the resolution obtained by AFM and fluorescence microscopy imaging, in the graph in Figure 2.9c, the width of the patterns obtained from the surface topography and the fluorescence intensity image are plotted against each other. For 0.5-2 μm wide bars, the width measured from the topography and the fluorescence image are equal, but diverge below 500 nm due to the optical diffraction limit of the fluorescence microscope.

It can be concluded that the spatial resolution of patterns created with the thermal probe is, as expected, higher than the optical images. This opens the possibility to hide patterns at the nanometer scale which are not visible by optical means as will be discussed in the following section.

2.3.5 Hidden in Plain Sight

The combination of t-SPL with a color-switchable fluorescent polymer provides the ability to pattern multifaceted nanostructures, which are optically hidden due to the limited contrast or resolution of most optical microscopy systems but topologically detectable with AFM. To demonstrate this, a series of patterns were fabricated with distinct information in the topographic and fluorescent states by way of consecutive patterning steps and readout using both AFM and fluorescence microscopy. First, a square of $30 \times 30 \mu\text{m}^2$ was patterned with a pitch size of 60 nm (Figure 2.10a). Subsequently, a second pattern

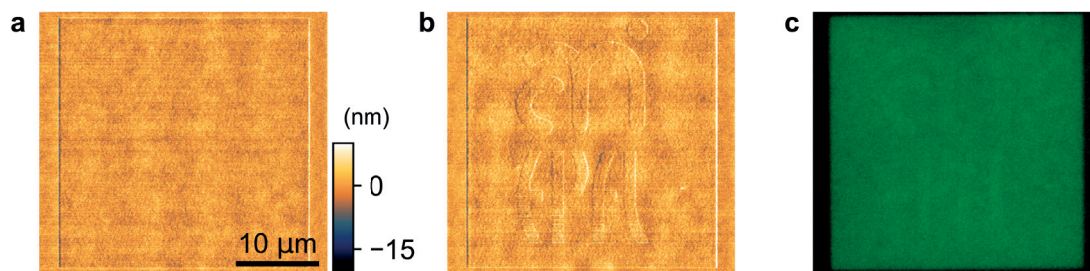


Figure 2.10 – Thermal patterning of nanoscale features with distinct topography but the same fluorescence intensity. **(a)** t-SPL patterning of the square of $30 \times 30 \mu\text{m}^2$ at a pitch size of 60 nm. **(b)** Overlay of a second t-SPL pattern within the prepatterned square, containing the logos of the two institutes *AMI* and *EPFL*. **(c)** Fluorescence microscopy image of the patterned area acquired under irradiation with UV light, showing that the second structures patterned by t-SPL are virtually invisible in fluorescence microscopy.

was produced within the square, which can be distinguished from the background by AFM (Figure 2.10b). However, as shown in Figure 2.10c, the second pattern is virtually indistinguishable from the background when measured with fluorescence microscopy. To obtain truly hidden features, it is important to avoid deep indents and pileup. To be able to see the features with a fluorescence microscope, the hidden t-SPL patterns are larger than $1 \mu\text{m}$, whereas in a real security feature, the information can be stored in the form of a binary pattern composed of indents and unpatterned areas at the size of a few tens of nanometers.

2.3.6 Fluorescence Change at Ambient Conditions

Figure 2.11 shows three samples of the supramolecular polymer on $120 \mu\text{m}$ thick coverslip glasses, which were cooled down at different conditions under UV illumination. The thin substrates were chosen to reduce the thermal mass of the substrate and allow fast cooling. The upper sample was heated to $180 \text{ }^\circ\text{C}$ on a hot plate until it was clearly green fluorescent and then let to naturally cool down to room temperature by removing it from the hot plate. The middle sample was heated up to $180 \text{ }^\circ\text{C}$ and immediately quenched in a bath of liquid nitrogen at $-196 \text{ }^\circ\text{C}$. The third sample at the bottom was taken from a hot plate at $180 \text{ }^\circ\text{C}$ and exhibits a green fluorescence.

Figure 2.11b and c show the same samples after 1 second and 3 seconds, respectively. The color of the hot sample at the bottom changes from green to yellow and then red within the 3 seconds. The color transition can be explained by a mixture of green and red fluorophores. By quenching the hot sample in liquid nitrogen, most of the UPy-OPV-UPy moieties recrystallized within a time period smaller than 3 seconds. It

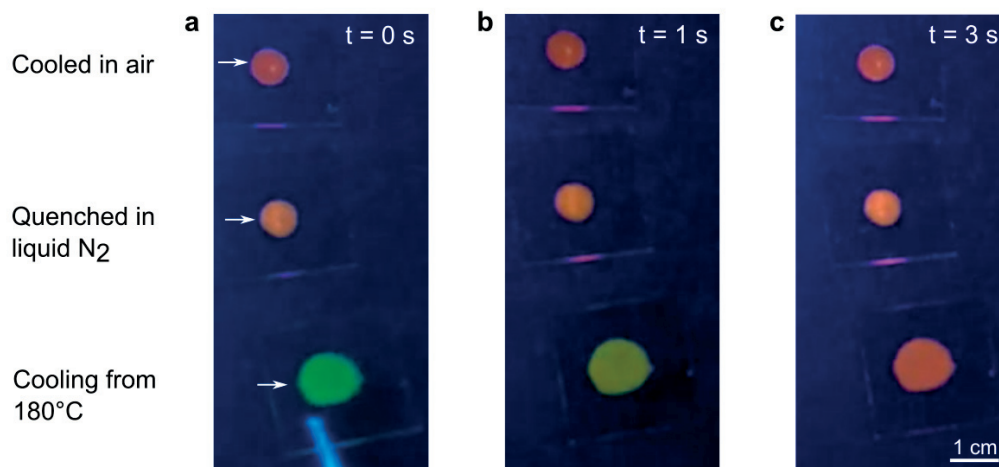


Figure 2.11 – Cooling of a fluorescent supramolecular polymer in air at room temperature and in liquid nitrogen under UV illumination. **(a)** The upper sample was heated to 180 °C and let cool at room temperature, the middle sample was heated to 180 °C and quenched liquid nitrogen to -196 °C and the bottom sample is taken from the hot plate and fluoresces in green. **(b)** The samples after 1 second where the bottom sample fluorescence color shifted to yellow and **(c)** after 3 seconds all samples are fluorescing in orange. One can observe that in the quenched sample the fluorophores did not aggregate to the same degree as the air cooled samples.

is difficult to estimate the cooling rate within the liquid nitrogen bottle, however it can be seen from the macroscopic sample, that the quench rate is not high enough for complete recrystallization. These experiments support the hypothesis that only the combination of high cooling rates and small volumes accessible by t-SPL enable trapping of the high-temperature state.

2.3.7 Reversible Thermomechanical Indentation

Due to the molecular nature of supramolecular polymers, they are suited for self-healing applications. Optical healing capabilities have been demonstrated by irradiation with a UV light source which heats the material up to 188 °C and cures macroscopic defects over a time period of 12 seconds.¹⁵² In the following section, the same principle is applied for data storage applications at the nanometer scale with a thermal scanning probe as the heat source and at time scales on the order of microseconds.

The requirements on a substrate for thermomechanical data storage are (i) homogeneity at the nanoscale, (ii) resistance against wear and (iii) easy deformability during writing.³⁶ Most polymers investigated for data storage applications (see Table 1.1) were crosslinked to improve their resistance against wear at the cost of an increase in the glass transition temperature. The advantage of supramolecular polymers is that the crosslinks can be

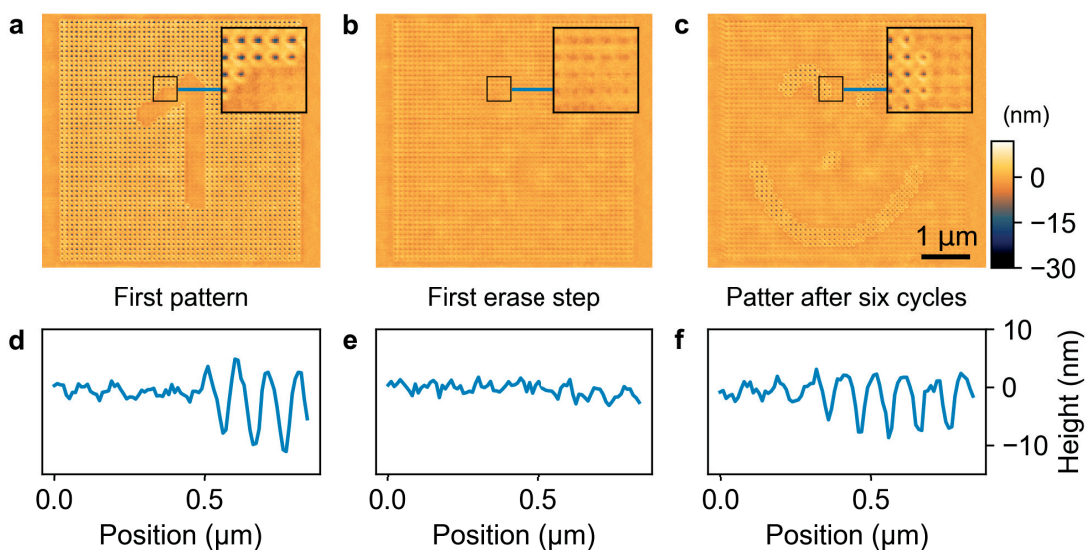


Figure 2.12 – Demonstration of write and erase cycles on a supramolecular polymer. (a) The surface topography of a pattern composed of indents, except for the area with the number "1" in the supramolecular polymer. The inset shows a zoom of the surface topography. (b) The same area after erasing every indent by using a lower electrostatic force and a contact time of 50 μs . (c) The same area after six cycles of patterning and subsequent erasing. (d)-(f) The measured surface profiles are plotted as indicated by a blue line in the corresponding topography. The topographical contrast between indents and erased indents is on the order of 10 nm.

broken up by thermal energy during indentation but form again after the heat source is removed. As a consequence, the material is resistant against wear during readout of the pattern. Here this concept is demonstrated by thermomechanical writing and erasing indents in UPy-OPV-UPy by a heated probe. Figure 2.12a shows a pattern of $5 \times 5 \mu\text{m}^2$ with indents separated by a distance of 100 nm. The contact time of the heated probe was 8 μs with a high electrostatic force (9 V applied voltage). The inset shows a magnified image of the surface topography to resolve the contrast between indented and non-indented areas.

In the next step, the indents were erased by applying a force just sufficient enough to bring the tip into contact with the substrate. Then heating was applied to bring the supramolecular polymer above the glass transition temperature and induce reflow. During erasing, the contact time was increased to 50 μs to allow sufficient time for the polymer to reflow. The set of parameters were experimentally determined by a trial-and-error approach. Note that this erasing scheme is slightly different than previously reported, in so far that it does not require the pitch size to be decreased as reported on PMMA samples.⁸ The inset shows that while the location of the former indent is still visible, the depth of the indent has significantly decreased from 10 to 2-3 nm. Before the pattern

displayed in Figure 2.12c, six pattern/erase cycles have been performed. Despite the history of intents can be determined by eye, the contrast between indented area and erased indents is sufficient to distinguish them. Figures d)-f) show the surface profile in each topography as indicated by the blue horizontal line. The topographical contrast between indents is clearly visible.

The pitch size of the pattern shown in Figure 2.12 is 100 nm, which translates into a storage density of 64 Gb/in². This value can be increased by reducing the indentation depth and arranging the indents in a triangular lattice instead of a quadratic. The storage density achieved here is two orders of magnitude smaller than the Tb/in² range demonstrated on PMMA during the “Millipede” project.^{8,50,163} It was demonstrated that the limit of thermomechanical data storage is reached at an indent density of 4 Tb/in² due to the finite size of the tip apex, substrate roughness and rim formation.³³ Compared to optical storage media, such as Blue-ray discs with a storage density of 12.5 Gb/in², thermomechanical indentation techniques can reach 2 orders of magnitude higher storage densities. However, new developments in the field of heat-assisted magnetic recording, suggest that storage densities larger than 10 Tb/in² can be achieved at writing velocities of 7.5 m/s.¹⁶⁴

While supramolecular polymers exhibit properties that could be interesting for data storage applications, it is unlikely, that they will find a commercial application in this field. Nevertheless, understanding self-healing at the nanometer scale is important to understand the mechanism behind it and design better materials. Local thermal analysis with a heated tip can be useful to analyze self-healing effects at the nanometer scale.

2.3.8 An Attempt to Pattern Supramolecular Polymer on a Paper Substrate

The fluorescent supramolecular polymer used in this work, has been shown in the previous chapters to be a candidate for creating anti-counterfeit security features with sub-diffraction limit resolution that can be read out by optical microscopy or surface metrology methods. Patterning of UPy-OPV-UPy in the previous chapters was performed on silicon chips due to the current restriction of the cantilevers to conducting substrates. However, in principle the technology is not limited to smooth and rigid substrates but can be applied on any type of material, as demonstrated in the following experiment. Figure 2.13a shows a piece of cellulose printer paper with dark lines of graphite from a pencil. The graphite is necessary to provide a conducting substrate for electrostatic cantilever actuation. The orange stripe perpendicular to the pencil lines, was fabricated from a piece of molten UPy-OPV-UPy by spreading it over the paper using a razor blade. A pin is placed on the graphite lines to establish an electrical contact and clamp the sample in the t-SPL tool. For thermal lithography, the cantilever was placed on the graphite stripes and patterning was performed as described in Section 2.2.3. Figure 2.13b shows

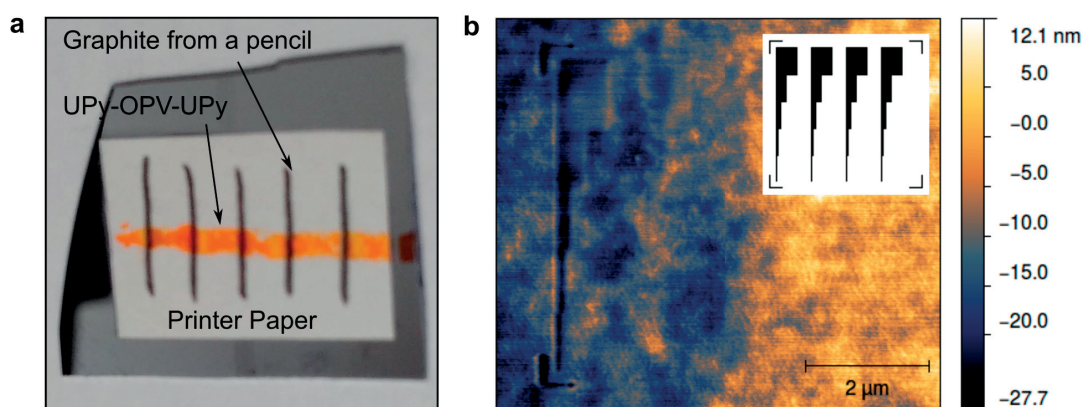


Figure 2.13 – t-SPL of a fluorescent supramolecular polymer on paper. **(a)** An optical photograph shows a printer paper sample with vertical graphite lines used to as electrodes for electrostatic actuation of the cantilever and the orange supramolecular polymer. **(b)** A surface topography obtained on the supramolecular polymer on paper with the inset showing the pattern template. Only a part of the pattern was transferred, presumably due to large variations in the surface height.

the surface topography of a pattern that was obtained based on the target pattern in the inset. The left part of the structure is nicely patterned into the supramolecular polymer but on the left side no pattern is created. It is speculated that the surface irregularities of the polymer are too large and hence the tip loses contact to the sample, because the tip height calibration of the tool was typically performed in the lower left corner. To try to increase the surface homogeneity, supramolecular polymer was hot pressed on the paper as described in Section 2.2.1. However due to poor adhesion between the polymer and the graphite layer no samples of satisfactory quality could be obtained. To avoid the necessity of an electrical layer on paper or any other flexible material, a new type of cantilevers are being developed with backside electronic contacts, which would allow patterning on non-conducting substrates.⁶²

Here it was demonstrated that thermal patterning of supramolecular polymers is not limited to smooth and rigid materials but can be performed on flexible and uneven substrates, though with limited results. Further improvements on the sample fabrication and introducing back-side actuated cantilevers can facilitate thermal patterning on rough and flexible substrates.

2.4 Conclusion

Nanoscale thermal patterning with a heated probe of a novel thermochromic luminescent supramolecular polymer was demonstrated. t-SPL nanoindentation of UPy-OPV-UPy films resulted in a fluorescent as well as topographical pattern at the nanometer scale due to a low viscosity above T_g and the ability to kinetically trap the disassembled

Chapter 2. t-SPL of a fluorescent supramolecular polymer

monomeric state with a resulting hypochromic shift. The results suggest that this is only possible for a small heated volume. In-depth studies of the patterning conditions showed that altering the nanoscale indentation pitch modulated the green fluorescence intensity, material pileup, and overall patterning parameters. It was further explored how patterns can be erased and rewritten using the self-healing feature of the supramolecular glass.

3 Silk Fibroin as a Resist for t-SPL

3.1 Introduction

Silk fibroin has attracted interest in the past years due to its remarkable mechanical strength,¹⁶⁵ high optical transparency (>95% in visible range)¹⁶⁶ and its tunable biodegradability.¹⁶⁷ Silk is a natural material produced by certain spiders (e.g. *Nephilia clavipes*) or worms such as the domestic silkworm *Bombyx mori*.¹⁶⁵ Silk from *Bombyx mori* is composed of fibroin which is surrounded by hydrophilic proteins sericin. For technical applications, the later is typically removed during a degumming process.¹⁶⁸ Fibroin consists of a light chain (~26 kDa) and a heavy chain (~390 kDa), both of which are composed of a repeated sequence of amino acids glycine, alanine and serine. The proteins can stabilize via inter-chain hydrogen bond interactions to form α -helix and β -sheet secondary structures as shown in Figures 3.1a and b, respectively. Silk fibroin prepared from aqueous solution and dried in air at ambient conditions on a substrate is composed of mainly α -helix/random coil confirmation, which is typically identified as the amorphous phase. A phase change from the water-soluble amorphous phase to a crystalline phase can be induced by treatment with organic solvents such as ethanol or methanol, which promotes the formation of beta-sheet crystallites (annealing). The crystallites act as a cross-linker between fibroin strands and turns the material water-insoluble.¹⁶⁹

In applications such as in optical bio-sensors^{165,170} and bio-electronics,^{171,172} structuring of silk fibroin is required to obtain the desired shape and functionality of the device.¹⁷³ Several techniques have previously been used to create micro- to nanometer sized patterns in silk fibroin, including soft-lithography based molding,¹⁷⁴ rapid thermal nanoimprinting^{175,176} and sub-micrometer sphere templating.¹⁷⁷ Silk fibroin has also been patterned by means of UV photolithography in combination with a photoinitiator, which crosslinked the fibroin chains when exposed to UV light¹⁷⁸⁻¹⁸⁰ and 3D structures have been fabricated by multiphoton lithography.¹⁸¹ More recently, silk fibroin samples were patterned through deep UV photolithography without photoinitiators by taking

advantage of the phototendering effect.¹⁸² To obtain sub-100 nm resolution, e-beam lithography has been performed directly on annealed and as-spin-coated silk fibroin films by using it as positive and negative resist.¹⁸³ To use it as a negative resist, the as-coated amorphous silk fibroin thin films are exposed by e-beam at high irradiation doses ($75000 \mu\text{C}/\text{cm}^2$ at 125 keV, 2 nA), inducing an amorphous-to-helix structural change by radiolysis with residual water in the film, which renders the exposed area water-insoluble. To avoid high electron doses that are necessary to induce beta-sheet formation via radiolysis, conjugation of fibroin with methacrylate moieties to induce crosslinking during exposure was recently proposed.¹⁷² For positive silk fibroin resist, the as-coated films were annealed in ethanol to promote the formation of water-insoluble beta-sheet crystallites and the subsequent electron irradiation ($7350 \mu\text{C}/\text{cm}^2$, 125 keV, 2 nA), degrades the exposed areas of the silk film, which results in the formation of water-soluble short polypeptides.¹⁸³

The contrast formation in nanoscale patterning of silk fibroin by e-beam and photolithography is based either on decomposition of the protein, such as by phototendering or electron irradiation, or the formation of crosslinks, for example by the addition of a photoinitiator or functionalization of the protein. The polymorphic nature of silk fibroin - it can be either a water-soluble phase composed of random coil and alpha-helix secondary structures or a water-insoluble phase rich in beta-sheet crystallites - could be used to create a solubility contrast without the necessity to use UV light or electrons. It is known that moderate temperatures between 192 to 214 °C induce beta-sheet formation in a previously amorphous silk fibroin film,¹⁶⁹ through thermally assisted reorientation of the molecular chains. More recently, it was discovered by fast scanning calorimetry that the reversed phase change, the melting of beta-sheet crystallites at 292-351 °C, can be induced by fast heating at rates on the order of 2000 °C/s while significantly suppressing decomposition of fibroin.^{184,185} During melting of the crystallites, the stabilizing hydrogen bonds of the secondary structures are broken up, which results in a crystalline to amorphous phase change accompanied by a change in the water solubility.

Similar to fast scanning calorimetry, a heated atomic force microscopy (AFM) tip can serve as a heat source with high enough heating rates to melt beta-sheet crystallites as depicted in Figure 3.1c. The thermal probe is brought into contact with the substrate by applying an opposing electrical potential between cantilever and sample, which pulls the cantilever towards the substrate as illustrated in Figure 3.1c. When the thermal probe is in contact with the substrate, the material around the probe is locally heated at heating rates reaching 10^8 K/s as depicted in Figure 3.1d. Thermal scanning probe patterns are formed by consecutive indentation with the heated probe for a few microseconds per indent while raster scanning the sample below the thermal probe.¹⁸⁶

In this chapter, thermal patterning of annealed silk fibroin thin films by using a nanometer scale heated probe, which changes locally the water solubility of the exposed material is demonstrated. Subsequent immersion in deionized water removes the thermally-altered

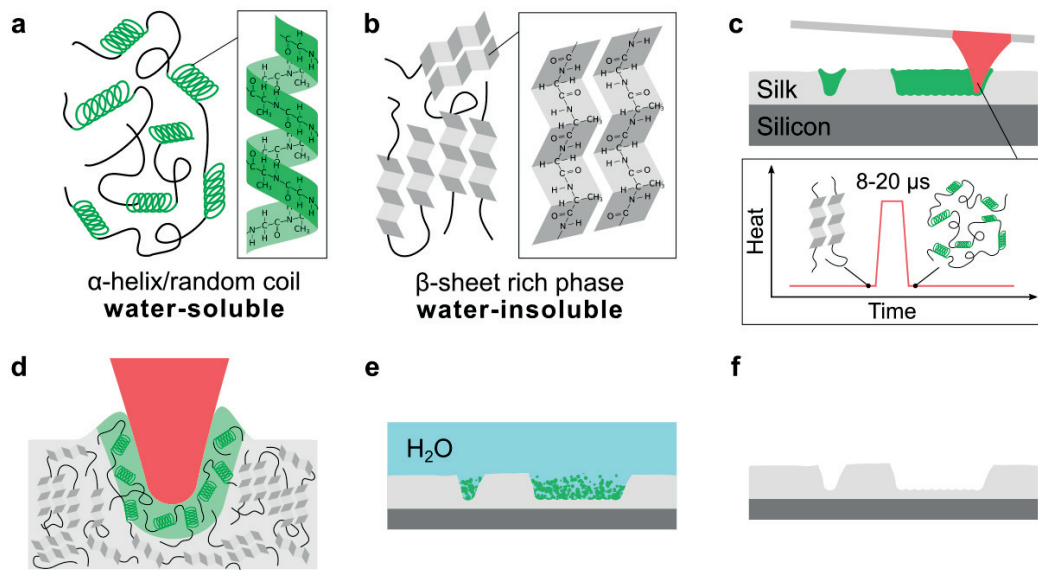


Figure 3.1 – Concept of t-SPL on silk fibroin thin films. (a) A visualization of the water-soluble amorphous silk phase in which the fibroin is arranged in α -helix secondary structure and random coils. (b) Water-insoluble crystalline phase composed of β -sheet secondary structures, which act as cross-links between fibroin strands. (c) Thermal patterning of silk fibroin with a heated probe by applying heat pulses on the order of microseconds to induce melting of beta-sheet crystallites. (d) Local phase change from water-insoluble to water-soluble phase in close proximity of the tip. (e) Development of the exposed area in DI water. (f) Micro- to nano-sized topographical structures in silk fibroin are obtained after pressurized air drying.

material.

3.2 Materials and Methods

3.2.1 Sample Fabrication

A 9 wt% aqueous solution of silk fibroin was prepared using a standard procedure.¹⁸⁷ In brief, *Bombyx mori* silk cocoons were reduced to small pieces using scissors and boiled in a 0.02 M Na_2CO_3 solution for 30 min to remove sericin from the natural silk fibers. The remaining fibroin fibers were rinsed with deionized water and dried overnight. The dry fibroin was completely dissolved after 4 hours in a 9.3 M LiBr solution at 60 °C. After dialysis against deionized water over three days, followed by two centrifugation steps at 4400 RPM for 20 min and filtration (Millex SV 5.00 μm PVDF syringe filters, SigmaAldrich), a clear solution of silk fibroin was obtained. The solution was cooled in a fridge between the centrifugation steps to avoid gelling. 280-350 nm thick films were obtained by spin coating the solution on oxygen plasma (100 W, 0.4 mbar, 1 min) treated silicon chips at a speed of 4000 RPM for 2 minutes with an

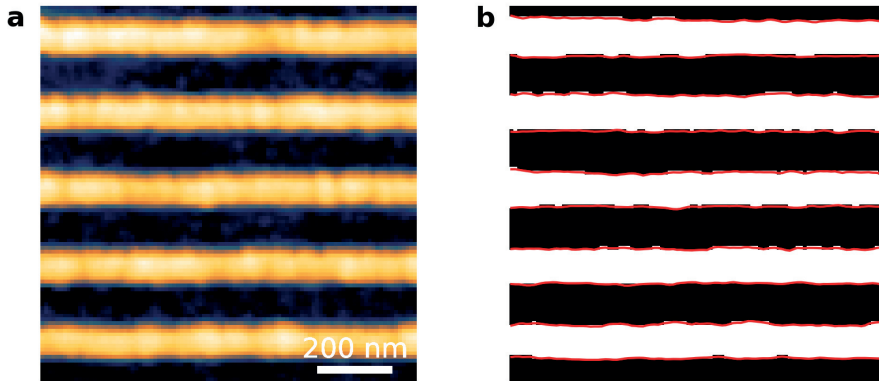


Figure 3.2 – Determination of the line edge roughness. **(a)** The surface topography of a pattern with horizontal lines is shown, which is used to determine the line edge roughness, **(b)** The binarized image with the detected edges in *red* which were used to compute the LER.

acceleration of 1000 RPM/s. The spin-coated films were soft-baked on a hot plate at 90 °C for 1 minute to evaporate water residues. To promote the formation of water-insoluble beta-pleated sheet crystallites, the samples were immersed in ethanol (70 vol%, Reactolab SA) for 4 minutes, which was found to be sufficient to turn the films water-insoluble.¹⁸⁷ Alternatively, in view of a fully water-based lithography process, the silk fibroin films can be annealed in water vapor for 12 hours.¹⁸³

3.2.2 Thermal Scanning Probe Lithography

Patterning of the silk fibroin films was performed using a commercial thermal scanning probe lithography tool (NanoFrazor Explore, Swisslitho AG) at a heater temperature of ~650-960 °C equipped with a thermal scanning probe (Monopede HPL, Swisslitho AG). A heating efficiency $c=0.50$ was used to estimate the contact temperature T_c between the tip and the substrate based on the common relationship $T_c = c \cdot (T_h - T_s) + T_s$, where T_h is the heater temperature and T_s is the substrate temperature.³⁶ The distance between indents (pixel size) was 20 nm for high-resolution patterns and 40 nm for large area patterns and the tip was actuated towards the substrate for 8-30 μ s. After thermal patterning, the samples were immersed in deionized water for 20 s to dissolve the thermally modified silk fibroin (Figure 3.1e) and dried with a nitrogen gas gun (Figure 3.1f). Shorter or longer development were not found to enhance the pattern quality. To observe the resulting patterns after development, the samples were scanned with the same t-SPL tool in imaging mode, similar to an atomic force microscope (AFM).

3.2.3 Calculation of the Line Edge Roughness

A script was used to compute the line edge roughness (LER) from a silk fibroin surface topography as shown in Figure 3.2a (see Appendix A.3).¹⁸⁸ The first part of the script converts the surface topography into a binary image by *Otsu's Binarization* method as shown in Figure 3.2b. An edge detection algorithm was used to obtain the coordinates of the edge as indicated by the *red* curves. The edge coordinates are fitted to a line and the line edge roughness is computed using $\sigma = \sqrt{\frac{\sum_i^N \delta_i^2}{N}}$, where δ_i is the distance between the edge and the fitted line for the *i*-th data point and *N* is the number of data points. The LER (3σ) is averaged over 10 lines.

3.2.4 Dry-Etching of Silk Fibroin

To test the effectiveness of silk fibroin thin films as a mask layer, experiments were made on pattern transfer to SiO₂ thin films. Silk fibroin was spin coated on silicon chips with a 200 nm thick wet silicon oxide and patterned as described in Section 3.2.1, followed by t-SPL patterning of ~200 nm deep squares. The chips were then attached to a 4-inch silicon wafer for compatibility with the dry etcher. The pattern transfer to SiO₂ was completed with an inductively-coupled plasma dry-etcher (SPTS APS, SPTS Technologies Ltd). The samples were dry etched in He/H₂/C₄F₈ (175/18/15 sccm) for 55 seconds at a pressure of 4 mTorr, an inductively coupled plasma (ICP) power of 1200 W and an RF power of 300 W. After dry etching, the silk fibroin resist was removed by oxygen plasma cleaning for 10 minutes at a power of 100 W and a pressure of 0.4 mbar (Femto, Diener electronic GmbH).

3.3 Results and Discussion

In the following sections, the contrast formation mechanism of silk fibroin as a t-SPL resist is discussed and results about the achieved resolution and line edge roughness are presented. A simulation of the temperature distribution around a tip apex in silk fibroin is shown. Finally, grayscale lithography of silk fibroin by t-SPL is demonstrated and preliminary results of a pattern transfer from silk fibroin into SiO₂ are presented.

3.3.1 Contrast Formation Mechanism in Thermally Modified Silk Fibroin

The contrast formation mechanism of silk fibroin as a water-developable resist for thermal scanning probe lithography is investigated by writing square patterns with an area of $5 \times 5 \mu\text{m}^2$ with the t-SPL tool ($T_{\text{contact}}=362 \text{ }^\circ\text{C}$, $t_{\text{contact}}=30 \mu\text{s}$) as shown in Figure 3.3a. After t-SPL, the thermally modified area can be distinguished from the unpatterned border (Figure 3.3a *left*), namely through a small pile-up of material that has formed at

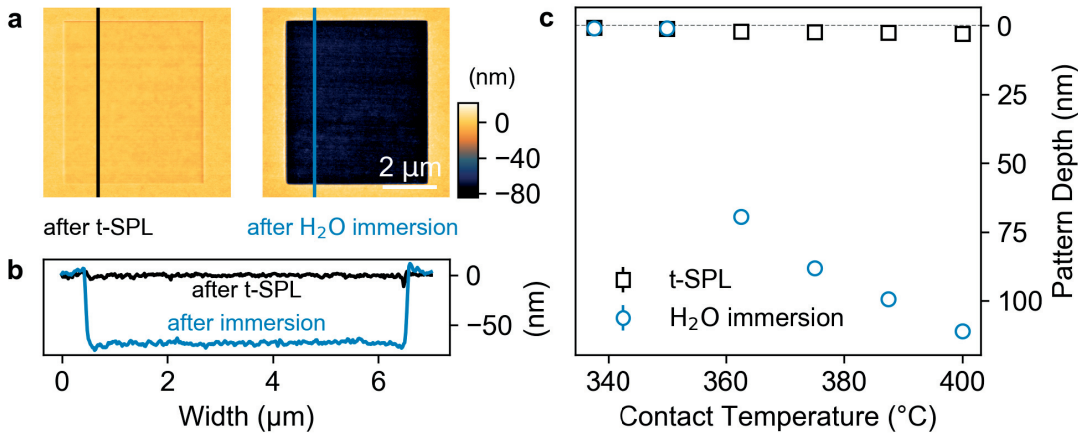


Figure 3.3 – Contrast formation in t-SPL on silk fibroin. (a) AFM surface topography of a silk fibroin film after t-SPL patterning at $T_{Contact} = 363$ °C (*left*) and after water immersion for 20 seconds (*right*) are shown. (b) The corresponding surface profiles as indicated on the topographies is shown. (c) Pattern depth as a function of the temperature before and after immersion in water.

the corners of the square due to plastic deformation of molten fibroin during indentation. The pile-up is only visible at the edges of the square because during each consecutive indent, the previous indent is filled with molten material, which is pushed to the side by the tip as already discussed in Chapter 2.^{146,189} After immersing the sample for 20 seconds in DI water at room temperature, the thermally modified fibroin dissolved as demonstrated in Figure 3.3a (*right*). The surface profiles in Figure 3.3b show that the material has been uniformly removed down to a depth of 65 nm, while the surface roughness of the patterned area only slightly increased from 1.5 nm to 2 nm. To determine the contact temperature at which indents start to form, square patterns are written at different tip temperatures and the pattern depth was measured after immersion in water as shown in Figure 3.3c. For a contact temperature of 338 °C and below, no pattern is visible because the thermal energy provided by the tip is not sufficient to melt the silk fibroin above the glass transition temperature (between 167 and 201 °C¹⁸⁴) and penetrate the film.

At a contact temperature of 350 °C, the thermal conversion of the silk fibroin takes place, but non-uniformly. Tests on multiple samples did not uncover the source of this nonuniformity. At contact temperatures above 350 °C, patterning is stable and the pattern depth increases up to ~110 nm at 400 °C after water immersion. Although the indentation force was kept constant, the pattern depth increases with temperature. A possible explanation is that due to the higher tip temperature, a wider range of material is thermally converted or that, due to the temperature dependent bending of the cantilever, the tip exerts a larger force on the molten material.

In order to understand the origin in the solubility change of annealed silk fibroin when

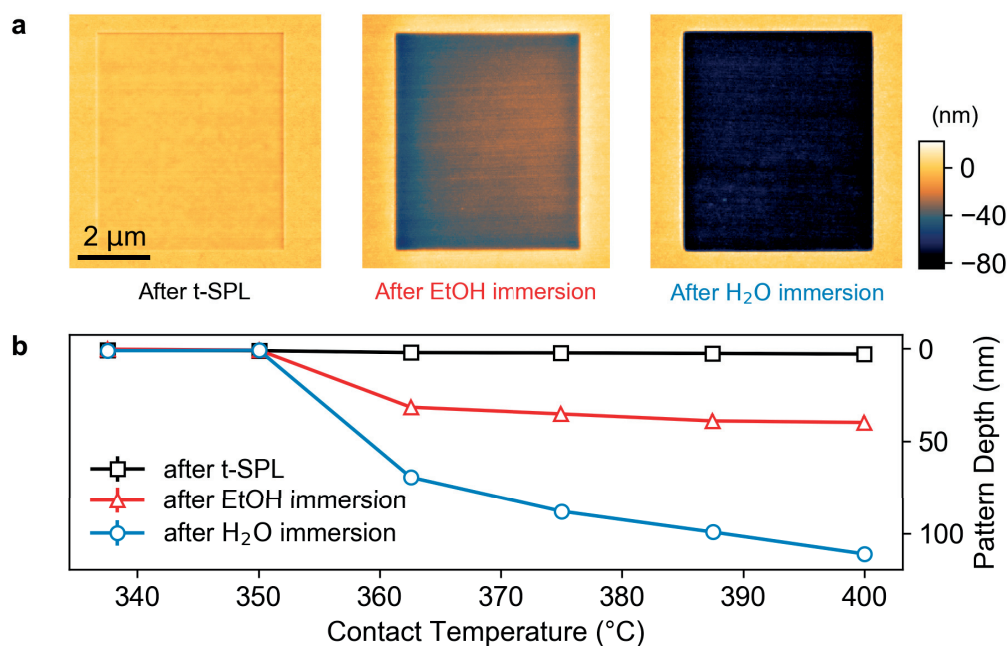


Figure 3.4 – Reversibility of t-SPL treated silk fibroin. (a) Surface topography of a silk fibroin film after thermal patterning, after immersion in ethanol and after immersion in water. (b) The pattern depth is plotted as a function of the contact temperature after t-SPL, ethanol immersion for 10 min and after water immersion for 20 seconds.

heated with a thermal probe at high heating rates on the order of 10^8 K/s for a few microseconds, the volume change of the material during thermal treatment and the reversibility of the solubility change are analyzed. Ideally, the information about the composition and degree of crystallinity of silk can be obtained by infrared spectroscopy or x-ray diffraction. However, since typical patterns are only few tens of micrometers in length and the thermally exposed volumes are on the order of a few femtoliters, direct measurement using spectroscopy techniques is challenging. Instead, for this work, indirect measurements that can give information about the conversion process are used.

Based on the work by Cebe *et al.* on fast differential scanning calorimetry of silk fibroin, it is hypothesized that if melting of beta sheet crystallites is reversible, the solubility change originates from melting of beta-sheet crystallites.¹⁸⁴ Hence, $5 \times 5 \mu\text{m}$ large squares are patterned at different contact temperatures and immersed in ethanol prior to the development in water to induce beta-sheet formation. Figure 3.4a shows the surface topographies after t-SPL, after immersion in 70% ethanol for 10 minutes and after water immersion for 20 seconds. During immersion in ethanol, some of the thermally treated silk fibroin dissolves slowly but does not turn water-insoluble, as shown in the topography after water immersion.

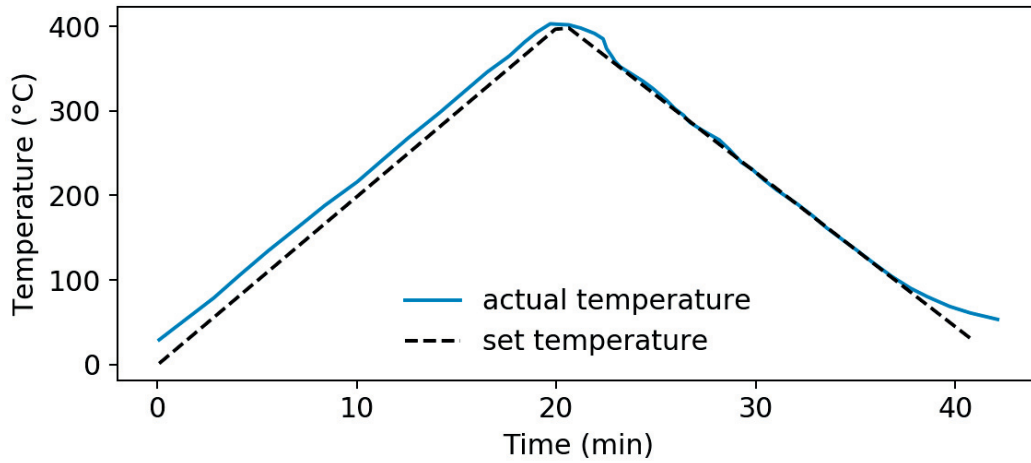


Figure 3.5 – Temperature profile during thermal treatment of a silk fibroin thin film with a conventional high-temperature oven at a heating rate of 20 °C.

Further, the effect of temperature on the reversibility of the phase change is analyzed. Figure 3.4b shows the pattern depth after t-SPL, after ethanol immersion and after water immersion for contact temperatures ranging from 340 to 400 °C. At 338 °C, neither a visible pattern is created nor does material dissolve in ethanol or water. At 350 °C, the patterned square is visible after t-SPL but little material is dissolved in ethanol. At higher temperatures, the thermally modified silk fibroin partially dissolved in ethanol during the 10 minutes immersion. After drying with a nitrogen gun, traces originating from the patterned area are observed. During the subsequent immersion in water for 20 seconds, the traces as well as the remaining material in the structures are removed, giving an indication that no conversion to water-insoluble β -sheet-rich silk fibroin takes place as described by Cebe *et al.*¹⁸⁴

An explanation for this can be that the silk fibroin thermally degraded during indentation with the heated probe. To investigate if the silk fibroin pyrolyzed during thermal indentation experiments, a sample coated with a silk fibroin film that was previously used for t-SPL was heated to 400 °C in a high-temperature oven (EO 601, ATV Technologie GmbH) at a rate of 20 °C/min as shown in the temperature curve in Figure 3.5. The pyrolyzed film was immersed in ethanol and water but no dissolution was observed as for the t-SPL patterns. It can be concluded that silk fibroin during thermal indentation neither fully converts back into the phase before annealing (amorphous random coil/ α -helix), nor does it pyrolyze during thermal indentation.

Besides the solubility of thermally treated silk fibroin in ethanol and water, the volume change induced by the heated tip can give information about the contrast mechanism. Four possible modifications are going to be discussed in view of the induced volume changes: (i) mechanical material removal, (ii) thermally induced phase change of silk fibroin,

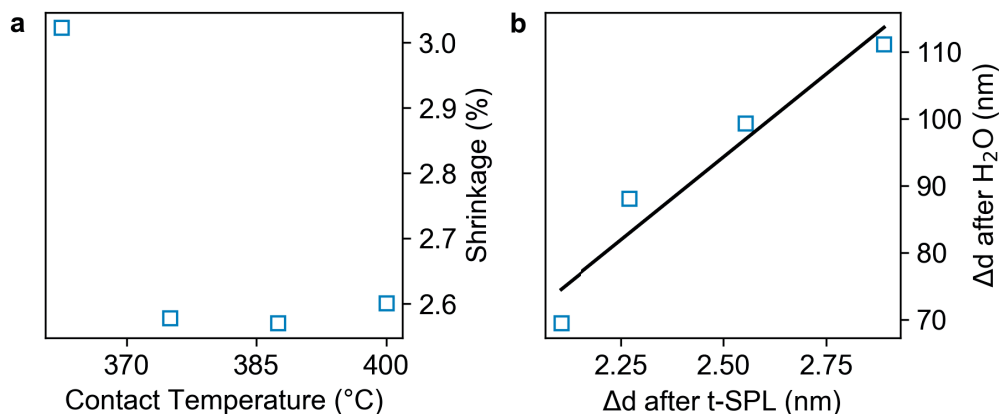


Figure 3.6 – Correlation between temperature, shrinkage and depth. (a) The volume shrinkage of thermally treated silk fibroin is shown as a function of temperature. (b) Correlation between pattern depth after t-SPL and after water immersion.

(iii) thermal decomposition and evaporation of volatile molecules and (iv) evaporation of bound water in silk fibroin.

Mechanical removal of material is very unlikely to be the cause of the observed volume change, because during the experiments, no material was found at the border of the scanned area. It is also unlikely that material deposits on the tip during patterning due to contamination from silk residues. A quick calculation reveals that a volume equal to the observed difference before and after t-SPL, would result in a 180-280 nm thick layer on the tip. The adhesion length of the tip during approach and retraction is regularly observed and found not to have significantly changed during interactions with the silk fibroin.

A phase change from crystalline ($\rho_{\text{crystalline}} = 1.4 - 1.45 \text{ g/cm}^3$) to amorphous silk fibroin ($\rho_{\text{amorph}} = 1.3 \text{ g/cm}^3$) would result in a volume increase of 11%.¹⁹⁰ Since for the thermally treated films, a decrease in the volume is observed, a phase change cannot explain the experimental observation. It should be noted that this does not necessarily mean that no phase change occurs at all during the thermal transformation of silk fibroin with the heated tip.

Figure 3.6a shows the shrinkage of the patterned volume as a function of the tip temperature. Values where no pattern was created at lower temperature are excluded. Based on the availability of experimental data, it is not possible to see a clear trend in the data. However, one can observe a shrinkage of the patterned material between 2.6 and 3%. In Figure 3.6b, the depth change after t-SPL patterning is plotted against the depth change after water immersion. The graph shows that the shrinkage after t-SPL correlates with the overall thermally modified volume. Yazawa *et al.* studied the water

	Observation			
	t-SPL treated silk is water soluble	t-SPL melting is irreversible	Pyrolyzed films are insoluble	Volume change during t-SPL
Explanation	β -sheet to α -helix/random coil conversion	✓	✗	only if water evaporation is dominant
	Thermal degradation	✗	✓	✓
	Water evaporation during t-SPL		?	✓

Figure 3.7 – Diagram with possible explanations for the contrast mechanism in t-SPL treated silk fibroin vs. experimental observations.

removal and thermal decomposition of silk fibroin films by means of differential scanning calorimetry and thermogravimetric analysis and found evaporation of bound water (5-9 wt%) occurs between 80 and 200 °C depending on the ambient humidity,¹⁹¹ which can explain the shrinkage of 2.6-3% observed by after t-SPL patterning.

Cebe *et al.* studied the thermal degradation of silk using fast scanning calorimetry at low (0.03 °C/s) and high (2000 °C/s) heating rates. They found that the onset of thermal degradation starts at 220 and at 347 °C for slow and fast heating, respectively. Following the time-temperature-superposition behavior of many polymers, it would be expected that the thermal degradation of silk at heating rates of 10^8 °C/s occurs at temperatures much higher than 347 °C (see Section 2.3.1). However, due to the uncertainty in the calculation of the contact temperature it can not be fully excluded that partial thermal degradation of the silk fibroin occurs during thermal indentation.

In summary, the contrast mechanism of thermally treated silk fibroin could not be precisely identified. Figure 3.7 shows an overview of the above discussed experimental observations and possible explanations. The experiments suggest that neither does a pure crystalline to amorphous phase change occur, nor does the silk fibroin completely degrade during thermal indentation. Evaporation of bound water could explain the shrinkage of the annealed silk after patterning.

3.3.2 Resolution

In order to determine the lateral resolution of silk as a t-SPL resist, a series of horizontal lines at a pitch size from 100 to 400 nm and a target depth of 100 nm were patterned as shown in Figure 3.8a. One can see that the patterns were successfully written down to a pitch-size of 200 nm, however at a pitch of 100 nm the side walls separating the thermal

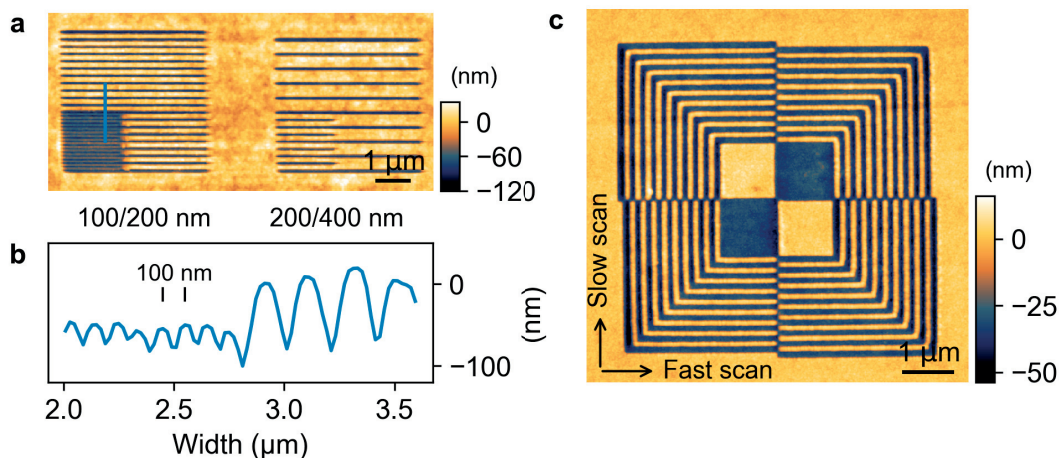


Figure 3.8 – Resolution and line edge roughness of t-SPL with silk fibroin. (a) Surface topography of a pattern composed of horizontal lines at a pitch of 100, 200 and 400 nm for demonstrating high resolution patterning capability. The blue line corresponds to the surface profile shown in the figure below. (b) The surface profile of the 100/200 nm pattern is plotted against the position, whereby 30 nm tall structures were obtained at a pitch of 100 nm. (c) Pattern with horizontal and vertical structures to determine the line edge roughness in fast and slow scan direction.

indents have been removed during immersion in water. The surface profile across the 100/200 nm pattern is plotted in Figure 3.8b and shows that for the smaller pitch size, the features are 30 nm deep. Geometrically, with a tip opening angle of 30° and a pitch size of 100 nm, a depth of approximately 187 nm is expected. However, spreading of heat from the tip and a finite tip apex radius can considerably reduce the height of the pattern (see Appendix A.1).

Line edge roughness (LER) is another measure of resolution commonly used in lithography, which describes the deviation of a patterned line from an ideal straight line. In Figure 3.8c, a pattern with parallel features in vertical and horizontal directions is shown, which is used to compute the LER in the slow and fast scan directions. For the 30-40 nm deep pattern, a LER of 6.9 ± 1.8 nm (horizontal) and 9.3 ± 2.4 nm (vertical) is obtained in fast and slow scan directions, respectively. The increased roughness in the slow scan direction is likely due to the pileup of material from the indentation at the end of each sequence of consecutive indents. It can also be observed in Figure 3.8c, that the depth of vertical lines is on average 10 nm larger than for horizontal lines. The LER and the ultimate resolution in lithography are directly related to the molecular size of a resist.

The size of silk fibroin fibrils adsorbed on a silicon substrate has been determined previously by AFM imaging to be on the order of 180 nm^3 which results in a diameter of approximately 7 nm for a globular structure.¹⁹² The line edge roughness obtained from the measurements is in agreement with the size of the fibroin molecules.

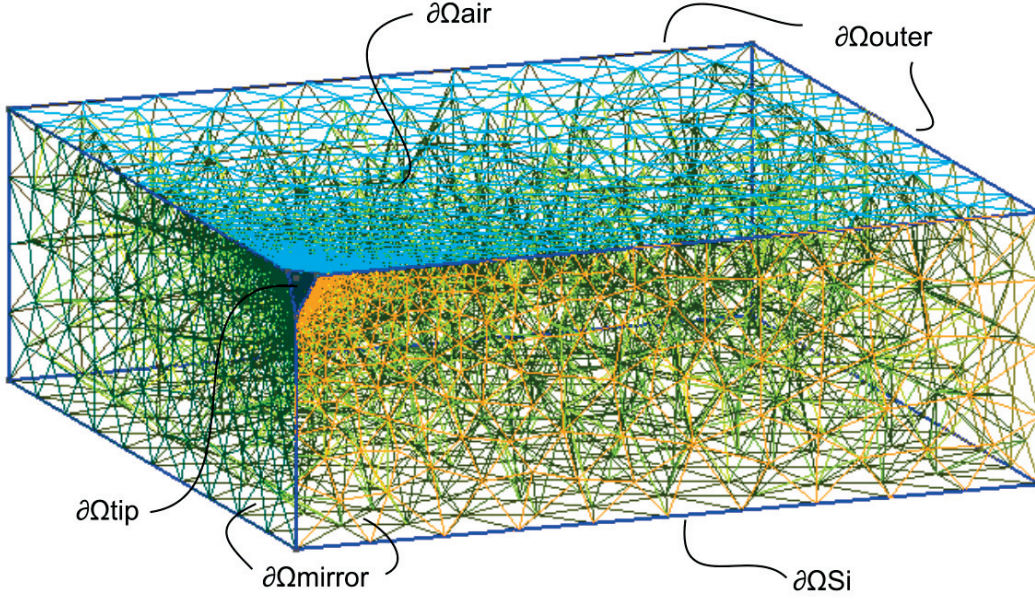


Figure 3.9 – Finite element mesh and domain Ω for simulating the heat transfer from a tip to the substrate

3.3.3 Temperature Distribution Around the Tip Apex

In order to visualize the temperature distribution around the tip apex during indentation in the polymer, a finite element simulation is performed. Due to the complexity of the system under investigation, a few simplifications need to be made. The heat transfer from the heater to the tip apex, convective heat losses and the unknown contact resistance across the tip-polymer interface are neglected and a constant, uniform temperature of the tip is taken. A typical heater temperature during patterning is 650-750 °C, and assuming a heating efficiency of 0.4-0.7,¹⁹³ the temperature at the tip-polymer contact is between 290 to 510 °C. For the simulation, a tip temperature of 363 °C is chosen, because the lowest experimental heater temperature at which patterns are created is 700 °C (see Section 3.3.1) and a heating efficiency of 0.5 is assumed. For the simulation, it is assumed that the silicon substrate is at room temperature because silicon is a good thermal conductor ($\kappa_{Si} = 148 \text{ W/mK}$) and efficiently transfers heat away. To limit the computational effort the symmetry of the problem is exploited and only one quarter is simulated as shown in Figure 3.9. For simplicity, it is further assumed that no heat transfer takes place across the polymer-air interface. A temperature-independent, experimentally-determined thermal diffusivity of $\alpha_{silk} = 1.6 \cdot 10^{-7} \text{ m}^2/\text{s}$ from literature is used.¹⁹⁴

Under the assumptions specified above, the problem can be formulated as follows:

$$\frac{\partial u(\vec{x}, t)}{\partial t} = \alpha \nabla^2 u(\vec{x}, t), \quad \vec{x} \text{ in } \Omega \quad (3.1)$$

$$u(\vec{x}, t) = T_R, \quad \vec{x} \text{ on } \partial\Omega_{Si}, \partial\Omega_{Outer} \quad (3.2)$$

$$u(\vec{x}, t) = T_H, \quad \vec{x} \text{ on } \partial\Omega_{Heater} \quad (3.3)$$

$$\frac{\partial u(\vec{x}, t)}{\partial \vec{n}} = 0, \quad \vec{x} \text{ on } \partial\Omega_{Air} \quad (3.4)$$

$$u(\vec{x}, t) = T_R, \quad t = 0 \quad (3.5)$$

where $u(\vec{x}, t)$ is the temperature, \vec{x} the location vector, \vec{n} the surface normal vector, t is time and T_R is room temperature and T_H the heater temperature. The boundaries of the simulation are defined in Figure 3.9.

The heat equation is discretized in time to perform the time stepping with the forward Euler method:

$$\frac{\partial u(\vec{x}, t)}{t} \approx \frac{u(\vec{x}, t + \Delta t) - u(\vec{x}, t)}{\Delta t} = \frac{u_{n+1} - u_n}{\Delta t},$$

which leads to:

$$u_{n+1} - \alpha \Delta t \nabla^2 u_{n+1} = u_n$$

for the discrete form of the equation. To solve the differential equation in space, the finite element method is used. The weak form of the problem can be formulated as:

$$\int_{\Omega} v u_{n+1} d\vec{x} + \alpha \Delta t \int_{\Omega} \nabla v \nabla u_{n+1} d\vec{x} = \int_{\Omega} v u_n d\vec{x} \quad t > 0$$

$$\int_{\Omega} v u_{n+1} d\vec{x} + \alpha \Delta t \int_{\Omega} \nabla v \nabla u_{n+1} d\vec{x} = \int_{\Omega} v T_R d\vec{x} \quad t = 0$$

with the test function v .¹⁹⁵

Since no heat flows perpendicular to the symmetry planes, the boundary conditions $\frac{\partial u(\vec{x}, t)}{\partial \vec{n}} = 0$ are applied.

The mesh for the simulation is created with an 3-D finite element grid generator *gmsh*.¹⁹⁶

The indent depth is 50 nm, a value typically achieved during the experiments, and an opening angle of 30° was assumed for the conical tip. The finite element simulation was performed with the software *FEniCS*¹⁹⁷ (source code see Appendix A.4). The total time simulated was 6 μ s and 500 time steps were performed. Figure 3.10a shows an extract of the temperature distribution from the simulation around the 363 °C hot tip after 4 μ s of heating. The contours in the graph indicate lines of equal temperature. The temperature is highest at the contact with the thermal probe, and drops as a function of distance. About 20-30 nm away from the tip, the temperature has dropped below $T_g=167-201$ °C, the glass transition temperature of silk fibroin. The melting temperature of silk beta-crystallites ($T_m=292-351$ °C), is only reached at a distance less than 5 nm away from the thermal probe. Figure 3.10b shows the temperature profile from the tip apex in vertical direction towards the substrate after 16 ns, 0.5 μ s and 4 μ s. While heat quickly spreads during the first 0.5 μ s, no significant temperature increase can be observed afterwards.

Since no analytical expression of the temperature distribution of a cone in a slab was found to compare with the numerical simulations, the radial steady-state temperature distribution of a hemi-sphere is used.¹⁹⁸ The radial temperature distribution $T(r)$ of a hemi-sphere with a radius r_1 at temperature T_1 in contact with a material can be expressed by:

$$\frac{T - T_2}{T_1 - T_2} = \frac{1 - r_2/r}{1 - r_2/r_1}. \quad (3.6)$$

If the temperature T_2 at a distance of $r_2 - r_1$ away from the hemi-sphere is known the temperature distribution can be determined. For the analytical solution, the same boundary conditions as in the numerical simulation are used. The radius r_1 of the hemi-sphere was chosen such that it has the same surface area as the cone in the numerical simulation. The analytical solution is plotted in Figure 3.10b (dashed line). In close proximity to the tip, the temperature distributions differ due to the influence of the cone shape but the two distributions overlap with increasing distance.

From these findings one can conclude that the temperature is highest in close proximity to the tip apex and drops rapidly with increasing distance. The melting temperature of beta-pleated crystallites is reached only within ~5 nm from the tip, in contrast to the glass transition temperature which is reached between 20-30 nm away from the tip. Despite the simplicity of the model, it provides an estimation of the temperature distribution around the cantilever probe, and provides insight into the patterning mechanism of silk fibroin.

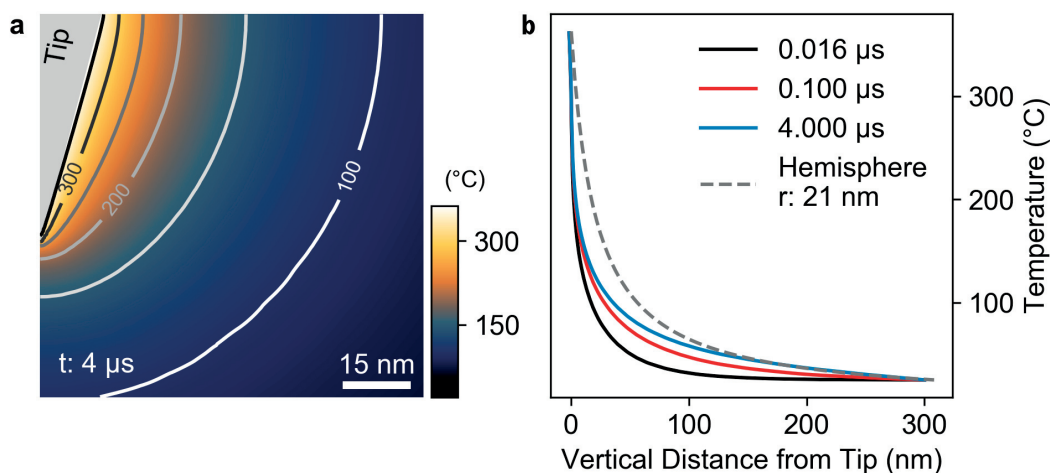


Figure 3.10 – Simulation of the temperature distribution around the tip inside the silk fibroin film. **(a)** Map of the temperature distribution near a heated probe at 363 °C indenting a silk fibroin thin film after 4 μs of heating. **(b)** The temperature of the silk fibroin film is plotted as a function of the vertical distance from the tip apex after different indentation times. The analytical solution of the steady-state radial temperature distribution for a hemisphere with a radius of 21 nm is plotted in dashed lines.

3.3.4 Grayscale Lithography

A major advantage of t-SPL is the simplicity to perform grayscale lithography by varying the deflection of the cantilever. While grayscale lithography has been successfully demonstrated for resists that volatilize upon thermal interaction with the probe,^{20,22} it is not evident that it would be possible for non-volatile resists. In this work, grayscale lithography with silk fibroin is demonstrated and discussed. Figure 3.11a shows a topography with a linear depth gradient from 30 to 200 nm over a range of 18 μm , which is created by decreasing the indentation force from left for right (Heater temperature 900 °C). Since silk does not decompose into volatile entities such as other t-SPL resists, it is supposed that the indentation mechanism is based on melting the silk fibroin when heated above the glass transition temperature ($T_g = 167\text{-}201$ °C), while the tip penetrates the molten material until the indentation force is in balance with the spring force of the cantilever and the shear force from the melt.

During patterning it was noted that besides the pile-up that forms from molten silk fibroin, which is displaced by the tip during indentation and dissolves after water immersion, some patterns exhibit a permanent rim around the edges (Figure 3.11a/b). To clarify the origin of this rim, its height is plotted as a function of the tip indentation depth as shown in Figure 3.11c. The maximum height of the rim of ~ 20 nm is observed at the left side, where the pattern is the deepest (*blue* curve) and gradually decreases with

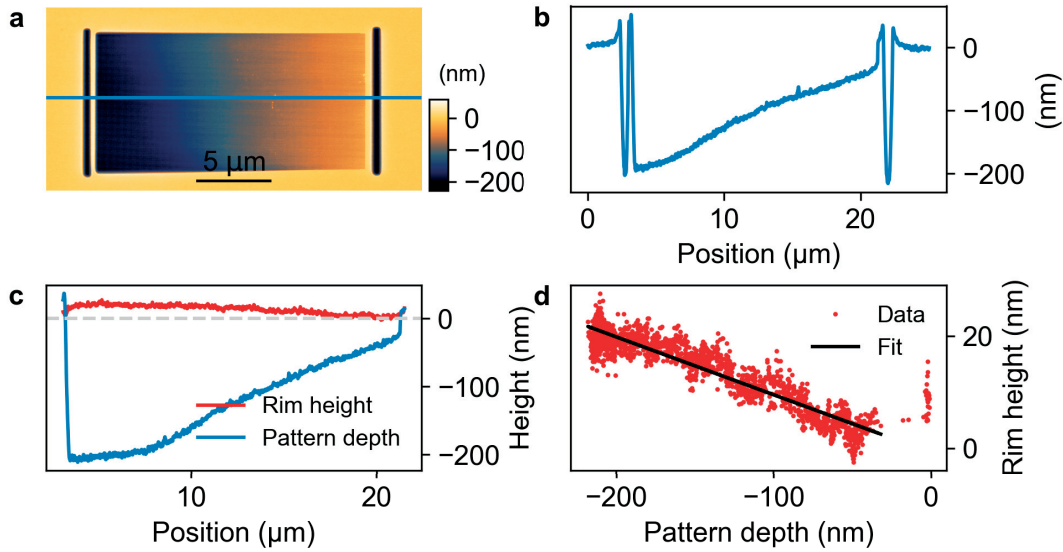


Figure 3.11 – Grayscale lithography of silk fibroin and correlation of the rim height with pattern depth. (a) Grayscale pattern in a silk fibroin film with a topographical gradient from 30 to 200 nm in depth. (b) Profile of the pattern as indicated by the blue line in the surface topography. (c) Profile of the pattern depth (*blue* line) and the rim height in horizontal direction at the lower edge of the structure (*red* line). (d) Plot of the rim height vs pattern depth shows a clear correlation between rim height and pattern depth.

decreasing pattern depth from left to right. Figure 3.11d shows a plot of the rim height as a function of the pattern depth, which reveals an almost linear relationship between the two parameters ($R^2=0.88$). It can be concluded that the permanent rim after patterning of structures deeper than 70-90 nm is due to plastic deformation of the silk fibroin with the conical probe. The deeper the probe indents, the more the silk fibroin is laterally deformed, which can explain the observations that deep structures were larger in lateral direction than the target pattern.

In this section it was shown that grayscale lithography does work also for non-volatile t-SPL resists such as silk fibroin, but structures deeper than 70-90 nm suffer from lateral deformation due to the conical shape of the probe.

3.3.5 Dry Etching of Silk Fibroin in He/H₂/C₄F₈ Chemistry

To extend the range of applications of silk fibroin as a resist for micro- to nano-fabrication, a dry-etch pattern transfer from silk fibroin into SiO₂ is demonstrated. In a first step, the etch rate of silk fibroin in He/H₂/C₄F₈ chemistry (175/18/15 sccm, 4 mTorr) was determined in order to calculate the etch selectivity of silk with respect to SiO₂. In Figure 3.12, the thickness change of 13 silk fibroin samples with respect to the initial

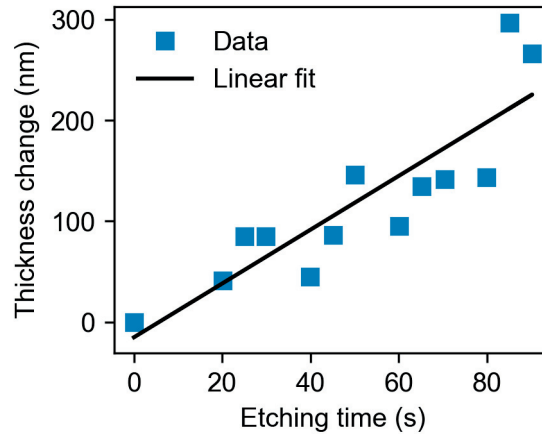


Figure 3.12 – The graph shows the thickness change of the etched silk fibroin film by dry etching using $\text{He}/\text{H}_2/\text{C}_4\text{F}_8$ for different etch times. The line displays the linear regression of the data points to determine the etch rate of silk fibroin (160 ± 28 , $R^2=0.75$).

thickness after etching is plotted against the etching times between 20 to 90 seconds. An etch rate of 160 ± 28 nm/min was computed from a least square fit to the measured data and an etch selectivity between silk fibroin and SiO_2 of 2.16 ± 0.08 was determined based on information about the SiO_2 etch rate for this dry-etch chemistry (345 nm/min).¹⁹⁹

After having determined the etch rate of silk fibroin, a pattern transfer is performed from ~ 200 nm deep structures in silk fibroin into a 200 nm thick layer of wet oxide on silicon. Figure 3.13a shows the surface topography of the patterns written into silk fibroin. The surface topography of the remaining resist is mapped again after dry etching for 55 seconds as shown in Figure 3.13b. Due to etching, the root mean square (RMS) surface roughness of the fibroin film increases from 2 to 28 nm. The remaining silk fibroin layer was removed by oxygen plasma cleaning for 10 minutes (100 W, 0.4 mbar) and the transferred structure in SiO_2 is shown in Figure 3.13c. The RMS surface roughness of the SiO_2 was 10 nm and as can be seen in the surface topography image, imaging was not optimal. It is speculated that either residues from the oxygen plasma treatment are on the surface or that the SiO_2 was etched by the oxygen plasma. Due to the depth of the structures, it was not possible to fully measure them with the AFM probe.

In comparison to $\text{He}/\text{H}_2/\text{C}_4\text{F}_8$ dry-etching processes with other thermal resists such as PPA, silk fibroin performs equally well. As an example an etch rate of 200 nm/min was obtained using the same dry-etch process on the same machine for untreated PPA. By optimization of the etch gas composition and a pre-bake to remove liquid in the resist, the etch rate for PPA could be improved to 59 nm/min.⁵² It should be noted that the etching parameters for silk fibroin have not been optimized and therefore a performance increase by adjusting the etch conditions can be expected.

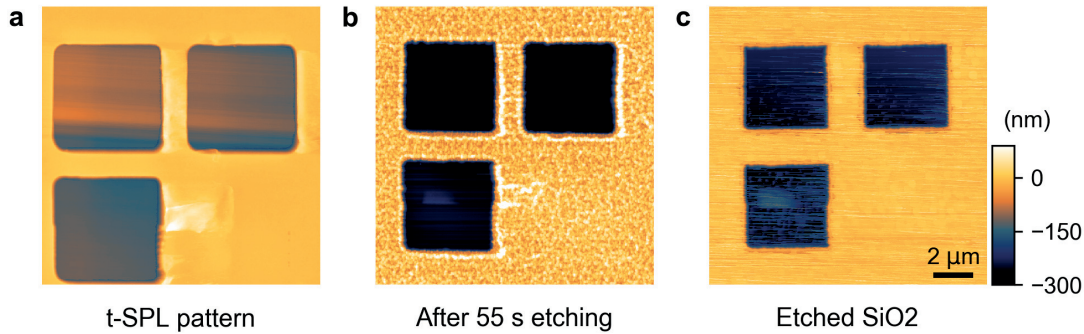


Figure 3.13 – Surface topographies of patterns transferred from silk fibroin into SiO₂ by a He/H₂/C₄F₈-based dry-etch transfer process. (a) Surface topography of 200 nm deep patterns after water development, written by t-SPL on silk fibroin thin film. (b) Surface topography of the silk fibroin after dry etching for 55 seconds in He/H₂/C₄F₈ (c) SiO₂ surface topography after removal of the silk fibroin by an oxygen plasma treatment.

In conclusion, it was shown that silk fibroin in combination with t-SPL can be used as a resist for pattern transfer. Further optimization of the transfer parameters is required, such as thinning of the resist that remained after t-SPL in the patterned area prior to dry etching. An improvement in the surface roughness of the structures is expected. To remove the remaining silk fibroin after dry etching, a solvent is required which dissolves crystalline silk fibroin efficiently without attacking the substrate. Sequential metal oxide vapor infiltration of silk fibroin can further increase the etch selectivity between the substrate and the resist.²⁰⁰

3.4 Conclusion

In conclusion, it is shown that silk fibroin can be used as a resist for t-SPL, based on solubility contrast formation between exposed and unexposed areas. However, the origin of the thermally induced solubility change could not be conclusively identified and further experiments are required. It is shown that a 30 nm deep structures can be written at a pitch size of 100 nm. A numerical simulation is performed to show the heat distribution around the conical tip in silk fibroin, which is identified as a source of the small depth. To achieve a higher resolution, thinner silk films on the order of a few tens of nm could help to confine the temperature closer to the tip. A line edge roughness of 6.9 ± 1.8 nm and 9.3 ± 2.4 nm was achieved in the slow and fast scanning directions, respectively. A comparison between the globular diameter of the silk fibroin molecule on the order of 9 nm is comparable with the experimentally observed line edge roughness and limits the maximum achievable resolution. It is further shown that grayscale lithography with a non-volatile resist such as silk fibroin is possible with t-SPL. However, it should be noted that this comes at a drawback that the final pattern cannot be read out in a closed-loop

lithography manner in comparison to volatile resists. Preliminary experiments on dry etching of silk fibroin in He/H₂/C₄F₈ chemistry show promising results. An etch rate of 160 ± 28 nm/min is experimentally determined, which results in an etch selectivity to SiO₂ of 2.1 ± 0.08 . To show the feasibility of a pattern transfer with silk fibroin, square structures have been transferred from silk fibroin into a 200 nm thick wet oxide layer on silicon. Even though more experiments are required to determine the resolution and the line edge roughness of the proposed process, these first experiments show promising results. It should be noted that silk fibroin, once deposited on a sample and dried, is an extremely stable resist. Some of the samples in this work were used for up to 20 patterning and development cycles without signs of wear. The samples were kept at ambient conditions in a shelf for over a year and could be reused without a noticeable reduction in performance.

4 Nanoscale Thermometry on a Heated t-SPL Probe

4.1 Introduction

The second part of this thesis concerns the planning and construction of an experimental setup for performing nanoscale thermometry on heated atomic force microscopy (AFM) probes. As discussed in Chapter 1, fluorescent nanoparticles, in particular nanodiamonds containing nitrogen vacancy color centers, are suitable as a nanometer-scale temperature sensor. To perform thermometry measurements on fluorescent nanodiamonds mounted to a heated probe, a confocal laser microscope is required with an atomic force microscopy system similar to that of a thermal scanning probe tool. The chapter starts with a short introduction into the theory of NV^- center thermometry, focusing on optically detected magnetic resonance. Then, the thermometry setup and its characterization are described. Finally, preliminary results on nanoscale thermometry are presented.

4.1.1 Theory

The nitrogen vacancy (NV) center is a point defect in the diamond lattice formed by a substitutional nitrogen atom and a vacancy in one of the neighbor lattice sites as shown in Figure 4.1a. In this work, the focus will be on the negatively charged NV center (NV^-), which has triggered interest as a nanoscale magnetic field, temperature and pressure sensor.¹²⁹ The electronic structure of the NV^- center involves six electrons; two are provided by the nitrogen atom and three from the dangling bonds of the surrounding carbon atoms. The sixth electron is captured from the diamond lattice, making it overall negatively charged.

The photophysics of the NV^- center can be explained by three electronic levels: a ground triplet state $|g\rangle$, an excited triplet state $|e\rangle$ and a metastable singlet state $|s\rangle$ as depicted in Figure 4.1b. The ground state exhibits a zero-field fine structure splitting (ZFS) of 2.87 GHz between $m_s = 0$ and $m_s = \pm 1$ state as drawn in the inset. The degeneracy of the $m_s = \pm 1$ state can be lifted by an external magnetic field due to the Zeeman effect.

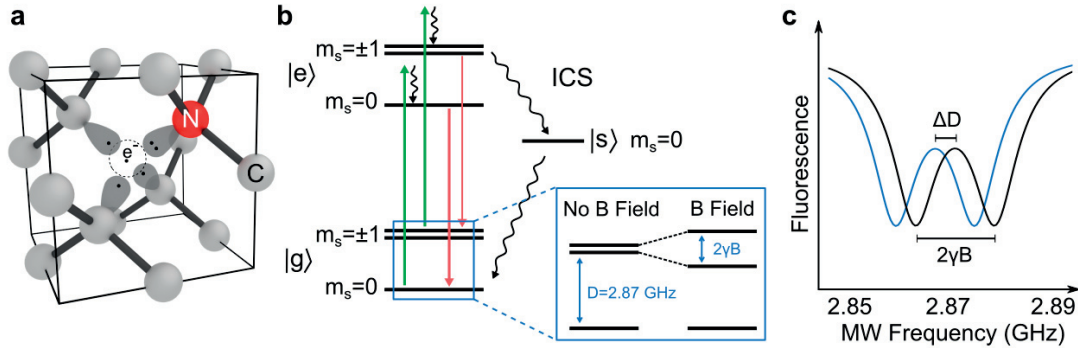


Figure 4.1 – Energy diagram and spectrum of the negatively charged nitrogen vacancy in diamond. **(a)** The lattice structure is shown with carbon atoms (C), the nitrogen atom (N) and the vacancy. **(b)** Orbital diagram with a ground triplet state ($|g\rangle$), an excited triplet state ($|e\rangle$) and a metastable singlet state ($|s\rangle$) with the inter-crossing system (ICS). Straight arrows indicate radiative excitation (up) and relaxation (down), whereas wavy lines indicate non-radiative relaxations. The inset shows the zero-field fine structure splitting of the ground state of 2.87 GHz and the Zeeman splitting of the $m_s = \pm 1$ states under application of an external magnetic field. **(c)** Typical curve of a ODMR spectrum of an NV^- center with a ZFS around 2.87 GHz and the Zeeman splitting between the spin-up and spin-down states.

The NV^- center exhibits further an inter-crossing system (ICS), which preferentially depopulates the $m_s = \pm 1$ state via the singlet state into the $m_s = 0$ state.

One of the interesting aspects of the NV^- center is that its spin state can be optically read out. To do so, the spin is excited from $|g\rangle$ into $|e\rangle$ with a laser (typically $\lambda = 532$ nm) as indicated by green arrows in Figure 4.1b. The optical transitions in the NV^- center are spin conserving, which means that the overall spin after a radiative transition remains unchanged. Unlike the $m_s = 0$ state, the probability of the the excited $m_s = \pm 1$ states to non-radiatively relax via the ICS into the $m_s = 0$ ground state is much higher, which results in an optical contrast between the two states. The probability for the excited $m_s = \pm 1$ states to relax via the ICS is $\sim 30\%$.¹²⁹ The ICS further enables spin polarization by laser pumping for typically 1-2 μs after which the spin populates the $m_s = 0$ state. In a typical optically-detected magnetic resonance experiment (ODMR), a microwave (MW) field around 2.87 GHz is applied in parallel or in sequence to optical excitation to drive the spin transition of the ground state. If the MW is off-resonance, the NV^- center is spin-polarized in the bright fluorescent $m_s = 0$ state. When the MW field frequency is near the resonance, it can efficiently drive the $m_s = 0$ to $m_s = \pm 1$ transition. Due to the partial non-radiative relaxation via the ICS, a reduction in fluorescence is observed. Figure 4.1c shows a schematic curve of an ODMR spectrum at non-zero magnetic field. From the ODMR spectrum, information about the magnetic field, via the strength of Zeeman splitting of the $m_s = \pm 1$ spin, and the temperature and pressure via the ZFS can be obtained.

The NV center's Hamiltonian gives insight how the different perturbations affect the spin energy levels:

$$\frac{H}{\hbar} = D(S_z^2 - \frac{2}{3}) + \gamma \mathbf{B} \cdot \mathbf{S} + \epsilon_z E_z (S_z^2 - \frac{2}{3}) + \epsilon_{xy} (E_x (S_x S_y + S_y S_x) + E_y (S_x^2 + S_y^2)) \quad (4.1)$$

The first term on the right hand side of Equation (4.1) accounts for the ZFS, where D is the ZFS parameter. The second term describes the effect of an external magnetic field with a magnetic field vector \mathbf{B} on the spin energy and the last three terms describe the electric interactions, where E_x , E_y and E_z are the electric field coordinates and ϵ_{xy} and ϵ_z the coupling constants.¹²⁹ \mathbf{S} , S_x , S_y and S_z are the Pauli matrices. The versatility of the NV⁻ center as a sensor stems from the dependence of the $m = \pm 1$ splitting on the external magnetic field and the dependence of the ZFS on strain, pressure and temperature.¹²⁹

In the following section, the origin of the temperature dependence of the ZFS is discussed in more detail.

Origin of the Temperature Dependence of the Zero Field Splitting

In the literature, the temperature dependence of the zero-field splitting D is explained by two contributions: (i) the perturbation of the electronic energy levels by the strain due to thermal expansion ΔD_{ex} and (ii) the difference in vibrational frequencies associated with different electronic levels ΔD_{e-p} .^{130,131} A model for the temperature dependence of D has been proposed by Doherty *et al.* taking into account the energy level shift of the ZFS due to thermal expansion and electron-phonon coupling.¹³¹ The contribution to ΔD due to thermal expansion can be understood by a shift of the electronic energies of the NV⁻ centers as a consequence of the expansion of the nuclei's equilibrium position with temperature. The temperature dependence of ΔD can be expressed as:

$$\Delta D_{ex}(T) = A \cdot P(T) = AB \int_0^T e(t) dt, \quad (4.2)$$

where $A = 14.6$ MHz/GPa is the experimentally determined shift of the zero-field splitting with hydrostatic pressure $P(T)$, $B = 442$ GPa is the diamond bulk modulus and $e(t)$ is the temperature dependent volume expansion coefficient of diamond.

The electron-phonon interaction contribution to the shift of $D(T)$ can be expressed as

$$\Delta D_{e-p}(T) = \hbar \int_0^{\Omega} n(\omega, T) \delta(\omega) \rho(\omega) d\omega, \quad (4.3)$$

where $n(\omega, T) = 1/(e^{\hbar\omega/k_B T} - 1)$ is the thermal distribution of vibrational occupations, $\Omega \sim 165$ meV the highest vibrational frequency of diamond, $\rho(\omega)$ the vibrational density of modes and $\delta(\omega)$ the average vibrational frequency difference between the electronic states.

By expansion of the overall frequency shift $\Delta D(T) = -\Delta D_{ex}(T) - \Delta D_{e-p}(T)$ up to the fifth order, its temperature dependence can be expressed as:

$$\Delta D(T) \approx -\frac{e_1}{2} AB T^2 - \frac{e_2}{3} AB T^3 - \left(b_4 + \frac{e_3}{4} AB\right) T^4 - \left(b_5 + \frac{e_4}{5} AB\right) T^5, \quad (4.4)$$

where e_i are the thermal expansion coefficients and b_i the coefficients accounting for electron-phonon interaction.²⁰¹

Figure 4.2a shows an overview of different experimental curves of $D(T)$ found in literature. Chen *et al.* experimentally determined $D(T)$ for ensembles of NV⁻ centers in bulk diamond in the temperature range from 15 to 300 K.²⁰² Doherty *et al.* confirmed the findings for a single NV⁻ center between 5 and 300 K and developed a model to explain the origins of the temperature dependence of D as discussed above.²⁰¹ Toyli *et al.* measured $D(T)$ from room temperature to 700 K on single NV⁻ centers in bulk diamond, which overlap with low temperature measurements at room temperature.¹³⁰ Plakhotnik *et al.* and Laraoui *et al.* recorded $D(T)$ for nanoparticles.^{111,135} Their ZFS is shifted with respect to the bulk diamond curves, which could be due to strain in the crystal lattice affecting the thermal expansion or to the small particle size which affects the density of vibrational modes $\rho(\omega)$.¹³¹

Not only the ZFS shift but also the fluorescence intensity, has been explored for thermometry. Figure 4.2b shows the normalized fluorescence intensity as a function of temperature obtained from experiments found in literature. Fluorescence intensity measurements from a single NV⁻ center in a bulk diamond crystal was performed by Toyli *et al.*, whereas Laraoui *et al.* and Plakhotnik *et al.* used diamond nanoparticles. The curve from Toyli *et al.* exhibits a considerable decrease in fluorescence intensity above ~ 550 K. A similar decrease was observed by Laraoui *et al.* at ~ 500 K. Plakhotnik *et al.* found that the fluorescence intensity change as a function of temperature considerably differs between measurements obtained from 10 similar nanoparticles, as shown in Figure 4.2b. The solid

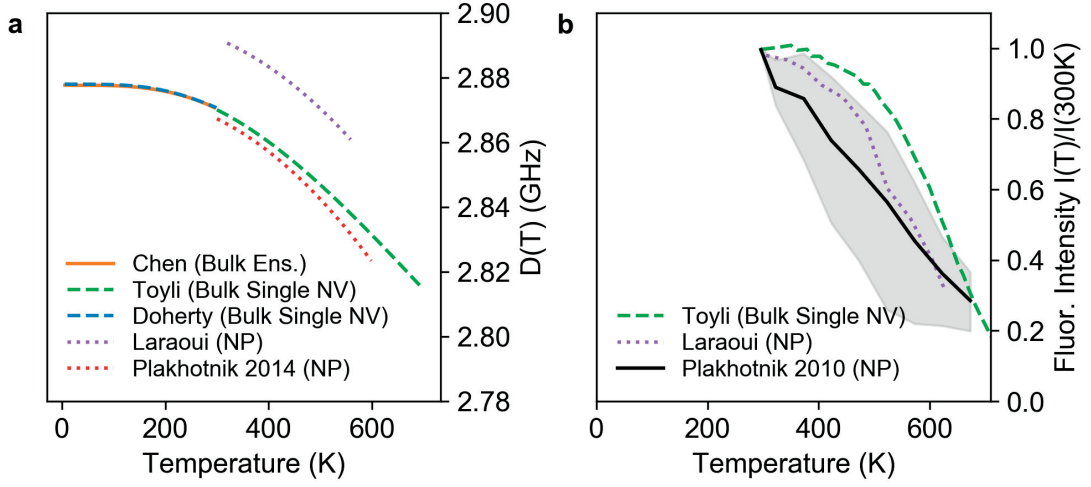


Figure 4.2 – A comparison of experimental data on the temperature dependence of the ZFS and the fluorescence intensity in literature. **(a)** The zero field splitting parameter is plotted against the temperature. Measurements from Doherty¹³¹, Toyli¹³⁰ were performed on single NV^- centers in bulk diamond. Chen imaged NV^- center ensembles in bulk diamond.²⁰² For the measurements by Plakhotnik¹³⁵ and Laraoui,¹¹¹ NV^- center ensembles in diamond nanoparticles were used. **(b)** The normalized fluorescence intensity is plotted against the temperature from experiments performed by Toyli and Laraoui. The black solid line is an average intensity from 10 nanocrystals measured by Plakhotnik and the gray shaded area represents the range of the minimum and maximum values.¹¹⁰

black line is the average fluorescence intensity and the gray area represents the range of all measurements. It is clear that due to these considerable deviations, each nanoparticle would need to be calibrated for intensity-based NV^- nanothermometry.

Limitations and Advantages of NV^- Center Based Thermometry

Spin lifetime measurements revealed that non-radiative processes diminish the spin-selectivity between $|g\rangle$ and $|e\rangle$ transition and limit the maximum measurable temperature with ODMR-based thermometry to 670 K.¹³⁰ Variations between diamond nanoparticles, such as structural defects, impurities, strain and the surface morphology can affect temperature measurements. Doherty *et al.* studied the effect of impurities on the ZFS shift as a function of temperature. While the impurities seem to have an effect on the thermal expansion, the overall ZFS shift is less sensitive to impurities, presumably due to the dominant contribution of the electron phonon interaction $\Delta E_{e-p}(T)$. On the other hand, it is expected that for very small diamonds, the density of vibrational modes $\rho(\omega)$ is modified and will change $\Delta E_{e-p}(T)$ compared to bulk diamond.¹³¹ Another limitation is the emission rate of the NV^- center and the collection efficiency of the optical components. It is estimated that the theoretical detection count rate from a single NV^- center in a nanocrystal is 20 MHz. However, the numerical aperture of the objective, incomplete

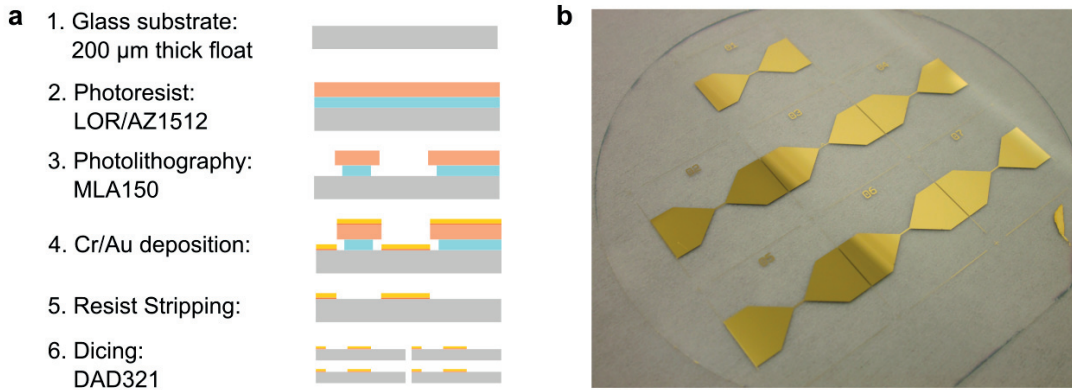


Figure 4.3 – Overview of the microwave antenna fabrication. **(a)** Process flow of the fabrication process **(b)** The glass wafer with the gold microwave antennas before dicing.

spin polarization and accumulation of the center in the metastable non-radiating state reduce the maximum count rate to 200-500 kCts/s.²⁰³

A distinct advantage of NV^- center thermometry in comparison to other luminescence thermometers is that the temperature-dependent signal is independent of the illumination and fluorescence intensity. For tip-based thermometry, this is important since the nanoparticle might not experience the same laser intensity throughout an experiment, where for example, the tip location is changed.

4.2 Materials and Methods

In the following section, sample preparation with the diamond particles and fabrication of the MW antenna are described. The description of the optical setup for thermometry and its characterization are described in Section 4.3.

4.2.1 Diamond Nanoparticles and Sample Preparation

All fluorescent diamond particles used in this work were purchased from Adamas Nanotechnologies Inc. and contain 3 ppm NV^- centers as specified by the supplier. Diamond particles with a diameter of 1 μm were provided in powder form and were distributed on the sample under an optical microscope with a toothpick. Smaller particles with an average size of 140 and 40 nm were provided in suspension (1mg/mL) and contained, on average, 800 and 12-14 NV^- centers per particle, respectively. To control the distance between the particles on the sample, the suspensions were diluted with DI water to concentrations of 0.1 mg/mL and 0.01 mg/mL prior to spincoating.

4.2.2 Fabrication of the Microwave Antenna

The microwave antennas were fabricated using a standard lift-off process as shown in Figure 4.3a. A 220 μm thick 4-inch glass wafer was spincoated with 0.82 μm thick LOR-5A resist and 1.1 μm thick AZ1512. The resist was exposed with a maskless laser writer (MLA150, Heidelberg Instruments GmbH). A 15 nm thick chromium adhesion layer was sputter deposited, followed by a 250 nm thick gold layer. The resist was stripped with NMP remover and the wafers were diced (DAD321, Disco Corp.) into $25 \times 25 \text{ mm}^2$ large chips. The gold lines were 280 μm in width. Figure 4.3b shows the final glass wafer with the gold microwave antennas before dicing.

4.3 NV⁻ Thermometry Setup

In the following section, the assembly of a platform is described that was planned, built and characterized as a part of this thesis to perform fluorescence based thermometry in combination with thermal scanning probes. The setup is composed of two parts: an optical part which includes a laser, various optical components and a detection system, and a scanning part, which allows for positioning and powering the thermal scanning probes. While many commercial solutions for fluorescence based microscopy exist, a custom setup offers more flexibility to add components at a later stage.

The setup is built on an actively damped optical table (RS 100, Newport Inc.) to reduce mechanical vibrations from the environment. An overview of the setup with the table and an aluminum frame to accommodate the electronic components is shown in Figure 4.4. The frame is furthermore equipped with light-tight curtains to reduce background illumination. The figure also shows the laser, the inverted microscope with the sample and cantilever scanning stages and the optical enclosure for the detectors. In the following sections, all components are discussed in more detail.

4.3.1 Laser

The design of the laser is adapted from Oeckinghaus *et al.*²⁰⁴ with major improvements concerning the laser alignment. The laser is shown in Figure 4.5a and is composed of a green GaN laser diode (LD-520-50SG, Roithner) with a typical emission wavelength of 520 nm, a spectral width of 2 nm and a maximum optical output power of 50 mW.²⁰⁵ The diode is soldered via two wires to a laser diode driver (LDP-V03, PicoLAS), which is connected to a pulse generator module (PLCS-21, PicoLAS). The pulse generator is steered by the computer via a USB cable to set the pulse length, frequency, voltage and other parameters. No additional cooling for the diode is required in our experiments. Before performing any experiments, the laser must stabilize for 30 minutes. The diode is fixed to a dedicated holder (S1LM38, Thorlabs Inc.), which is mounted to a translational

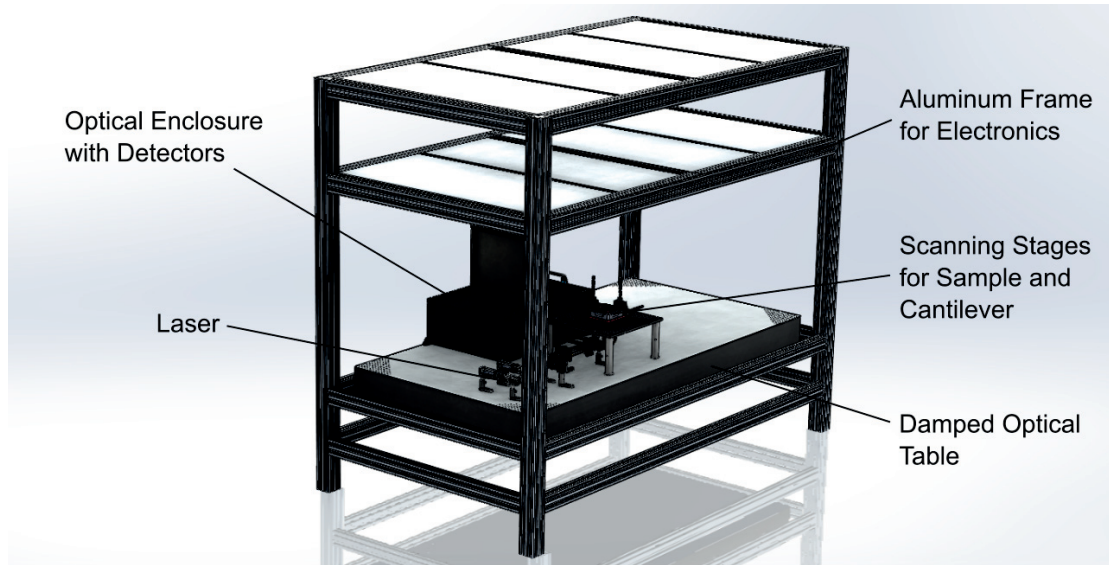


Figure 4.4 – CAD drawing of the optical setup, which is composed of an aluminum frame with shelves at the top to accommodate the electronics, an actively damped optical table, a laser and a inverted microscope with stages for the sample and the thermal probe, and an optical enclosure for the optical detectors. In addition, black curtains are attached to the frame to reduce background illumination.

mount (SPT1, Thorlabs Inc.) to facilitate alignment with respect to the system’s optical axis. The diode beam is collimated by using an aspheric lens with a focal length of 3.1 mm (C330TMD-A, Thorlabs Inc.), which is mounted on a translational stage (SM1Z, Thorlabs Inc.), allowing for precise collimation. Due to the divergence of the laser diode beam by 22° in the fast and 6° in slow axis directions, additional beam shaping is required to obtain a circular beam. An anamorphic prism pair (PS883-A, Thorlabs Inc.) with a magnification of $4\times$ was used to expand the beam in the slow axis direction. The laser beam is directed towards the sample stage as described in the following section.

4.3.2 Confocal Laser Microscope

To match the beam diameter with the objective’s backfocal plane diameter, the laser beam is expanded using two planoconvex lenses with a focal length of 30 mm (LA1805-B, Thorlabs Inc.) and 100 mm (LA1509-B, Thorlabs Inc.). A pinhole with an aperture of $20\ \mu\text{m}$ (20S, Thorlabs Inc.) placed in between the lenses reduces stray light from the diode as depicted in Figure 4.6. The laser beam is then reflected from a high-pass dichroic mirror (DMCP550R, Thorlabs Inc.) working at a cut-off wavelength of 550 nm towards a dielectric mirror (BB1-E02, Thorlabs Inc), which deflects the beam in the vertical direction into the objective (UPLSAPO 40X2, Olympus). The objective was operated in air at a magnification of $40\times$, with a high numerical aperture of 0.95 at a large solid angle for photon collection. The objective is vertically mounted on a

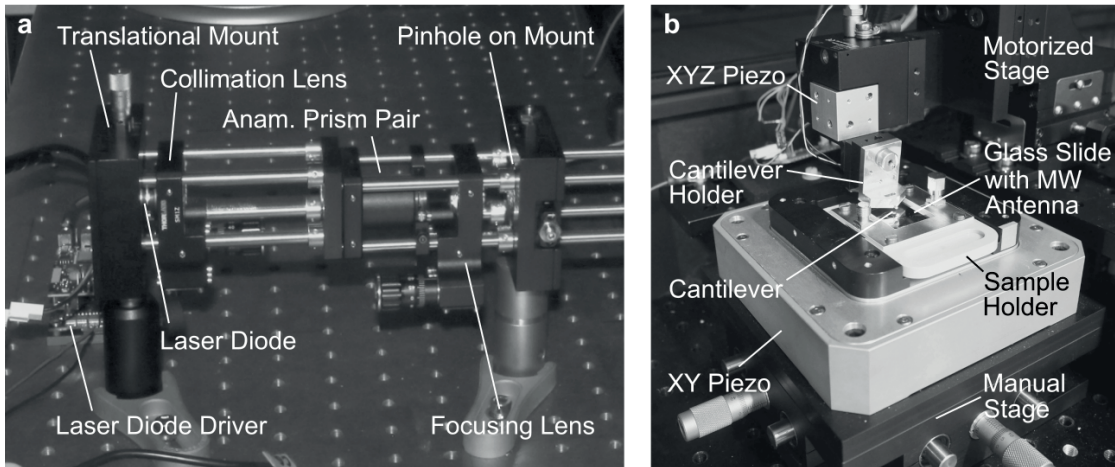


Figure 4.5 – Photography of the laser and the inverted microscope with the scanning stages. **(a)** The laser diode driver with the diode and optical components for beam shaping and alignment are shown. **(b)** The inverted optical microscope with the sample scanning stage (XY Piezo) and the sample holder is shown. The objective is situated below the glass slide with the MW antenna. The cantilever is located above the sample and can be moved via a piezoelectric actuator (XYZ Piezo) and a motorized stage.

translational stage below the sample holder with three degrees of freedom to align it with respect to the laser beam and a single axis piezoelectric actuator to focus on the sample. Figure 4.5b shows the sample stage, which is composed of a glass slide holder mounted on a two axis piezoelectric actuator. The light from the sample is collected by the same objective, passes through the dichroic mirror and is focused (LA1131-A, Thorlabs Inc.) on a 15 μm diameter pinhole (15S, Thorlabs Inc.). The pinhole blocks all light, except in the confocal volume, and therefore allows higher spacial resolution in comparison to conventional wide-field optical microscopes.²⁰⁶

4.3.3 Fluorescence Detection

To prevent light contamination from any external sources, the detection path of the optical setup, including the beam splitter and the detectors, are placed inside an optical enclosure made out of black hardboard (TB4, Thorlabs Inc.) as depicted in Figure 4.6. After passing the pinhole, the beam is collimated (LA1131-A, Thorlabs Inc.) and split with a 50:50 beam splitter (BS016, Thorlabs Inc.) into two beams. One beam is focused (LA1131-A, Thorlabs Inc.) on a red-enhanced silicon photodiode (SD 100-11-21-221, Advanced Photonix Inc.), which is used mainly for alignment of the setup with highly fluorescent particles. The second beam is focused on a single photon detector (SPCM-AQRH-14-TR, Excelitas), which is used to detect low level emission from fluorescent nanoparticles. The photon counting module is attached to a custom-made aluminum block, specifically built for efficient cooling. It is further mounted on a XYZ translational

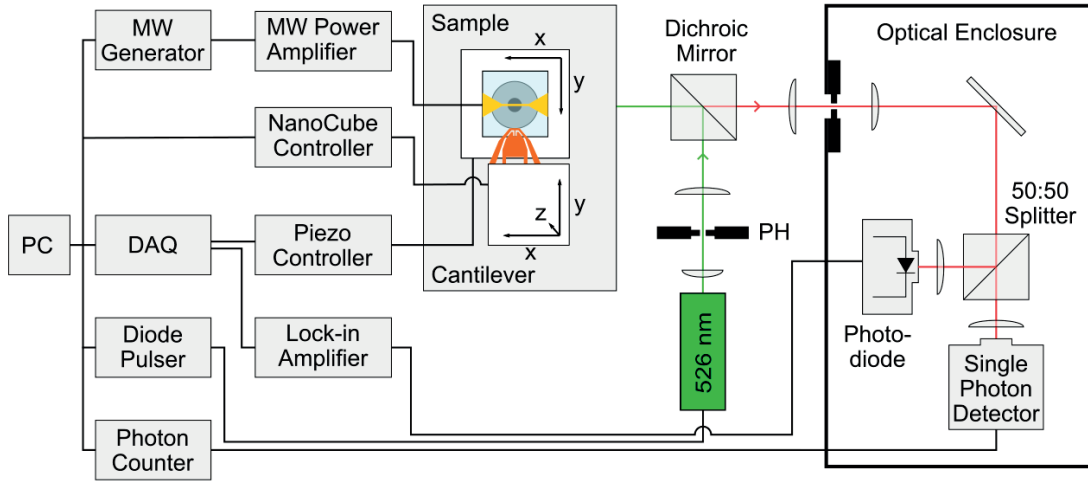


Figure 4.6 – Schematic overview of the NV^- setup. The gray boxes on the left represent the electronic parts such as computer, controller and acquisition boards. In the center, the scanning stage, objective and the cantilever are shown. The laser and the detection system are located on the left side. The detection arm is placed in an optical enclosure to reduce light contamination.

stage (M-D240-7, Newport Corp.) to enable alignment of the detector with respect to the optical axis. The signal from the red-enhanced silicon photodiode is amplified with a transimpedance amplifier (Model 181, Princeton Applied Research) and a digital lock-in amplifier (SG384-DSP, Stanford Research Systems). In order to reduce the noise, the laser was modulated at a frequency of 528.2 Hz (33120A, Hewlett Packard). The signal of the photodiode from the lock-in amplifier is recorded by a data acquisition board (PCIe-6259, National Instruments) via a shielded connector block (BNC-2110, National Instruments). The photon counter module, on the other hand, is connected to a time-correlated single photon counting module (PicoHarp300, PicoQuant), which is directly plugged into the computer via a USB cable.

4.3.4 Sample Stage

A custom-made sample holder is used to efficiently clamp and exchange $25 \times 25 \text{ mm}^2$ sized coverslip samples as shown in Figure 4.5b. In addition to mechanical clamping, the sample holder establishes an electrical contact to the MW antenna on the glass slide. The holder is placed on a two-axis piezoelectric stage (P-734.2CL, Physik Instrumente) with a range of $100 \mu\text{m}$, which itself is mounted on a manual stage (M-406, Newport Corp.) for quick alignment of the sample with respect to the laser beam. The position of the piezoelectric actuators is controlled by an analog output signal from the data acquisition board (PCIe-6259, National Instruments) via a three axis servo controller (E-725, Physik Instrumente). The stage position is capacitively measured with integrated sensors and recorded by the data acquisition board.

4.3.5 Positioning and Resistive Heating of the Thermal Probe

Coarse positioning of the thermal scanning probe is performed with a three-axis motorized stage (PT3-Z8, Thorlabs Inc.). An additional three-axis piezoelectric stage (P-616 NanoCube™, Physik Instrumente), is mounted on the motorized stage to control the approach and scanning of the thermal cantilever as shown in Figure 4.5. It is connected to the computer via a controller (E-727, Physik Instrumente).

Commercial thermal scanning probes (Monopede HPL, Swisslitho) are used, which are clamped to a dedicated holder with three metal connectors that serve as mechanical and electrical contacts. The cantilevers are made of phosphorous doped silicon ($n_n \sim 10^{20} \text{ cm}^{-3}$)¹⁶¹ and consist of three legs, as shown in Figure 4.7a. At the front of the cantilever, two resistive heaters are implemented, defined by a low doped region ($n_n \sim 10^{19} \text{ cm}^{-3}$) and indicated in *red* in Figure 4.7a. The heater in the top leg (hereafter named *Reader*) serves as a thermal height sensor to readout the distance of the cantilever with respect to the sample surface. The heater in the central leg (hereafter named *Writer*) heats a 500 nm long conical tip mounted below the heater and is used during thermal patterning. The third leg is the common ground.

Both heaters are powered by a computer-controlled DC power source (E3649A, Agilent) via a circuit as drawn in Figure 4.7b. With the DAQ board, the voltage drop across the series resistors R_{SR} and R_{SW} is measured to determine the *Reader* resistance R_R and the *Writer* resistance R_W , respectively. R_R and R_W are calculated as follows:

$$R_R(z) = \frac{V_R}{V_{appl} - V_R} R_{SR} - R_{Leg} \quad (4.5)$$

$$R_W(z) = \frac{V_W}{V_{appl} - V_W} R_{SW} - R_{Leg} \quad (4.6)$$

where $R_{SR} = 5085 \text{ } \Omega$ and $R_{SW} = 5105 \text{ } \Omega$ are the series resistances, and R_{Leg} is the resistance from the legs. Since the cantilever resistance is dominated by the resistance of the low-doped areas, R_{Leg} can be neglected.

4.3.6 Microwave Magnetic Field Generation

The microwave magnetic field, required to drive the $m_s = 0$ to $m_s = \pm 1$ spin transition, is generated by a MW antenna which was fabricated as described in Section 4.2.2. The MW signal is created with a microwave generator (SG384, Stanford Research Systems) and amplified by 45 dB with a high-power amplifier (ZHL-16W-43+, Mini-Circuits). Between the generator and the amplifier, the signal is attenuated by 17 dB (7 dBm/18 GHz/2 W, Mini-Circuits and 10 dB/16 GHz/2 W, Huber+Suhner AG). The amplifier is connected

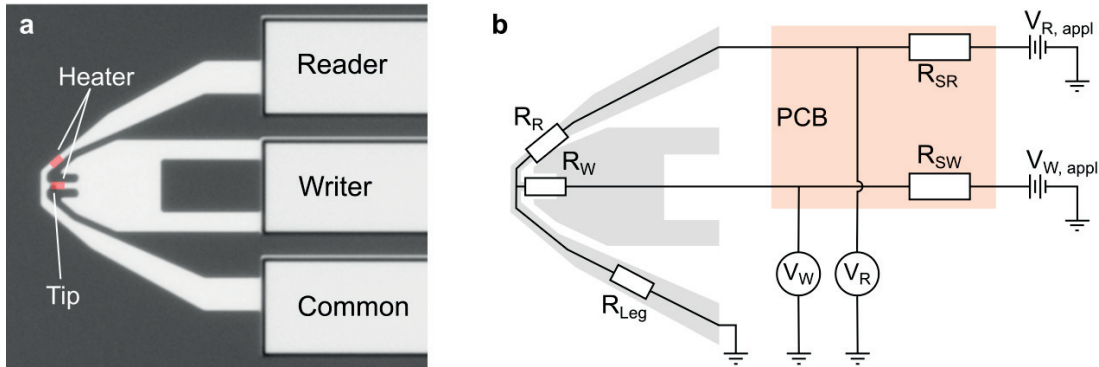


Figure 4.7 – Electrical connection of the cantilever. (a) Optical microscopy image of the cantilever with the *Reader*, *Writer* and *Common* legs. The *Reader* and *Writer* heater are colored red. (b) Schematics of the electronics to power the cantilever and measure its current-voltage characteristics.

to the sample via a coaxial cable, which then transfers the MW signal to the MW antenna as shown in Figure 4.5b.

4.3.7 Software

The software for the thermometry setup was implemented in LabView (Version 2016, National Instruments Inc.), which is a system design platform using a visual programming language. The software was designed to interface the electronics, such as the laser diode pulser, the position controller, the microwave generator and the cantilever’s power source, and to control the sequence of experiments such as optically detected magnetic resonance or scanning of the surface. Three standalone programs were designed: A positioning/scanning software, a program to optically detected magnetic resonance and one to perform tip characterization. Each program will be briefly discussed in the following sections.

VI to Perform Positioning and Scanning

The scanning/positioning virtual instrument (VI) was designed to perform multiple tasks in one program such as: fine/coarse alignment, positioning, scanning and data acquisition. To perform these tasks, the program continuously acquires data from all sensors such as the position of the piezoelectric actuators, measured cantilever resistance, photon detector count rate, etc. All data is displayed in real-time in the user interface. At the same time, the user can perform actions such as changing the settings or moving the stages while immediately receiving feedback about the updated measured positions or fluorescence intensity. Due to the complexity of the program and in order to facilitate extensibility a few design principles were applied:

4.3. NV⁻ Thermometry Setup

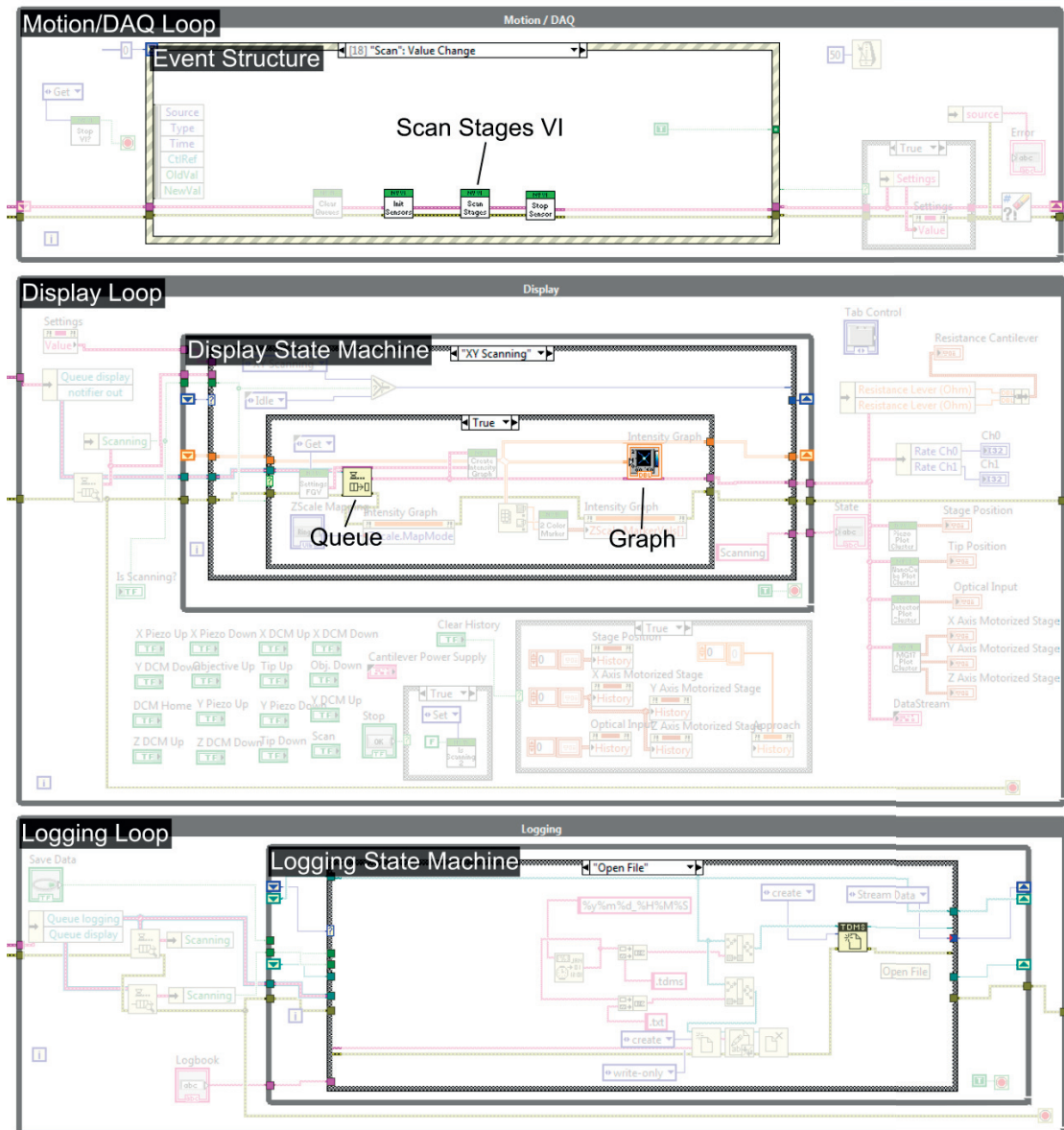


Figure 4.8 – Scanning VI for the thermometry setup, composed of three main loops. The top loop is responsible for motion control and data acquisition and sends the acquired data to a *Queue* which is processed by the other two loops. The center and bottom loops are responsible for displaying and data logging, respectively. The design pattern follows a *Producer/Consumer* scheme, which, for example, keeps the user interface responsive and ensures chronology of the recorded data. For the sake of simplicity, components irrelevant to the understanding of the program are grayed out.

- A *Producer/Consumer* design pattern is applied to allow different parts of the software to run in parallel at a different speed without loss of data
- Data flow is structured in *Clusters*, which are grouped in “Settings” and “Acquired data”

- Extensibility and reusability is facilitated by using type definition *Type Def*
- Communication across loops is performed via *Functional Global Variables*
- Subtasks are encapsulated in SubVIs
- A *State Machine* design pattern is applied for complex logic

Figure 4.8 shows the Labview diagram of the scanning VI, whereby elements unimportant for the understanding of the working principle are grayed out. The basic software is composed of the three *While loops*: *Motion/DAQ*, *Display* and *Logging*, following the *Producer/Consumer* design pattern. The *Motion/DAQ* loop holds the *Producer* role, whereas the other two are *Consumer* loops.

The *Motion/DAQ* loop contains an *Event structure*, which captures actions from the user such as changing a setting, pressing a button or a keyboard key. According to the event that occurred, a different sequence of instructions is executed. As an example, in Figure 4.8, the sequence for the scanning event is shown, which is triggered by the “Scan” button in the user interface. The first subVI “Init Sensors” initiates sensors such as the thermal height sensor. The second subVI “Scan Stages” performs the scanning of the stages and is built such that any combination between detectors and scan axis is possible. During scanning, the acquired data is chronologically appended to a *Queue* from which the *Consumer loops* will retrieve the data. In the third subVI “Stop Sensors”, the sensors that do not need to run continuously (such as the thermal height sensor) are terminated.

The *Display* loop accommodates all elements from the user interface such as buttons or graphs and continuously reads data from the *Queue*. The structure inside the *Display* loop is a *State Machine*, which, depending on the state, displays the data in a specific graph or diagram. As an example, the diagram for a two-axes scan is shown. The position of the two axes and the signal (e.g. the fluorescence count rate) retrieved from the *Queue* are used to compile the image, which is displayed in the graph. The concept applies also for a single axis scan, such as the approach with the thermal probe to the surface, which is then displayed in a diagram.

The *Logging* loop follows the same design pattern as the *Display* loop. As an example, the diagram is shown, which is used to open a new file to stream the data.

SubVI to Scan the Stages

While most subVIs will not be discussed in detail here, the principle of how the scanning of the stages is implemented will be explained. The SubVI to perform different types of scans is located in the *Motion/DAQ* loop as indicated in Figure 4.8. As an example, the diagram for a two-axes scan of the thermal probe is shown in Figure 4.9. The structure is composed of two *For Loops*, one for each axis. The outer loop updates the Y position of the piezoelectric actuator and the inner loop the X position. The computation of the X

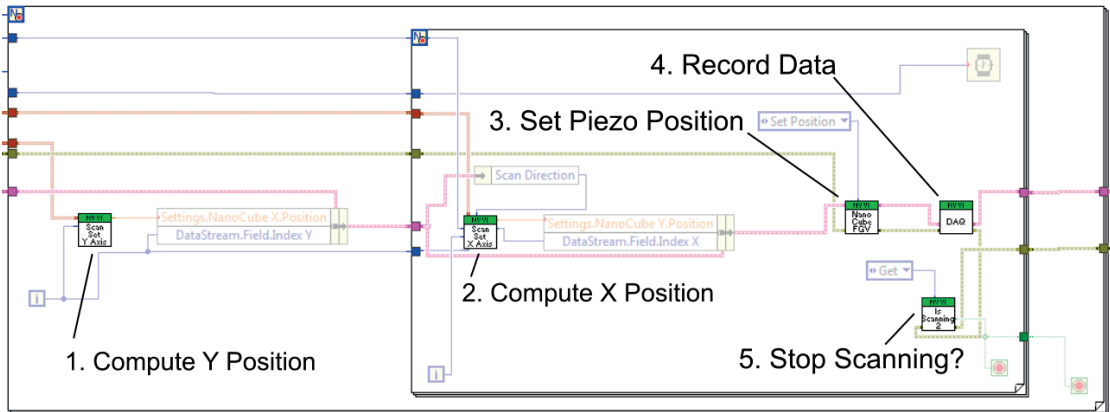


Figure 4.9 – The figure shows a scheme that was used for various scanning tasks and is composed of two *For Loops* in which the position of the stage (here the NanoCube with the cantilever) is updated via the *NanoCubeFGV* SubVI and all signals are acquired via the *DAQ* SubVI.

and Y position is encapsulated into the subVIs “Scan Set X Axis” and “Scan Set Y Axis”, which facilitates the implementation of complex scan patterns. The stage coordinates are sent to the specific stage controller and all data is recorded and appended to a *Queue* as described in the previous section. To allow the user to abort the scan in progress, a *Functional Global Variable* is used to check if the stop button has been pressed.

VI to Perform Optically Detected Magnetic Resonance Experiments

The optically-detected magnetic resonance is recorded in a separate VI as shown in Figure 4.10. This VI makes it possible to set the frequency range of the sweep and the number of averages performed as well as display the continuous count rate of the single photon detector (*top graph*), the optical power of the regular silicon photodiode detector (*center graph*), the data from each individual microwave sweep (*bottom left*) and the average signal vs. microwave frequency (*bottom right*). During a ODMR experiment, the cantilever voltage can be controlled to perform thermometry experiments. The necessary data is saved into a *TDMS* file after the MW scan has been terminated.

4.4 Characterization and Calibration

Characterization and calibration of the optical setup are necessary to measure and optimize the system’s performance as well as to ensure that the performance does not reduce over time without being noticed. In the following sections, the calibration and characterization of important components is presented.

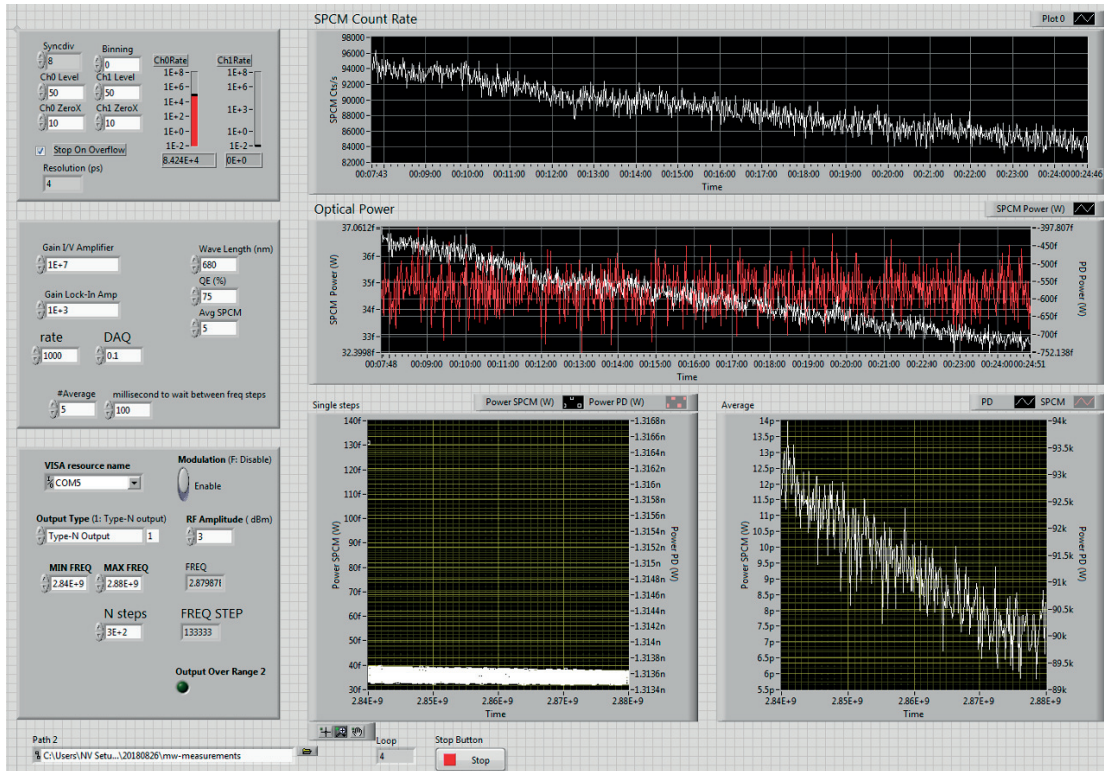


Figure 4.10 – User interface of the VI to perform ODMR experiments

4.4.1 Optical Alignment

A crucial and time consuming part of building and maintaining a laser microscope, is alignment of the optical components. Therefore, a procedure to coarse and fine align the optical components is described, which has proven useful. The optical setup is coarse aligned using a green laser ($\lambda=526$ nm) as shown in Figure 4.6 and a red laser, which is placed at the location of the silicon photodiode. By iteratively adjusting the mirrors and pinholes, the laser beams were aligned such that the two rays overlap at a distance of ~ 2 m from the position of the objective. The shape of the green laser beam is observed on a white wall and featured a nearly circular shape. After mounting back the objective and the silicon photodiode in place of the red laser, the detection path is aligned under illumination from a white LED placed in front of the objective. Since the light intensity of the beam through the pinhole is visible by eye, it is possible to coarse align the photosensitive areas of both detectors, while being switched-off. In a second step, the detectors were fine aligned by maximizing the signal from optically excited fluorescent microparticles (MDNV1umHI, Adámas Nanotechnologies Inc.) with a diameter of $1 \mu\text{m}$. During the alignment of the single photon detector, the optical enclosure needs to be opened to manipulate the position of the pinhole and mirrors. Since these detectors are extremely sensitive to light, the alignment had to be performed in the dark without a computer screen. To obtain feedback for maximizing the transmitted light,

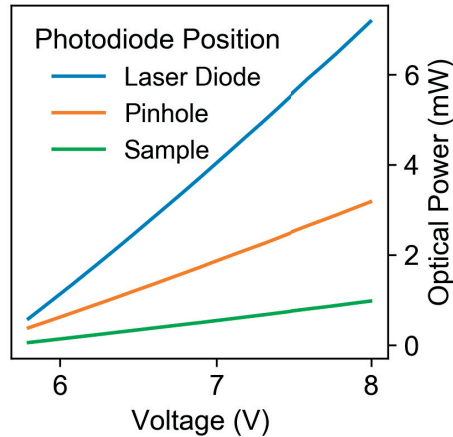


Figure 4.11 – Optical power measured with a calibrated photodiode at the laser diode, after the pinhole and at the sample position after the objective.

a LabView program is used, which converts the count rate into an audio signal whereby higher frequencies correspond to a higher count rate and *vice versa*. The room in which the setup is located is temperature controlled (~ 0.1 K) to reduce temperature induced misalignment of the components. Despite temperature control, fine-adjustments have to be performed approximately once a month in order to correct for small misalignments over time.

4.4.2 Laser Power Calibration

The power of the laser is determined with a calibrated 1×1 cm² large photodiode (FDS1010-CAL, Thorlabs Inc.). The photodiode has a sensitivity of 0.2 A/W at a wavelength of 530 nm. To compute the average power, the laser is pulsed at a repetition rate of 500 kHz with a pulse duration of 500 ns. In Figure 4.11, the power is plotted as a function of the applied voltage to drive the laser diode. The laser power increases linearly with the applied voltage up to the maximum operating potential of 8 V. At 7.8 V, an optical power of 7.18 mW is measured at the laser diode, 3.18 mW after the pinhole and 0.98 mW at the sample position. Most of the light intensity is lost at the pinhole and the backfocal plane of the objective.

4.4.3 Electrical Characterization of the Cantilevers

The current-voltage characteristics of each cantilever are measured prior to thermometry experiments. The cantilever is powered with the circuit as described in Section 4.3.5. The current-voltage curves were recorded by sweeping the applied voltage from 1 to 10 V, while measuring the potential drop across the cantilever as shown in Figure 4.12 and Equation (4.5) is used to compute the cantilever resistance. In Figure 4.12a, a

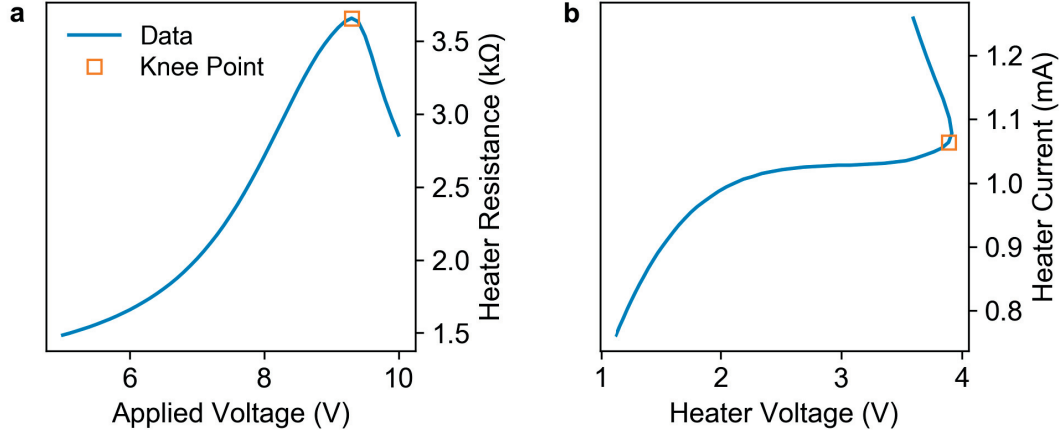


Figure 4.12 – Electrical characterization of the cantilevers. (a) The graph shows the *Reader* heater resistance as a function of the applied voltage. The knee point is indicated by a square marker. (b) The heater current is plotted against the voltage across the *Reader* sensor. Beyond the knee point, the current rapidly increases due to a decrease in the resistance from thermally activated charge carriers.

typical resistance-voltage curve for the *Reader* heater is plotted. The square indicates the knee point, where the resistance is the highest. At low voltages, the doped silicon resistor exhibits an ohmic behavior. With increasing temperature of the heater at higher voltages, more charge carriers are thermally excited into the conduction band. Above the knee point, the resistance is dominated by thermally activated carriers and therefore decreases with increasing voltage.¹⁶⁰ The current rapidly increases above the knee point as shown in Figure 4.12b, which makes it necessary to add a resistor in series to the silicon heater to avoid damaging the heater. The knee point can be used to calibrate the heater temperature since the temperature at which the peak resistance of a semiconductor appears can be analytically calculated.¹⁶⁰

4.4.4 Surface Detection and Surface Metrology with Thermal Scanning Probes

In this section, the procedure to detect the sample surface with the integrated height sensor in the thermal scanning probe is described. A potential of 8 V is applied across the *Reader* heater R_R and the series resistor $R_{SR} = 5085 \Omega$ (see Figure 4.7b), while the voltage across the *Reader* resistance is continuously measured during a surface approach as plotted in Figure 4.13a. The tip-sample distance is reduced until the tip touches the substrate. This point can be detected by a change in the slope of the approach curve as shown in the inset. In this setup, the criteria to stop the approach is defined via a threshold $\frac{1}{V_{min}} \frac{d^2 V(z)}{dz^2} < -\frac{0.1}{\text{nm}^2}$ at a step size of 20 nm. From the approach, the position of the piezoelectric actuator where the tip touches is determined by fitting the curve before

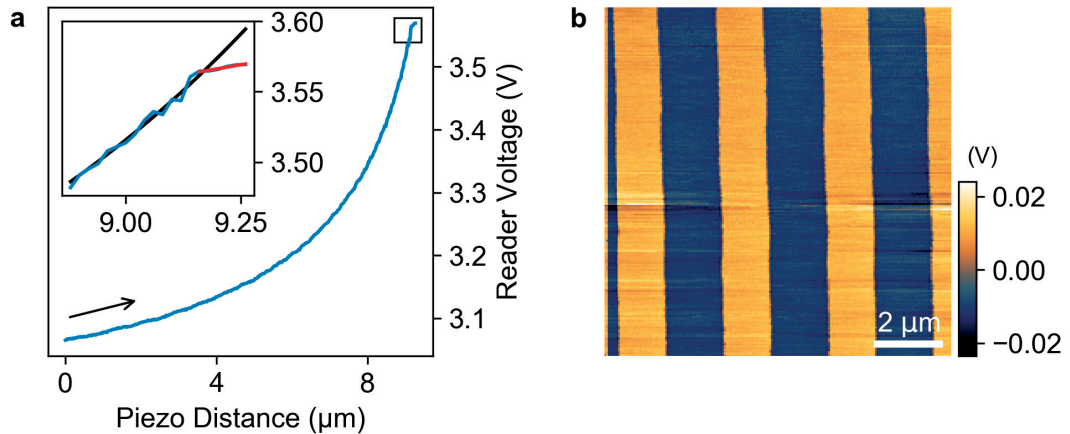


Figure 4.13 – Approach curve of the thermal scanning probe to the substrate and topography scan of a reference sample. **(a)** Plot of the *Reader* voltage against the piezo distance during an approach. The inset shows a magnification of the curve where the tip touches the surface. **(b)** Topography scan of a reference silicon sample with 2 μm wide and 100 nm high structures. The contrast signal is the potential drop over the *Reader* series resistor.

contact with a third order polynomial (*black* line) and the curve after contact with a first order polynomial (*red* line) as shown in the inset in Figure 4.13a. The contact point is calculated as the intersection of both fitted curves.

Thermal height sensing is also used to image the surface topography. Topography scans of the surface are performed by placing the tip into contact with the sample and scanning the area of interest line by line. Figure 4.13b shows a surface topography scan obtained from a AFM calibration grid (TGZ02, MikroMasch) made of 1.5 μm wide 100 ± 1.5 nm high stripes in silicon. The scan is performed at a pixel size of 50 nm and a pixel time of 50 ms. The topography contrast is provided as the voltage change over the series resistor of the reader sensor. One can see that the lines could be reproduced. However, some of the vertical lines are laterally shifted with respect to each other. From these results it is clear that basic imaging of the surface topography with the scanning probe is possible, but for quantitative measurements the procedure has to be further refined.

4.4.5 Tip Alignment with Respect to the Laser Beam

To finely align the laser with respect to the tip apex of the cantilever, the reflected laser light from the cantilever and the laser-induced resistance change in the cantilever can be used to create an image of the cantilever by scanning it over the laser. From the interaction of the laser beam with the cantilever, the location of the tip and the heater region can be identified as shown in Figure 4.14a.

The first method to create an image of the cantilever exploits the fact that when the laser is focused on the cantilever, a large portion of the laser light is reflected and coupled back into the optical path. Despite the dichroic mirror and the high-pass filter in front of the photon detector, a measurable amount of light passes towards the single photon detector. Figure 4.14a shows an image which displays the count rate of the reflected light while the cantilever is scanned over the laser beam. The highest counts are obtained when the laser beam is on top of the silicon surfaces which are normal to the laser beam (160-175 kCts/s). When the laser is focused on the tip, which is indicated by a circle, due to its conical shape, more rays are deflected at angles beyond the collection angle of the objective. As a consequence, the count rate is lower compared to the normal surfaces. This procedure makes it possible to identify the location of the tip with an accuracy of less than 2-3 μm .

A second method exploits the resistance change in the cantilever due to illumination with the laser as shown in Figure 4.14b. Two effects contribute to the resistance change; (i) laser-induced heating which can increase or decrease the resistance depending on the position in the resistance curve (see Figure 4.12) and (ii) photo-induced charge carriers which reduce the resistance. The gray background in Figure 4.14b represents the electrical resistance of the cantilever without external disturbance. In the bright areas, the resistance of the cantilever increased under laser illumination, which can be attributed to laser-induced heating. In the area of the *Writer* heater, which was powered during this scan, a laser-induced decrease in the resistance can be observed. This can be explained by the fact that photo-induced charge carrier excitation is the dominant effect in the low-doped silicon area, which reduces the resistance.¹²³ Therefore, it is possible to identify the location of the low-doped heater region. A comparison between the image obtained from the reflected light and the image obtained from the laser-induced resistance change reveals that the heater and the tip do not completely overlap.

4.4.6 Calculation of the Magnetic Field Produced by the MW Antenna

Knowledge of the magnetic field around the microwave antenna is of importance for optically-detected magnetic resonance experiments, because if the microwave magnetic field is too low, the $m_s = 0$ to $m_s = \pm 1$ spin transition is not efficient and hence only a small fluorescence contrast will be observed at the spin resonance. On the contrary, a very high microwave magnetic field leads to line broadening,²⁰⁷ which reduces the sensitivity (and can cause Joule heating in the microwave antenna).

Therefore, in the following section, the microwave magnetic field around the optical antennas used in this work is calculated. The magnetic field $d\vec{B}$ produced by an infinitesimal element $d\vec{l}$ of a cylindrical wire at a distance \vec{r} is described by the Biot-

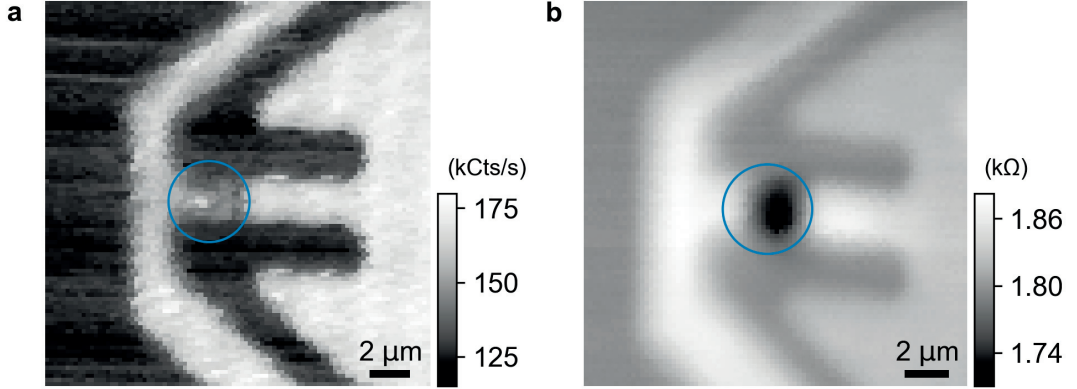


Figure 4.14 – Alignment of the cantilever with respect to the laser to locate the tip and the heater regions. **(a)** Imaging of the cantilever by measuring the reflected light from the cantilever with the photon counter. The blue circle indicates the region of the tip. **(b)** Imaging of the cantilever by measuring the laser induced resistance change of the *Writer* sensor, which is useful to determine the location of the heater. The blue circle indicates the heater region.

Savart law:

$$d\vec{B} = \frac{\mu_0}{4\pi} \frac{I d\vec{l} \times \vec{r}}{|\vec{r}|^3}, \quad (4.7)$$

where μ_0 is the magnetic permeability in vacuum and I is the current running through the wire. For an infinitely long cylindrical wire the magnetic field intensity can be calculated as:

$$\vec{B}(x, y) = \frac{\mu_0 I}{2\pi \sqrt{x^2 + y^2}} \hat{\varphi}, \quad (4.8)$$

where $\hat{\varphi}$ is the angular unit vector.

The strategy to numerically calculate the magnetic field distribution from a current in an arbitrarily-shaped, infinitely long wire is to subdivide it into smaller elements and superimpose the magnetic field vectors produced by each element calculated from Equation (4.8):

$$\vec{B}_{Wire}(x, y) = \sum_{x_0, y_0} \vec{B}(x - x_0, y - y_0) \quad \text{where } x_0, y_0 \in \text{Wire} \quad (4.9)$$

$$= \sum_{x_0, y_0} \frac{\mu_0 I}{2\pi} \frac{\hat{\varphi}}{\sqrt{(x - x_0)^2 + (y - y_0)^2}} \quad (4.10)$$

$$= \sum_{x_0, y_0} \frac{\mu_0 I}{2\pi} \frac{-\sin(\varphi)\hat{x} + \cos(\varphi)\hat{y}}{\sqrt{(x - x_0)^2 + (y - y_0)^2}} \quad \text{where } \varphi = \arctan\left(\frac{x - x_0}{y - y_0}\right) \quad (4.11)$$

$$= \sum_{x_0, y_0} \frac{\mu_0 I}{2\pi} \frac{(x - x_0)\hat{y} - (y - y_0)\hat{x}}{(x - x_0)^2 + (y - y_0)^2}. \quad (4.12)$$

The dimensions of the MW antenna for the samples used here are 280 μm wide and 250 nm thick. For the numerical calculation, the wire was subdivided into $50 \times 50 \text{ nm}^2$ sized elements.

Figure 4.15a shows the magnetic field distribution around the MW antenna on one corner of the gold stripe. A typical MW power of 631 mW was used which corresponds a current of 3.5 mA. It can be seen, that the magnetic field strength is largest around the corner of the wire and rapidly decays with increasing distance from the wire. The large magnetic field around the corner, but not around the entire wire is due to superposition of the magnetic field components, which cancel the magnetic field. In Figure 4.15b, the magnetic field strength is plotted as a function of horizontal distance from the wire for MW powers between 100 and 3981 mW. As expected, the magnetic field strength decreases inversely with the distance from the wire and increases with the square root of the MW power $\sqrt{P_{MW}}$.

4.4.7 Localization of Fluorescent Particles and Optically Detected Magnetic Resonance

In the following paragraph, a typical procedure is described to detect fluorescent diamond particles and take an ODMR spectrum of a specific particle. Figure 4.16a shows a scan of a glass slide near the edges of a 280 μm wide microwave antenna with $\sim 1 \mu\text{m}$ large diamond particles distributed nearby. The MW antenna can easily be detected due to an increase in the reflected light when the laser is scanned over the metallic area. After a large scan of $60 \times 60 \mu\text{m}^2$ at a pixel size of 500 nm, to obtain an overview of the particle distribution, a specific particle (labeled with a circle) is selected and a small scan at a higher resolution (100 nm pixel size) is performed as shown in Figure 4.16b. To perform ODMR experiments, the laser is focused at the center of the particle and the MW frequency is scanned between 2.80 and 2.94 GHz while the fluorescence intensity

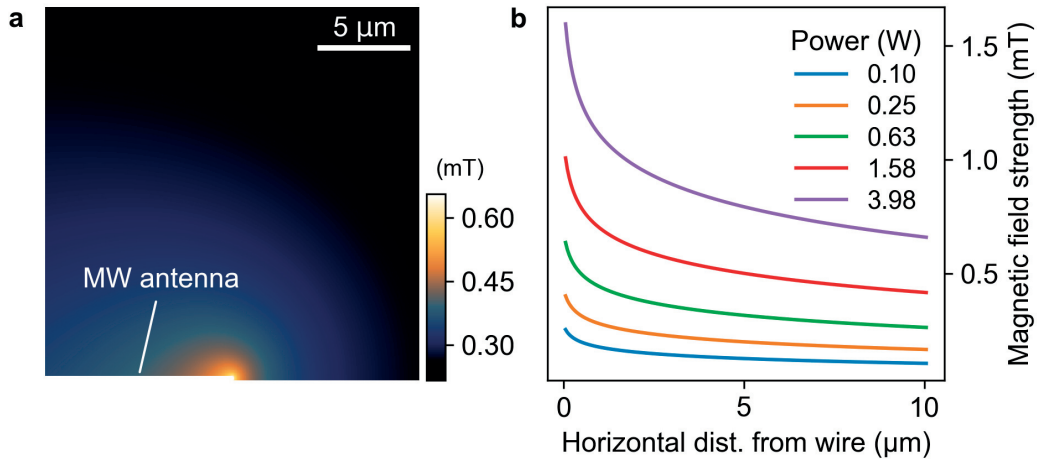


Figure 4.15 – Numerical calculation of the magnetic field distribution around the microwave antenna. **(a)** Magnetic field strength around one edge of an infinitely long, 280 μm wide and 250 nm thick gold film at a MW power of 36 mW. **(b)** The magnetic field strength is plotted for different microwave powers as a function of the lateral distance from the wire.

is recorded as shown in Figure 4.16c. The spectrum is then fitted with two Lorentzian curves as plotted in the graph to determine the ZFS.

From the graph in Figure 4.15b, the MW field at the diamond particle, which is located right at the corner of the antenna, can be estimated to be between 0.4-0.6 mT.

4.5 NV⁻ Center-Based Thermometry on Heated Probes

To demonstrate that nanoscale thermometry with the setup described in this work is possible, two thermometry experiments on heated probes are presented. Two sets of particles with an average diameter of 1 μm and 40 nm were used.

First measurements were made on a large particle due to a higher fluorescence signal and therefore better signal to noise ratio. The particle was attached to the cantilever by scanning the probe over a sample with randomly distributed particles. In Figure 4.17a, ODMR spectra are plotted at different dissipated cantilever powers ranging from 0.1 to 5 mW. The colored curves are the recorded data and the gray curves are the corresponding Lorentzian fit to the data. From the fit, the ZFS and the optical contrast are determined.

To determine the temperature of the particle from the ZFS parameter at different heating temperatures, the calibration curve from Toyli *et al.* was used (Figure 4.2a). In Figure 4.17b, the temperature is plotted against the dissipated power in the *Writer* heater of

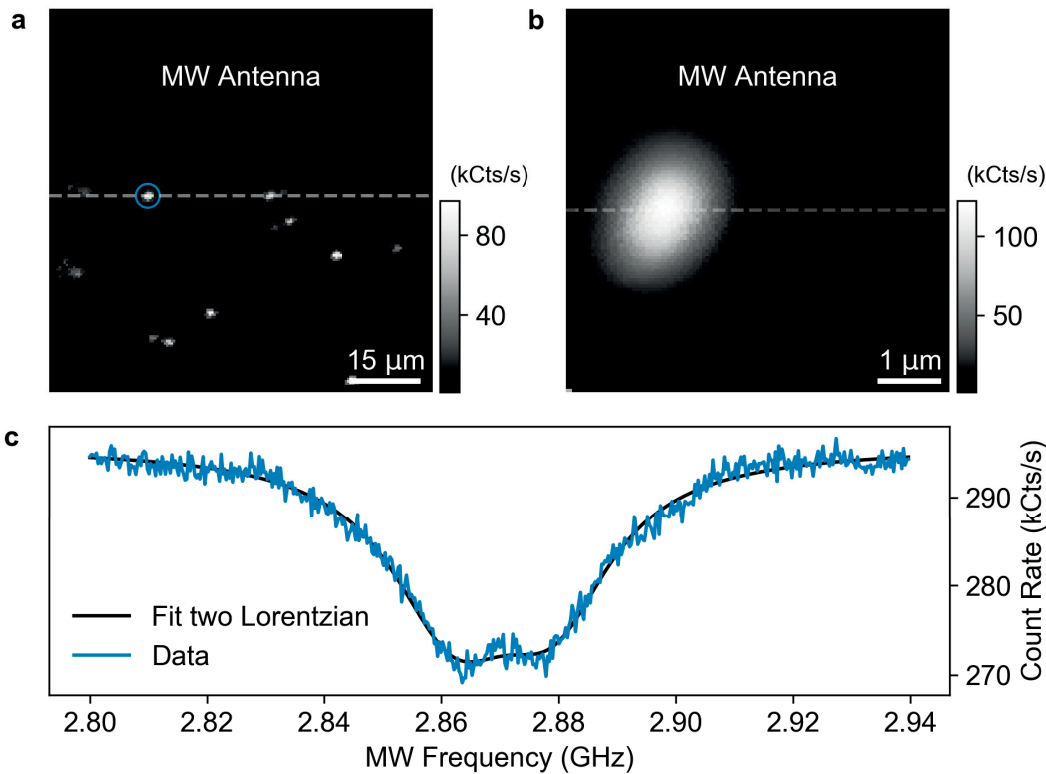


Figure 4.16 – Localization of fluorescent particles and ODMR of a specific particle. (a) Overview scan of $1\ \mu\text{m}$ large particles distributed nearby of the microwave antenna. The dashed line indicates the edge of the metal area. (b) Magnified scan of one particle. (c) Optically detected magnetic resonance spectrum of a selected particle and a fit with two Lorentzian (*black curve*).

the cantilever. The errorbar indicates the standard error from the Lorentzian fit. The temperature increases sublinearly with increasing heating power which is in contrast to the expected behavior as determined by Spieser *et al.*¹²⁴ The origin of the discrepancy is not clear but may be related to the size of the particle. In Section 4.1.1, it was discussed that the normalized fluorescence intensity could be used for thermometry. Therefore, in Figure 4.17c, the fluorescence intensity normalized with respect to the room temperature value is plotted against the heater temperature. Between room temperature and 400 K, the fluorescence intensity rapidly decreases and remains nearly constant up to 500 K which is in contrast to the reference data.¹³⁰ These results suggest that intensity-based thermometry is unsuitable for thermal probes. It is speculated that due to the bimorph bending of the cantilever with temperature, the fluorescence particle moves relative to the focus of the objective, which could explain the observed increase and also the large variation in between different data points. Furthermore, it was shown in the literature that the ODMR contrast decreases with increasing temperature for a single NV⁻ center.¹³⁰ In Figure 4.17c, the normalized amplitude of the ODMR contrast

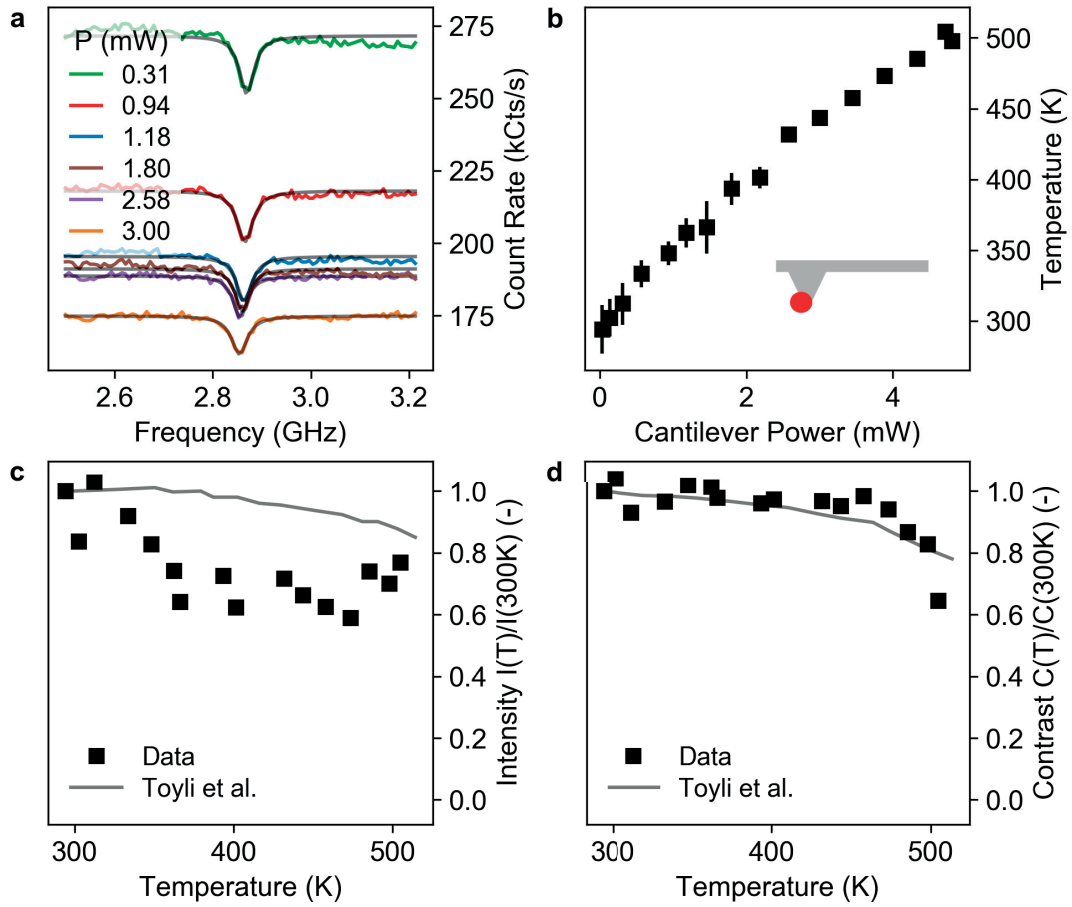


Figure 4.17 – NV⁻ center-based thermometry based on the ODMR signal. (a) The NV⁻ center emission from a $\sim 1 \mu\text{m}$ sized diamond particle attached to the heated tip is plotted against the MW frequency during an ODMR experiment at different heater temperatures. (b) The temperature obtained from the ZFS shift is plotted against the dissipated power in the cantilever. The errorbars indicate the standard error from fitting. (c) The normalized fluorescence intensity is plotted against the measured temperature. As a reference, the measurements from Toyli *et al.* are drawn.¹³⁰ (d) The normalized ODMR contrast is plotted against the measured temperature, again with measurements from Toyli *et al.* as a reference.

with respect to the contrast at room temperature is plotted against the temperature and shows good agreement with measurements from Toyli *et al.*

Particles with a diameter on the order of one micrometer are not suited for temperature measurements when taking into consideration that the tip is only 500 nm in height. In this measurements, the particles with an average diameter of 40 nm are picked up by the tip while scanning over a substrate coated with randomly distributed nanodiamonds. Multiple nanodiamonds are assumed to be attached to the tip during the scanning to

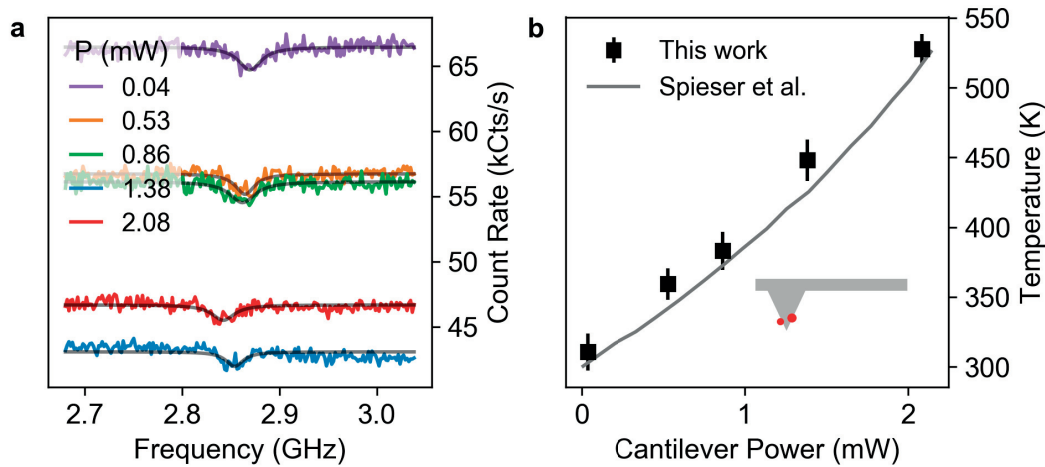


Figure 4.18 – NV^- center based thermometry with 40 nm particles. (a) The NV^- center emission from 40 nm-sized particles distributed around the heated tip is plotted against the MW frequency during an ODMR experiment at different heater temperatures. The laser power was modified between the curves to obtain sufficiently high count rates at high temperatures (b) The temperature obtained from the ZFS shift is plotted against the dissipated power in the cantilever. The errorbars indicate the standard error from the fitted curve. As a comparison, the experimental data from Raman thermometry by Spieser *et al.* on the same type of probes is shown.¹²⁴

obtain a fluorescence signal with a sufficiently large signal to noise ratio. Figure 4.18a shows the ODMR spectrum of the nanoparticles for a cantilever heating power from 0.04 to 2 mW when the tip was located 500 nm above the glass sample.

As expected, the count rate of the nanoparticles is smaller than for the microparticle, because fewer NV^- centers are contributing to the emission. As a consequence, the signal to noise ratio is smaller, which makes it more difficult to detect the ZFS. It should be noted that the count rate recorded for the 40 nm sized particles, which contain on average 12-14 NV^- centers, is smaller than the theoretical count rate of 200-500 kCts/s for a single NV^- center.²⁰³ A reduction in collection efficiency can be explained by the fact that the particles are on a tip that is positioned at a distance above the substrate, and hence the focusing of the objective through the coverslip is not optimal. Despite this, for multiple nanoparticles, the ODMR contrast is clearly measurable and can be fitted with a Lorentzian to read out the ZFS as shown by the gray curves.

In Figure 4.18b, the temperature obtained from the ZFS shift is plotted against the power dissipated in the cantilever. The tip temperature obtained from Raman thermometry in air¹²⁴ is plotted as a reference, which shows a good agreement with the ODMR measurements.

4.6 Conclusion

A thermometry setup was built to measure the temperature on thermal scanning probes by measuring the ODMR spectrum of NV^- centers in diamond nanoparticles attached to the probe tip. The setup is composed of a green laser to excite the NV^- centers and an inverted confocal microscope to focus the laser on the sample. The emitted fluorescence is detected by a single photon counting system. Multiple stages allow coarse and fine positioning of the optics, glass samples and the heated probe. Furthermore, the setup can record confocal fluorescence images and map the surface topography with the scanning probe. Different LabView software tools were developed that allow imaging, characterization of the cantilevers as well as thermometry measurements. First experiments have shown that ODMR-based thermometry on heated probes with the presented setup is feasible and are in agreement with results from the literature.

5 Conclusion and Outlook

In this work, two interesting materials have been investigated as resists for thermal scanning probe lithography (t-SPL), whereby patterning of both resists relies on fast heating and cooling rates on the order of 10^8 K/s. In addition a nanoscale thermometry setup was built that allows to perform temperature measurements on heated probes.

5.1 t-SPL on a Fluorescent Supramolecular Polymer

One investigated material is a thermochromic fluorescent supramolecular polymer, which exhibits a green fluorescent state at temperatures above 180 °C and a red fluorescent state at room temperature due to aggregation of excimer-forming moieties. In this work, it was shown that the high cooling rates in t-SPL make it possible to quench the green fluorescent state and create nano- to micrometer-sized structures with a fluorescent and topological contrast. By atomic force spectroscopy, it was found that the glass transition temperature of melt-casted films of the supramolecular polymer is 68 °C, which is in agreement with bulk films. Thermomechanical indentation was performed at temperatures ranging from 200 to 490 °C, indentation forces from 250 to 450 nN and time scales from 1 μ s to 1 ms. It was found that the temperature required to induce a surface modification of the material depends linearly on the indentation force and follows WLF-kinetics. For successful t-SPL patterning, the distance between consecutive indents is a crucial parameter due to displacement of molten material. In this work, reliably uniform patterns could be created at pitch sizes larger than 80 nm. By creating patterns below the optical diffraction limit, it was possible to control the fluorescence intensity of the green emission. A model that approximated the indents with semi-ellipsoids was able to explain the fluorescence intensity at pitch sizes from 20 to 500 nm. Another interesting feature is that multilevel structures can be created, where one pattern is visible by atomic force microscopy but not in optical microscopy. It was also demonstrated that indents created with the heated probe can be erased by local melting the supramolecular polymer under application of a small indentation force. Finally, a proof-of-concept study showed

that t-SPL on supramolecular polymers is not limited to rigid substrates such as silicon, but can also be applied on flexible substrates such as paper.

This novel coating material, combined with t-SPL, could be interesting for applications such as nano- to micrometer-scale anti-counterfeiting features in environments with temperatures not exceeding 180 °C with at least three degrees of security: fluorescence intensity, topography, and the concept of hidden features. Recent advances in laser-assisted and ultrafast nanoimprint lithography could be used to fabricate large-area patterns in UPy-OPV-UPy which can then be locally modified in a subsequent step with a heated probe to create highly customized features that are unique and difficult to reproduce. Furthermore, it is anticipated that this novel polymer has a broader application than thermal patterning such as in temperature and strain sensing.

5.2 Silk Fibroin as a Resist for t-SPL

The second material analyzed in this work is silk fibroin, a natural material with interesting optical and mechanical properties, such as a 80-90% transmission in the optical range and an elastic modulus between 16-20 GPa. By fast heating and cooling of annealed water-insoluble silk fibroin thin films with the heated probe, a solubility change was induced. While the origin of the contrast mechanism could not be fully determined, melting of beta-sheet crystallites, which make the silk fibroin water insoluble, or partial thermal degradation of the silk fibroin molecule are likely to be the driving mechanisms. Structures with a height of 30 nm at a pitch of 100 nm were created. A line edge roughness comparable to the size of silk fibroin molecules (~7 nm diameter) of 6.9 ± 1.8 nm and 9.3 ± 2.4 nm was measured in fast and slow scan directions, respectively. By simulation of the temperature distribution around a heated probe in silk fibroin, it was possible to identify the spreading of heat, besides the tip geometry, as a possible source of the low resolution. Thinner films could improve the spatial resolution due to stronger confinement of the heat around the tip apex. It was demonstrated that grayscale lithography of 50-200 nm deep patterns is possible with silk fibroin. Nanoscale patterns in silk fibroin have applications in optical sensing (photonic crystals) and silk fibroin has been demonstrated as a resist for pattern transfer into silicon oxide by a He/H₂/C₄F₈ dry-etching process. An etch rate of 160 ± 28 nm/min was found, which corresponds to a selectivity of 2.16 ± 0.08 with respect to silicon oxide.

Further experiments are required to bring clarification about the contrast formation of thermally modified silk fibroin. A proof-of-concept for a pattern transfer from silk into SiO₂ was shown but the process requires optimization to demonstrate a better performance. To extend the range of applications of silk fibroin as a resist beyond simple patterns and dry-etching, a lift-off process should be developed. Preliminary experiments with a dextran/silk double layer structure are promising. Dextran is water soluble but insoluble in ethanol. Therefore, the silk fibroin layer on the dextran can be annealed in

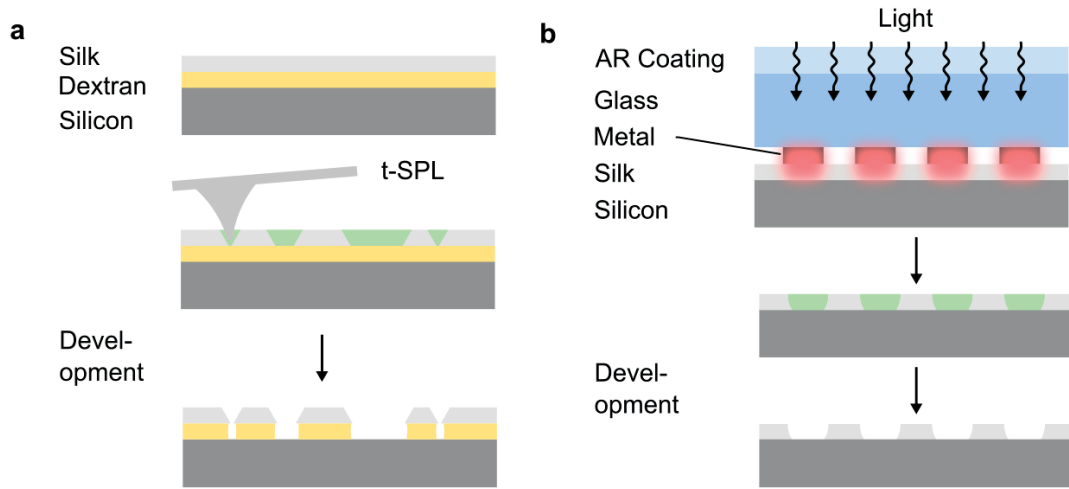


Figure 5.1 – Future experiments with silk fibroin. **(a)** Process flow of a lift-off process using silk fibroin and dextran **(b)** Process flow of thermal contact lithography with silk fibroin as a resist. A strong illumination source heats up a thin patterned metal layer due to absorption of the light. The silk fibroin below the metal is heated at short time scales and rendered water soluble. Subsequent development in water removes the thermally-treated silk fibroin.

ethanol. In a subsequent step, silk fibroin is patterned by t-SPL and immersed in water which removes the thermally exposed silk as well as the dextran below as depicted in Figure 5.1a. To reduce the dissolution rate of dextran during development, the water can be diluted with ethanol.

While t-SPL enables the creation of high-resolution structures, the technique is considerably slow for patterning large areas. To mitigate this disadvantage, mix-and-match lithography was proposed, where t-SPL is combined with a fast low-resolution patterning technique such as laser writing.²⁰⁸ Since silk fibroin has a low absorption in the visible range, laser heating is not efficient. Contact thermal lithography (CTL) can mitigate the problem by using an absorbing layer which heats up under optical illumination. In CTL, a mask is used that selectively absorbs light and converts it into heat, which diffuses away and heats up the material in contact as shown in 5.1b. The silk fibroin in contact with the absorber is locally exposed to heat and thermally modified similar to t-SPL. CTL was investigated in a previous publication using a photolithography mask with a chromium pattern and a commercial photolithography resist which crosslinks under exposure to heat.²⁰⁹

Patterned silk fibroin structures could be used in combination with t-SPL to fabricate 2.5D structures for cell capturing²¹⁰ or photonic applications where small and highly customized patterns with nanometer resolution are required.

5.3 Nanoscale Thermometry on Heated Probes Using NV⁻ Centers

In this work, a setup was designed, built and characterized to perform thermometry on heated atomic force microscopy tips by means of ODMR spectroscopy of NV⁻ centers. The setup is composed of a green laser for optical excitation of the NV⁻ electrons, an inverted confocal microscope to focus on the sample and a detection system that allows single photon counting. Multiple stages enable positioning of the sample and the cantilever with respect to each other as well as fluorescence imaging and surface metrology. So far, it was possible to contact micro- and nanoparticles with thermal probes and measure the temperature as a function of the dissipated power in the resistive heater. The measurements with nanoparticles are in agreement with Raman thermometry measurements in literature.

Nanoparticles are versatile sensors, since they can be placed in different locations. However, picking up nanoparticles with the probe is not a reproducible process. Hence, one could imagine to create diamond probes with one or multiple implanted NV⁻ centers at the tip apex for sensing. It would then be possible to measure the temperature of the probe while in contact with a material or enable differential-scanning calorimetry in applications such as for material analysis.

A longterm goal to optimize the signal collection would be to integrate the optics into the cantilever to reduce the losses via the detection path of the fluorescence microscope. Multifunctional probes with an integrated magnetic and thermal sensor would make it possible to create and measure reconfigurable metamaterials with finely tuned magnetic properties⁷⁷ and perform thermal analysis of materials at the nanometer scale. The pressure sensitivity of the NV center (10-15 MHz/GPa)²¹¹ would also be suitable to measuring forces during indentation with the heated probe.

A Appendix

A.1 Effect of Thermal Spreading and Tip Shape on Resolution

The tip shape and heat diffusion significantly affects the resolution and the aspect ratio of t-SPL patterns. Figure A.1 illustrates factors that can reduce the spatial resolution of a tip. In Figure A.1a, an ideal tip with an infinitively sharp tip apex and a typical opening angle of 30° is depicted. From geometrical considerations, the pattern height and pitch size can be determined. However, at the nanometer scale, the spreading of heat around the thermal probe can considerably increase the volume that is thermally modified due to diffusion of heat around the probe. As a consequence, it is desired to have the lowest possible temperature at the apex to induce the desired change in the material. Figure A.1c shows a more realistic illustration of a thermal probe. In addition to a finite tip apex radius, contaminations can reduce the lateral resolution of the probe and reduce the aspect ratio of a pattern.

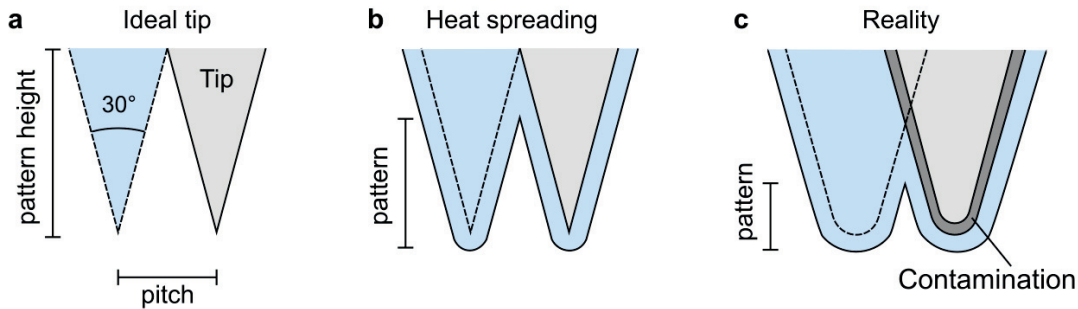


Figure A.1 – Influence of thermal spreading and tip shape on patterning resolution. (a) An ideal tip would be infinitely sharp to create a high aspect ratio indent. (b) Spreading of heat from the tip can reduce the lateral resolution and decrease the aspect ratio of the indents. (c) Illustration of a more realistic tip with contamination on the surface and a finite tip apex radius. These factors can considerably reduce the aspect ratio of the smallest achievable structures.

A.2 Script for Rim Detection

The following script was used to locate the edge of a surface topography structure and determine the location of the highest peaks of the rim along the edge. From the location of the peaks, the height of the rim is computed. The script was tested with Python 3.5.3.

Listing A.1 – "rimheight.py"

```

1  #!/usr/bin/env python3
3  """
4  Copyright (c) (2018) Samuel Zimmermann <samuel.zimmermann@protonmail.com>
5
6  This program is free software: you can redistribute it and/or modify
7  it under the terms of the GNU General Public License as published by
8  the Free Software Foundation, either version 3 of the License, or
9  (at your option) any later version.
10
11 This program is distributed in the hope that it will be useful,
12 but WITHOUT ANY WARRANTY; without even the implied warranty of
13 MERCHANTABILITY or FITNESS FOR A PARTICULAR PURPOSE. See the
14 GNU General Public License for more details.
15
16 You should have received a copy of the GNU General Public License
17 along with this program. If not, see <https://www.gnu.org/licenses/>.
18 """
19
20 import matplotlib.pyplot as plt
21 import numpy as np
22
23 # ----- functions -----

```

A.2. Script for Rim Detection

```
25 def get_max_on_line(img, dist_from_line):
    """
27     Find maximum across 0 axis of img
    assuming that the maxima lay on a horizontal straight line
29     Find only the coordinates of maxima which are
    closer than a certain with from the linear fit
31
    Input:
33     img -- 2d numpy array
    dist_from_line -- width how far maxima can be from the straight
    line
35
    Returns:
37     maxima -- 1d numpy array with values of maxima
    maxarg -- 1d numpy array with y coordinate of the maxima
39     fit1d -- numpy.fit1d object
    """
41     argmax = np.argmax(img, axis=0)
    xrange = np.arange(len(argmax))
43     fit = np.polyfit(xrange, argmax, deg =1)
    fit1d = np.poly1d(fit)
45
    maxima = np.zeros(xrange.shape)
47     maxarg = maxima.copy()
49
    for x in xrange:
        y = fit1d(x)
51     maxima[x] = max(img[int(y-dist_from_line/2):int(y+dist_from_line
    /2),x])
        maxarg[x] = img[int(y-dist_from_line/2):int(y+dist_from_line/2),x
    ].argmax()+int(y-dist_from_line/2)
53     return maxima, maxarg
55
# ----- script -----
57
# example data: tilted plane with trench
59 plane = lambda x, y: ((y.max()-y)*50+(x.max()-x)**2)/(x.max()**2+y.max())
    *10
    X, Y = np.mgrid[0:100, 0:100]
61 data = np.random.random((100,100))*plane(X,Y)
    data[:50,:] = np.random.random((50,100))
63
# plot sample data
65 plt.imshow(data)
    plt.show()
67
# compute maximum
69 dist_from_line = 5
    maxima, maxarg = get_max_on_line(data, dist_from_line)
71
# plot maximum
```

```
73 plt.plot(maxima)
    plt.xlabel('position')
75 plt.ylabel('height')
    plt.show()
```

A.3 Script to Compute the Line Edge Roughness

This script was used to compute the line edge roughness of a surface topography with horizontal structures. The script can easily be modified to detect vertical lines. The script was tested with Python 3.5.3.

Listing A.2 – `computeler.py` a script to compute the line edge roughness from horizontal structures

```
#!/usr/bin/env python3
2
"""
4 Copyright (c) (2018) Samuel Zimmermann <samuel.zimmermann@protonmail.com>

6 This program is free software: you can redistribute it and/or modify
it under the terms of the GNU General Public License as published by
8 the Free Software Foundation, either version 3 of the License, or
(at your option) any later version.

10 This program is distributed in the hope that it will be useful,
12 but WITHOUT ANY WARRANTY; without even the implied warranty of
MERCHANTABILITY or FITNESS FOR A PARTICULAR PURPOSE. See the
14 GNU General Public License for more details.

16 You should have received a copy of the GNU General Public License
along with this program. If not, see <https://www.gnu.org/licenses/>.
18 """

20 from skimage import measure
from skimage.filters import threshold_otsu
22 import numpy as np
import matplotlib.pyplot as plt
24
# sample data
26 X, Y = np.mgrid[0:100, 0:100]
field = np.sin(X/10*np.pi)*4+np.random.randn(100, 100)
28
# show sample data
30 plt.imshow(field)

32 # Pixelsize
px_size = 1e-8
34
# Otsu Threshold
36 thres = threshold_otsu(field)
```

A.4. Script to Simulate Temperature Distribution around the Tip

```
contours = measure.find_contours(field, thres)
38
# Output
40 lers = []

42 # Compute contours
for contour in contours:
44
    # unpack contours
46     x = contour[:,1]
    y = contour[:,0]
48
    # Fit linear curve
50     fit = np.polyfit(x, y, deg=1)
    fitn = np.poly1d(fit)
52
    # LER
54     ler = np.sqrt(np.sum(((y-fitn(x))*px_size)**2/len(y)))
    lers.append(ler)
56
    # plot red contour of the line edge
58     plt.plot(x,y,'r')

60 # plot
plt.show()
62
# print line edge roughness
64 print(u'LER (3sigma): {:.1f}({:.1f}) nm'.format(3*np.mean(lers)*1e9, 3*np
    .std(lers)*1e9))
```

A.4 Script to Simulate Temperature Distribution around the Tip

The temperature distribution around the tip was simulated using FEniCS (1:2016.2) with Python 2.7.13 on Debian 9.6. In addition, Gmsh 2.25 is required to create the mesh.

The script to simulate the temperature distribution `tip-indent.py` around a tip apex in contact with silk fibroin includes two modules: `fenicshelper.py` and `geohelp.py`. Furthermore, a template `tip-indent-tmpl.geo` to create the mesh is used to facilitate modifications in the geometry of the tip and sample.

Listing A.3 – `tip-indent.py` A script to simulate the heat distribution of a heated tip in a material using the finite element modelling software *FEniCS*

```
#!/usr/bin/env python2
2
"""
4 Copyright (c) (2018) Samuel Zimmermann <samuel.zimmermann@protonmail.com>
```

Appendix A. Appendix

```
6 This program is free software: you can redistribute it and/or modify
  it under the terms of the GNU General Public License as published by
8 the Free Software Foundation, either version 3 of the License, or
  (at your option) any later version.
10
  This program is distributed in the hope that it will be useful,
12 but WITHOUT ANY WARRANTY; without even the implied warranty of
  MERCHANTABILITY or FITNESS FOR A PARTICULAR PURPOSE. See the
14 GNU General Public License for more details.
16
  You should have received a copy of the GNU General Public License
  along with this program. If not, see <https://www.gnu.org/licenses/>.
18 """
20 import fenics as fn
  import fenicshelper as fh
22
  # ----- parameters -----
24
  mesh_name = 'tip-indent' # path to the mesh file without extension
26 gmsh_cmd = '-3' # gmsh command
28 # mesh parameters
  mesh_params = {'angle': 15,
30                 'height': 5e-8,
                 'width': 2e-6,
32                 'thickness': 350e-9,
                 'hdmsH': 0.5e-9,
34                 'ldmsH': 0.5e-7,
                 'depth': 2e-6
36                }
38 # lookup region to number in mesh
  regions = {
40     'heater': 1,
     'mirror': 2,
42     'heat sink': 3,
     'air': 4,
44     'body': 5
  }
46
  # simulation parameters
48 u0 = 298 # heat sink temperature and initial condition
      (K)
  uh = 676 # heater temperature (K)
50 T = 6e-6 # simulation time
  n_timesteps = 2 # number of time steps
52 dt = T / n_timesteps # time step size
  diff_thermal = 1.6e-7 # thermal diffusivity of silk fibroin(m2/s)
54
  # Create Files
56 vtkfile = fn.File('tip-indent.pvd')
```


A.4. Script to Simulate Temperature Distribution around the Tip

```
58 # ----- script -----
60 # Create and load mesh
    fh.create_mesh(mesh_name, mesh_params, gmsh_cmd, update=True)
62 mesh, pr, fr = fh.load_mesh(mesh_name)

64 # Function space
    V = fn.FunctionSpace(mesh, 'P', 1)
66
    # Integration elements
68 dx = fn.Measure('dx', subdomain_data = pr)

70 # Material constants
    alpha = fn.Constant(diff_thermal) # Thermal diffusivity
72
    # Boundary conditions
74 bcs = [
        fn.DirichletBC(V, uh, fr, regions['heater']),
76         fn.DirichletBC(V, u0, fr, regions['heat sink'])
    ]
78
    # Initial conditions
80 u_n = fn.interpolate(fn.Constant(u0), V)

82 # Variational problem
    u = fn.TrialFunction(V)
84 v = fn.TestFunction(V)

86 # left and right
    a = v*u*dx + alpha*dt*fn.dot(fn.grad(v),fn.grad(u))*dx
88 L = v*u_n*dx

90 # Time-stepping
    u = fn.Function(V)
92 t = 0

94 # loop time steps
    for n in range(n_timesteps):
96
        # Update current time
98         t += dt

100        # Compute solution
        fn.solve(a == L, u, bcs)
102
        # Store solution
104         vtkfile << (u, t)

106        # Update previous solution
        u_n.assign(u)
108
```

Appendix A. Appendix

```
print('{:d}/{:d}'.format(n, n_timesteps))
```

Listing A.4 – `fenicshelper.py` A module with various helper functions *FEniCS*

```
1  #!/usr/bin/env python2
2  # -*- coding: utf-8 -*-
3  """
4  Created on Thu Aug  2 17:33:15 2018
5
6  @author: samuel
7  """
8
9  def convert_geo_to_msh(fname, options):
10     """
11     Renders a gmsh script into a msh file
12
13     Note: works unfortunately not under IPython with python 2.7.13
14
15     Input:
16         fname: Filename without extension
17         options: Options for gmsh, e.g. "-2" for 2d mesh or "-3" for 3d
18         mesh
19
20     Output:
21         0 if successful, 1 if it failed
22
23     Example:
24         >>> convert_geo_to_msh('filename', '-2')
25         0
26     """
27     from subprocess import call, Popen
28
29     interpreter = 'gmsh'
30     options = str(options)
31     fname_in = fname + '.geo'
32
33     p = call([interpreter, options, fname_in])
34
35     print('Works not under ipython console')
36
37     if p == 0:
38         print('Sucessfully converted {:s}'.format(fname_in))
39     else:
40         print('Failed to convert {:s} using gmsh'.format(fname_in))
41
42     return p
43
44 def convert_msh_to_xml(fname):
45     """
46     Convert a mesh file into a xml file using dolfin-convert
47 """
```

A.4. Script to Simulate Temperature Distribution around the Tip

```
Input:
49     fname: Filename without extension

Output:
51     0 if successful, 1 if it failed
53
Example:
55     >>> convert_msh_to_xml('filename')
56     0
57     """
from subprocess import call, Popen
59
interpreter = 'dolfin-convert'
61
fname_in = fname + '.msh'
63 fname_out = fname + '.xml'

65 p = call([interpreter, fname_in, fname_out])

67 if p == 0:
    print('Successfully converted {:s} to {:s}'.format(fname_in,
fname_out))
69 else:
    print('Failed to convert {:s} to {:s} using dolfin-convert'.
format(fname_in, fname_out))
71
return p
73

75 #Todo implement mesh_dim, add save_geo_str to line 91 and put a sleep in
between
def create_mesh(fname, mesh_params, gmsh_cmd, update=False):
77     """Create the mesh from a .geo file into .xml format for fenics
Update only if .xml file does not exist or update is True
79
Input:
81     fname: filename without extension
opt_gmsh: options for gmsh
83     update: if true, the mesh is updated even if the files already
exist

85     Output:
0
87
Example:
89     >>>create_mesh('filename', '-2')
0
91     """
from os.path import isfile
93 from geohelp import save_geo_str
from time import sleep
95
```

Appendix A. Appendix

```
    if update == True:
97
        # Save the geo file
99        save_geo_str(fname, **mesh_params)
        sleep(2)
101
        # Convert geo -> msh -> xml
103        convert_geo_to_msh(fname, gmsh_cmd)
        convert_msh_to_xml(fname)
105        sleep(2)
107
    elif isfile(fname+'.xml') == False:
109
        create_mesh(fname, mesh_params, gmsh_cmd, update=True)
111
    else:
113
        print('Mesh was not updated.')
115
    return 0
117

119 def load_mesh(fname):
    """
121    Load a mesh, physical and facet region
123
    Input:
        fname: filename of the mesh without extension
125
    Output:
127        mesh:
            cd: information about interior regions
129            fd: information about boundaries
131
    Example:
        >>>mesh, cd, fd = load_mesh('filename')
133    """
    from fenics import Mesh, MeshFunction
135
    mesh = Mesh(fname+'.xml')
137    cd = MeshFunction('size_t', mesh, fname+'_physical_region.xml')
    fd = MeshFunction('size_t', mesh, fname+'_facet_region.xml')
139
    return mesh, cd, fd
141

143 def pv_csv_import(fname, n_files):
145
    import numpy as np
147
    for i in range(n_files):
```

A.4. Script to Simulate Temperature Distribution around the Tip

```
149     data = np.genfromtxt(fname+str(i)+'.csv', skip_header=1,
150                          delimiter=',', unpack=True)
151
152     if i == 0:
153         container = np.zeros((n_files, data.shape[1]))
154         container[i] = data[0]
155
156     container[i+1] = data[1]
157
158     return container
```

Listing A.5 – `geohelp.py` A module with helper functions to render a `.geo` template file into a `.mesh`.

```
1 #!/usr/bin/env python2
2 # -*- coding: utf-8 -*-
3 """
4 Created on Sun Aug  5 21:37:45 2018
5
6 @author: samuel
7 """
8
9 def replace_in_file(string, kwdict):
10     """
11     Replaces placeholders of the form '{placeholder}' with dict values of
12     the form {'placeholder': value}
13
14     Input:
15     string containing placeholders of the form {placeholder}
16     dict with key, value pairs of the form {'placeholder': value}
17
18     Output:
19     formatted string with replaced placeholders
20
21     Example:
22     >>>string = 'hello {people}'
23     >>>strformatted = replace_in_file(string, {'people': 'world'})
24     'hello world'
25     """
26
27     import re
28
29     for key, value in zip(kwdict.keys(), kwdict.values()):
30         string = re.sub('{{{:s}}}'.format(key), str(value), string)
31     return string
32
33 def save_geo_str(filename, **kwargs):
34     """
35     Saves a .geo file from a string formattable string under filename.geo
36     .
37     """
```

Appendix A. Appendix

```
Input:
37     arguments for string format

Output:
39     0
41

Example:
43
    >>>string = 'h = DefineNumber[ {height}, Name "Parameters/Indent
height" ]';
45     >>>save_geo_str('default', string, height=1e-6)
    'h = DefineNumber[ {1e-6}, Name "Parameters/Indent height" ]';
47
    """
49     from time import sleep
    print('Use mesh parameters:')
51     print(kwargs)

53     with open(filename+'-tmpl.geo', 'r') as f:
        string = f.read()
55
57     with open(filename+'.geo', 'w') as f:
        strformat = replace_in_file(string, kwargs)
59         f.write(strformat)

61     print()
    print('Created geo file:')
63     print(strformat)

65     sleep(3)

67     return 0
```

Listing A.6 – tip-indent-tmpl.geo A template file to create the geometry file for *Gmsh*.

```
1 angle = DefineNumber[ {angle}, Name "Parameters/Tip angle" ];
h = DefineNumber[ {height}, Name "Parameters/Indent height" ];
3 w = DefineNumber[ {width}, Name "Parameters/Substrate width" ];
t = DefineNumber[ {thickness}, Name "Parameters/Polymer thickness" ];
5 hdmsH = DefineNumber[ {hdmsH}, Name "Parameters/High mesh density" ];
ldmsH = DefineNumber[ {ldmsH}, Name "Parameters/Low mesh density" ];
7 r = DefineNumber[ Tan( angle/180*Pi )*h, Name "Parameters/Indent radius"
];
d = DefineNumber[ {depth}, Name "Parameters/Substrate depth" ];
9
Point(1) = {r, 0, 0, hdmsH};
11 Point(2) = {w, 0, 0, ldmsH};
Point(3) = {w, 0, -t, ldmsH};
13 Point(4) = {0, 0, -t, ldmsH};
Point(5) = {0, 0, -h, hdmsH};
15 Point(6) = {w, d, 0, ldmsH};
```

A.4. Script to Simulate Temperature Distribution around the Tip

```
Point(7) = {w, d, -t, ldmsh};
17 Point(8) = {0, d, 0, ldmsh};
   Point(9) = {0, d, -t, ldmsh};
19 Point(10) = {0, r, 0, hdmsH};

21 // Front surface
   Line(1) = {1, 5};
23 Line(2) = {2, 1};
   Line(3) = {3, 2};
25 Line(4) = {4, 3};
   Line(5) = {5, 4};
27 Line Loop(6) = {5, 4, 3, 2, 1};
   Plane Surface(22) = {6};
29

   // Tip surface 9
31 surfVect[] = Extrude {{0, 0, 1}, {0, 0, 0}, Pi/2} {
   Line{1};
33 }; // Axis direction, coordinate of an axis point, angle in radians

35 Characteristic Length {1, 5, 10, 23, 24} = hdmsH;

37 // Left surface
   // Line 24 top from extrusion
39 // Line 23 corresponding to 1 from extrusion
   Line(9) = {10, 8};
41 Line(10) = {8, 9};
   Line(11) = {9, 4};
43 Line Loop(12) = {-23, 9, 10, 11, -5};
   Plane Surface(23) = {12};
45

   // Back surface
47 Line(13) = {8, 6};
   Line(14) = {6, 7};
49 Line(15) = {7, 9};
   Line Loop(16) = {13, 14, 15, -10};
51 Plane Surface(24) = {16};

53 // Right surface
   Line(17) = {6, 2};
55 Line(18) = {3, 7};
   Line Loop(19) = {17, -3, 18, -14};
57 Plane Surface(26) = {19};

59 // Top surface
   Line Loop(20) = {-2, -17, -13, -9, -24};
61 Plane Surface(27) = {20};

63 // Bottom surface
   Line Loop(21) = {-4, -18, -15, -11};
65 Plane Surface(28) = {21};

67 // Volume
```

Appendix A. Appendix

```
Surface Loop(29) = {27, 22, 23, 25, 24, 26, 28};
69 Volume(30) = {29};

71
// Physical Groups
73 Physical Surface("heater") = {25};
Physical Surface("mirror") = {23, 6};
75 Physical Surface("heat sink") = {28, 26, 24};
Physical Surface("air") = {27};
77 Physical Volume("body") = {30};
```

A.5 Script to Compute the Magnetic Field from a Wire

Listing A.7 – "magneticfieldwire.py"

```
1  #!/usr/bin/env python3

3  """
Copyright (c) (2018) Samuel Zimmermann <samuel.zimmermann@protonmail.com>
5
This program is free software: you can redistribute it and/or modify
7 it under the terms of the GNU General Public License as published by
the Free Software Foundation, either version 3 of the License, or
9 (at your option) any later version.

11 This program is distributed in the hope that it will be useful,
but WITHOUT ANY WARRANTY; without even the implied warranty of
13 MERCHANTABILITY or FITNESS FOR A PARTICULAR PURPOSE. See the
GNU General Public License for more details.

15
You should have received a copy of the GNU General Public License
17 along with this program. If not, see <https://www.gnu.org/licenses/>.
"""

19
import matplotlib.pyplot as plt
21 import numpy as np

23 # ----- functions -----

25 def biot_savart(x0, y0, x, y, I):
    """
27     2D Magnetic field created in point x,y by a wire located at x0,y0
    expanding infinitely in z direction

29     Keyword arguments:
        x0 -- x position of the wire (float)
31         y0 -- y position of the wire (float)
        x -- x position where the field is created (array)
33         y -- y position where the field is created (array)
        I -- current
```


A.5. Script to Compute the Magnetic Field from a Wire

```
35
Return:
37     Bx -- Magnetic field vector x component (array)
     By -- Magnetic field vector y component (array)
39     """
mu0 = 4 * np.pi * 1e-7
41 magB = mu0 / (2 * np.pi) * I / ((x-x0)**2 + (y-y0)**2)
bx = magB * -(y-y0)
43 by = magB * (x-x0)
return bx, by
45
def superimpose_b_field(fieldWidth,fieldHeight,wireWidth,wireHeight,dx,I)
:
47     """
Superimpose magnetic field for a field of fieldWidth x fieldHeight in
size
49 with a wire of size wireWidth x wireHeight

51 Keyword arguments:
     fieldWidth -- width of the field
53     fieldHeight -- height of the field
     wireWidth -- width of the metal wire
55     wireheight -- height of the metal wire

57 Return:
     Bx -- Magnetic field vector x component (array)
59     By -- Magnetic field vector y component (array)
     X -- X position array
61     Y -- Y position array
     """
63     # meshgrid (m)
X, Y = np.meshgrid(np.arange(0, fieldWidth, dx),np.arange(0,
fieldHeight, dx))
65
     # magnetic vector field init
67     Bx = np.zeros(X.shape)
     By = np.zeros(Y.shape)
69
     # position of the metal wire
71     Xw = np.arange(fieldWidth/2-wireWidth/2,fieldWidth/2+wireWidth/2,dx)
     Yw = np.arange(fieldHeight/2-wireHeight/2,fieldHeight/2+wireHeight/2,
dx)
73
     # current density
75     i = I / (wireWidth * wireHeight) * dx ** 2

77     # loop over wire positions
for y0 in Yw:
79         for x0 in Xw:
             bx, by = biot_savart(x0,y0,X,Y,i)
81
             # superposition
```

Appendix A. Appendix

```
83         Bx += bx
84         By += by
85
86         # exclude wire area
87         Bx[int(y0//dx), int(x0//dx)] = np.nan
88         By[int(y0//dx), int(x0//dx)] = np.nan
89
90     return Bx, By, X, Y
91
92     # ----- script -----
93
94     # Field size (m)
95     fieldWidth = 20e-6
96     fieldHeight = 20e-6
97
98     # discretization (m)
99     dx = 50e-9
100
101     # Wire dimensions (m)
102     wireWidth = 1e-6
103     wireHeight = 250e-9
104
105     # Current (A)
106     I = 0.1
107
108     # compute magnetic field
109     Bx, By, X, Y = superimpose_b_field(fieldWidth, fieldHeight, wireWidth,
110                                       wireHeight, dx, I)
111     B = np.hypot(Bx, By)
112
113     # ----- plotting -----
114
115     plt.imshow(B)
116     plt.show()
```

Bibliography

- (1) Garcia, R.; Knoll, A. W.; Riedo, E. *Nature Nanotechnology* **2014**, *9*, 577–587.
- (2) Moore, S. K. EUV Lithography Finally Ready for Chip Manufacturing., online, 2018.
- (3) Tennant, D. M. In *Nanotechnology*, Timp, G., Ed.; Springer New York: New York, NY, 1999, pp 161–205.
- (4) Mack, C. Tennant’s Law., http://www.lithoguru.com/scientist/essays/Tennants_Law.html.
- (5) Verschuuren, M. A.; Megens, M.; Ni, Y.; van Sprang, H.; Polman, A. *Advanced Optical Technologies* **2017**, *6*, 243–264.
- (6) Brunner, T. A. *Journal of Vacuum Science & Technology B: Microelectronics and Nanometer Structures Processing, Measurement, and Phenomena* **2003**, *21*, 2632–2637.
- (7) Rawlings, C.; Wolf, H.; Hedrick, J. L.; Coady, D. J.; Duerig, U.; Knoll, A. W. *ACS Nano* **2015**, *9*, 6188–6195.
- (8) Binnig, G. K.; Cherubini, G.; Despont, M.; Dürig, U. T.; Eleftheriou, E.; Pozidis, H.; Vettiger, P. In *Springer Handbook of Nanotechnology*, Bhushan, P. B., Ed.; Springer Berlin Heidelberg: 2010, pp 1601–1632.
- (9) Somnath, S.; Kim, H. J.; Hu, H.; King, W. P. *Nanotechnology* **2014**, *25*, 014001.
- (10) Martínez, R. V.; Losilla, N. S.; Martinez, J.; Huttel, Y.; Garcia, R. *Nano Letters* **2007**, *7*, 1846–1850.
- (11) Sheehan, P. E.; Whitman, L. J.; King, W. P.; Nelson, B. A. *Applied Physics Letters* **2004**, *85*, 1589–1591.
- (12) Nelson, B. A.; King, W. P.; Laracuentе, A. R.; Sheehan, P. E.; Whitman, L. J. *Applied Physics Letters* **2006**, *88*, 033104.
- (13) Lee, W. K.; Dai, Z.; King, W. P.; Sheehan, P. E. *Nano Letters* **2010**, *10*, 129–133.
- (14) Tseng, A. A.; Notargiacomo, A.; Chen, T. P. *Journal of Vacuum Science & Technology B: Microelectronics and Nanometer Structures Processing, Measurement, and Phenomena* **2005**, *23*, 877–894.

Bibliography

- (15) Mamin, H. J.; Rugar, D. *Applied Physics Letters* **1992**, *61*, 1003–1005.
- (16) Chui, B. W.; Stowe, T. D.; Kenny, T. W.; Mamin, H. J.; Terris, B. D.; Rugar, D. *Applied Physics Letters* **1996**, *69*, 2767–2769.
- (17) Mamin, H. J. *Applied Physics Letters* **1996**, *69*, 433–435.
- (18) Lutwyche, M.; Andreoli, C.; Binnig, G.; Brugger, J.; Drechsler, U.; Häberle, W.; Rohrer, H.; Rothuizen, H.; Vettiger, P.; Yaralioglu, G.; Quate, C. *Sensors and Actuators A: Physical* **1999**, *73*, 89–94.
- (19) IBM Research, Zürich Millipede small-scale MEMS prototype shown at CeBIT., <https://www.zurich.ibm.com/news/05/millipede.html>.
- (20) Pires, D.; Hedrick, J. L.; Silva, A. D.; Frommer, J.; Gotsmann, B.; Wolf, H.; Despont, M.; Duerig, U.; Knoll, A. W. *Science* **2010**, *328*, 732–735.
- (21) Coulembier, O.; Knoll, A.; Pires, D.; Gotsmann, B.; Duerig, U.; Frommer, J.; Miller, R. D.; Dubois, P.; Hedrick, J. L. *Macromolecules* **2010**, *43*, 572–574.
- (22) Knoll, A. W.; Pires, D.; Coulembier, O.; Dubois, P.; Hedrick, J. L.; Frommer, J.; Duerig, U. *Advanced Materials* **2010**, *22*, 3361–3365.
- (23) Ito, H.; Willson, C. G. *Polymer Engineering & Science* **1983**, *23*, 1012–1018.
- (24) Carroll, K. M.; Lu, X.; Kim, S.; Gao, Y.; Kim, H.-J.; Somnath, S.; Polloni, L.; Sordan, R.; King, W. P.; Curtis, J. E.; Riedo, E. *Nanoscale* **2014**, *6*, 1299–1304.
- (25) Wang, D.; Kodali, V. K.; Ii, W. D. U.; Jarvholm, J. E.; Okada, T.; Jones, S. C.; Rumi, M.; Dai, Z.; King, W. P.; Marder, S. R.; Curtis, J. E.; Riedo, E. *Advanced Functional Materials* **2009**, *19*, 3696–3702.
- (26) Choi, Y.-S.; Wu, X.; Lee, D.-W. *Review of Scientific Instruments* **2014**, *85*, 045002.
- (27) Fenwick, O.; Bozec, L.; Credgington, D.; Hammiche, A.; Lazzarini, G. M.; Silberberg, Y. R.; Cacialli, F. *Nature Nanotechnology* **2009**, *4*, 664–668.
- (28) Hua, Y. Materials and Methods for Nanolithography using Scanning Thermal Cantilever Probes., Ph.D. Thesis, Georgia Institute of Technology, 2008.
- (29) Gotsmann, B.; Rothuizen, H.; Duerig, U. *Applied Physics Letters* **2008**, *93*, 093116.
- (30) Nelson, B. A.; King, W. P. *Review of Scientific Instruments* **2007**, *78*, 023702.
- (31) Knoll, A.; Wiesmann, D.; Gotsmann, B.; Duerig, U. *Physical Review Letters* **2009**, *102*, 117801.
- (32) Kaule, T.; Zhang, Y.; Emmerling, S.; Pihan, S.; Foerch, R.; Gutmann, J.; Butt, H.-J.; Berger, R.; Duerig, U.; Knoll, A. W. *ACS Nano* **2013**, *7*, 748–759.
- (33) Wiesmann, D.; Rawlings, C.; Vecchione, R.; Porro, F.; Gotsmann, B.; Knoll, A.; Pires, D.; Duerig, U. *Nano Letters* **2009**, *9*, 3171–3176.

-
- (34) Gotsmann, B.; Knoll, A. W.; Pratt, R.; Frommer, J.; Hedrick, J. L.; Duerig, U. *Advanced Functional Materials* **2010**, *20*, 1276–1284.
- (35) Basu, A. S.; McNamara, S.; Gianchandani, Y. B. *Journal of Vacuum Science & Technology B: Microelectronics and Nanometer Structures Processing, Measurement, and Phenomena* **2004**, *22*, 3217–3220.
- (36) Gotsmann, B.; Duerig, U.; Frommer, J.; Hawker, C. J. *Advanced Functional Materials* **2006**, *16*, 1499–1505.
- (37) SwissLitho AG Personal Communication., 2018.
- (38) Wei, Z.; Wang, D.; Kim, S.; Kim, S.-Y.; Hu, Y.; Yakes, M. K.; Laracuentte, A. R.; Dai, Z.; Marder, S. R.; Berger, C.; King, W. P.; Heer, W. A. d.; Sheehan, P. E.; Riedo, E. *Science* **2010**, *328*, 1373–1376.
- (39) Neuber, C. et al. In, 2014; Vol. 9049, pp 90491V–90491V–9.
- (40) Neuber, C. et al. In, 2015; Vol. 9425, pp 1–7.
- (41) Hua, Y.; Saxena, S. R.; Henderson, C. L.; King, W. P. *Journal of Micro/Nanolithography, MEMS, and MOEMS* **2007**, *6*, 023012.
- (42) Kim, H. J.; Moldovan, N.; Felts, J. R.; Somnath, S.; Dai, Z.; Jacobs, T. D. B.; Carpick, R. W.; Carlisle, J. A.; King, W. P. *Nanotechnology* **2012**, *23*, 495302.
- (43) Duvigneau, J.; Schönherr, H.; Vancso, G. J. *ACS Nano* **2010**, *4*, 6932–6940.
- (44) King, W. P.; Goodson, K. E. *Journal of Heat Transfer* **2007**, *129*, 1600–1604.
- (45) Vettiger, P.; Cross, G.; Despont, M.; Drechsler, U.; Durig, U.; Gotsmann, B.; Haberle, W.; Lantz, M. A.; Rothuizen, H. E.; Stutz, R.; Binnig, G. K. *IEEE Transactions on Nanotechnology* **2002**, *1*, 39–55.
- (46) Hua, Y.; King, W. P.; Henderson, C. L. *Microelectronic Engineering* **2008**, *85*, 934–936.
- (47) Vettiger, P.; Brugger, J.; Despont, M.; Drechsler, U.; Dürig, U.; Häberle, W.; Lutwyche, M.; Rothuizen, H.; Stutz, R.; Widmer, R.; Binnig, G. *Microelectronic Engineering* **1999**, *46*, 11–17.
- (48) Nam, H.-J.; Kim, Y.-S.; Lee, C. S.; Jin, W.-H.; Jang, S.-S.; Cho, I.-J.; Bu, J.-U.; Choi, W. B.; Choi, S. W. *Sensors and Actuators A: Physical* **2007**, *134*, 329–333.
- (49) Kim, Y.-S.; Jang, S.; Lee, C. S.; Jin, W.-H.; Cho, I.-J.; Ha, M.-H.; Nam, H.-J.; Bu, J.-U.; Chang, S.-I.; Yoon, E. *Sensors and Actuators A: Physical* **2007**, *135*, 67–72.
- (50) Binnig, G.; Despont, M.; Drechsler, U.; Häberle, W.; Lutwyche, M.; Vettiger, P.; Mamin, H. J.; Chui, B. W.; Kenny, T. W. *Applied Physics Letters* **1999**, *74*, 1329–1331.
- (51) Huang, C.-M.; Yeh, C.-H.; Chen, L.; Huang, D.-A.; Kuo, C. *ACS Applied Materials & Interfaces* **2013**, *5*, 120–127.

Bibliography

- (52) Lisunova, Y.; Spieser, M.; Juttin, R. D. D.; Holzner, F.; Brugger, J. *Microelectronic Engineering* **2017**, *180*, 20–24.
- (53) Lisunova, Y.; Brugger, J. *Microelectronic Engineering* **2018**, *193*, 23–27.
- (54) Sadeghian, H.; Paul, P. C.; Herfst, R.; Dekker, B.; Winters, J.; Maturova, K. In *2017 IEEE International Conference on Advanced Intelligent Mechatronics (AIM)*, 2017, pp 700–705.
- (55) Gottlieb, S.; Lorenzoni, M.; Evangelio, L.; Fernández-Regúlez, M.; Ryu, Y. K.; Rawlings, C.; Spieser, M.; Knoll, A. W.; F Perez-Murano *Nanotechnology* **2017**, *28*, 175301.
- (56) Ryu Cho, Y. K.; Rawlings, C. D.; Wolf, H.; Spieser, M.; Bisig, S.; Reidt, S.; Sousa, M.; Khanal, S. R.; Jacobs, T. D. B.; Knoll, A. W. *ACS Nano* **2017**, *11*, 11890–11897.
- (57) Cheong, L. L.; Paul, P.; Holzner, F.; Despont, M.; Coady, D. J.; Hedrick, J. L.; Allen, R.; Knoll, A. W.; Duerig, U. *Nano Letters* **2013**, *13*, 4485–4491.
- (58) Rawlings, C. D.; Zientek, M.; Spieser, M.; Urbonas, D.; Stöferle, T.; Mahrt, R. F.; Lisunova, Y.; Brugger, J.; Duerig, U.; Knoll, A. W. *Scientific Reports* **2017**, *7*, 16502.
- (59) Holzner, F.; Paul, P.; Drechsler, U.; Despont, M.; Knoll, A. W.; Duerig, U. *Applied Physics Letters* **2011**, *99*, 023110.
- (60) Holzner, F.; Kuemin, C.; Paul, P.; Hedrick, J. L.; Wolf, H.; Spencer, N. D.; Duerig, U.; Knoll, A. W. *Nano Letters* **2011**, *11*, 3957–3962.
- (61) Wolf, H.; Colin, R.; Mensch, P.; Hedrick, J. L.; Coady, D. J.; Duerig, U.; Knoll, A. W. *Journal of Vacuum Science & Technology B, Nanotechnology and Microelectronics: Materials, Processing, Measurement, and Phenomena* **2014**, *33*, 02B102.
- (62) Rawlings, C.; Spieser, M.; Schwemmer, C.; Kulmala, T. S.; Cho, Y. K. R.; Bonanni, S.; Duerig, U.; Paul, P.; Knoll, A. W. In *2017 19th International Conference on Solid-State Sensors, Actuators and Microsystems (TRANSDUCERS)*, 2017 19th International Conference on Solid-State Sensors, Actuators and Microsystems (TRANSDUCERS), 2017, pp 418–422.
- (63) Kulmala, T. S.; Rawlings, C. D.; Spieser, M.; Glinsner, T.; Schleunitz, A.; Bullerjahn, F.; Holzner, F. In *Novel Patterning Technologies 2018*, Novel Patterning Technologies 2018, International Society for Optics and Photonics: 2018; Vol. 10584, p 1058412.
- (64) Tolk, M.; Fenwick, O.; Ahmad, S.; Cacialli, F. *Journal of Applied Physics* **2012**, *111*, 124317.
- (65) Shaw, J. E.; Stavrinou, P. N.; Anthopoulos, T. D. *Nanoscale* **2014**, *6*, 5813–5819.
- (66) Wang, D.; Kim, S.; Underwood, W. D.; Giordano, A. J.; Henderson, C. L.; Dai, Z.; King, W. P.; Marder, S. R.; Riedo, E. *Applied Physics Letters* **2009**, *95*, 233108.

-
- (67) Duvigneau, J.; Schönherr, H.; Vancso, G. J. *ACS Applied Materials & Interfaces* **2011**, *3*, 3855–3865.
- (68) Shaw, J. E.; Stavrinou, P. N.; Anthopoulos, T. D. *Advanced Materials* **2013**, *25*, 552–558.
- (69) (Boday, D. J.; Garcia, J. M.; Hedrick, J. L.; Wojtecki, R. J.). Poly(thioaminal) probe based lithography., US20170153269A1, 2017.
- (70) Wang, D.; Szoszkiewicz, R.; Kodali, V.; Curtis, J.; Marder, S.; Riedo, E. In *Scanning Probe Microscopy in Nanoscience and Nanotechnology*; NanoScience and Technology; Springer, Berlin, Heidelberg: 2010, pp 795–811.
- (71) Carroll, K. M.; Giordano, A. J.; Wang, D.; Kodali, V. K.; Scrimgeour, J.; King, W. P.; Marder, S. R.; Riedo, E.; Curtis, J. E. *Langmuir* **2013**, *29*, 8675–8682.
- (72) Szoszkiewicz, R.; Okada, T.; Jones, S. C.; Li, T.-D.; King, W. P.; Marder, S. R.; Riedo, E. *Nano Letters* **2007**, *7*, 1064–1069.
- (73) Carroll, K. M.; Desai, M.; Giordano, A. J.; Scrimgeour, J.; King, W. P.; Riedo, E.; Curtis, J. E. *ChemPhysChem* **2014**, *15*, 2530–2535.
- (74) Hamann, H. F.; O’Boyle, M.; Martin, Y. C.; Rooks, M.; Wickramasinghe, H. K. *Nature Materials* **2006**, *5*, 383–387.
- (75) Podpirka, A.; Lee, W.-K.; Ziegler, J. I.; Brintlinger, T. H.; Felts, J. R.; Simpkins, B. S.; Bassim, N. D.; Laracuenta, A. R.; Sheehan, P. E.; Ruppalt, L. B. *Nanoscale* **2017**, *9*, 8815–8824.
- (76) Kim, S.; Bastani, Y.; Lu, H.; King, W. P.; Marder, S.; Sandhage, K. H.; Gruverman, A.; Riedo, E.; Bassiri-Gharb, N. *Advanced Materials* **2011**, *23*, 3786–3790.
- (77) Albisetti, E.; Petti, D.; Pancaldi, M.; Madami, M.; Tacchi, S.; Curtis, J.; King, W. P.; Papp, A.; Csaba, G.; Porod, W.; Vavassori, P.; Riedo, E.; Bertacco, R. *Nature Nanotechnology* **2016**, *11*, 545–551.
- (78) Skaug, M. J.; Schwemmer, C.; Fringes, S.; Rawlings, C. D.; Knoll, A. W. *Science* **2018**, *359*, 1505–1508.
- (79) Duvigneau, J.; Schönherr, H.; Vancso, G. J. *Langmuir* **2008**, *24*, 10825–10832.
- (80) Hinz, M.; Kleiner, A.; Hild, S.; Marti, O.; Dürig, U.; Gotsmann, B.; Drechsler, U.; Albrecht, T. R.; Vettiger, P. *European Polymer Journal* **2004**, *40*, 957–964.
- (81) Cahill, D. G.; Goodson, K.; Majumdar, A. *Journal of Heat Transfer* **2001**, *124*, 223–241.
- (82) Brites, C. D. S.; Lima, P. P.; Silva, N. J. O.; Millán, A.; Amaral, V. S.; Palacio, F.; Carlos, L. D. *Nanoscale* **2012**, *4*, 4799–4829.
- (83) Quintanilla, M.; Liz-Marzán, L. M. *Nano Today* **2018**, *19*, 126–145.
- (84) Gomès, S.; Assy, A.; Chapuis, P.-O. *Physica Status Solidi A* **2015**, *212*, 477–494.

Bibliography

- (85) Rangelow, I.; Gotszalk, T.; Grabiec, P.; Edinger, K.; Abedinov, N. *Microelectronic Engineering* **2001**, *57-58*, Micro- and Nano-Engineering 2000, 737–748.
- (86) Menges, F.; Riel, H.; Stemmer, A.; Gotsmann, B. *Nano Letters* **2012**, *12*, 596–601.
- (87) Menges, F.; Mensch, P.; Schmid, H.; Riel, H.; Stemmer, A.; Gotsmann, B. *Nature Communications* **2016**, *7*, 10874.
- (88) Sadat, S.; Tan, A.; Chua, Y. J.; Reddy, P. *Nano Letters* **2010**, *10*, 2613–2617.
- (89) Kim, K.; Jeong, W.; Lee, W.; Reddy, P. *ACS Nano* **2012**, *6*, 4248–4257.
- (90) Shekhawat, G. S.; Ramachandran, S.; Jiryaei Sharahi, H.; Sarkar, S.; Hujsak, K.; Li, Y.; Hagglund, K.; Kim, S.; Aden, G.; Chand, A.; Dravid, V. P. *ACS Nano* **2018**, *12*, 1760–1767.
- (91) Pavlov, A. *Applied Physics Letters* **2004**, *85*, 2095–2097.
- (92) Mecklenburg, M.; Hubbard, W. A.; White, E. R.; Dhall, R.; Cronin, S. B.; Aloni, S.; Regan, B. C. *Science* **2015**, *347*, 629–632.
- (93) Mecklenburg, M.; Zutter, B.; Regan, B. C. *Physical Review Applied* **2018**, *9*, 014005.
- (94) Lagos, M. J.; Batson, P. E. *Nano Letters* **2018**, *18*, PMID: 29874456, 4556–4563.
- (95) Teyssieux, D.; Thiery, L.; Cretin, B. *Review of Scientific Instruments* **2007**, *78*, 034902.
- (96) Weng, Q.; Lin, K.-T.; Yoshida, K.; Nema, H.; Komiyama, S.; Kim, S.; Hirakawa, K.; Kajihara, Y. *Nano Letters* **2018**, *18*, PMID: 29879352, 4220–4225.
- (97) Abel, M. R.; Wright, T. L.; King, W. P.; Graham, S. *IEEE Transactions on Components and Packaging Technologies* **2007**, *30*, 200–208.
- (98) Yue, Y.; Chen, X.; Wang, X. *ACS Nano* **2011**, *5*, 4466–4475.
- (99) Milichko, V. A.; Zuev, D. A.; Baranov, D. G.; Zograf, G. P.; Volodina, K.; Krasilin, A. A.; Mukhin, I. S.; Dmitriev, P. A.; Vinogradov, V. V.; Makarov, S. V.; Belov, P. A. *Laser & Photonics Reviews*, *12*, 1700227.
- (100) Aigouy, L.; Tessier, G.; Mortier, M.; Charlot, B. *Applied Physics Letters* **2005**, *87*, 184105.
- (101) Saïdi, E.; Samson, B.; Aigouy, L.; Volz, S.; Löw, P.; Bergaud, C.; Mortier, M. *Nanotechnology* **2009**, *20*, 115703.
- (102) Huang, F.; Gao, Y.; Zhou, J.; Xu, J.; Wang, Y. *Journal of Alloys and Compounds* **2015**, *639*, 325–329.
- (103) Assy, A.; Lin, H.-J.; Schoenauer-Sebag, M.; Gredin, P.; Mortier, M.; Billot, L.; Chen, Z.; Aigouy, L. *Sensors and Actuators A: Physical* **2016**, *250*, 71–77.
- (104) Debasu, M. L.; Brites, C. D. S.; Balabhadra, S.; Oliveira, H.; Rocha, J.; Carlos, L. D. *ChemNanoMat* **2016**, *2*, 520–527.

-
- (105) Geitenbeek, R. G.; Prins, P. T.; Albrecht, W.; van Blaaderen, A.; Weckhuysen, B. M.; Meijerink, A. *The Journal of Physical Chemistry C* **2017**, *121*, 3503–3510.
- (106) Kalinichev, A.; Kurochkin, M.; Golyeva, E.; Kurochkin, A.; Lähderanta, E.; Mikhailov, M.; Kolesnikov, I. *Journal of Luminescence* **2018**, *195*, 61–66.
- (107) Gao, G.; Busko, D.; Kauffmann-Weiss, S.; Turshatov, A.; Howard, I. A.; Richards, B. S. *Journal of Materials Chemistry C* **2018**, *6*, 4163–4170.
- (108) Gao, Y.; Cheng, Y.; Huang, F.; Lin, H.; Xu, J.; Wang, Y. *Journal of Alloys and Compounds* **2018**, *735*, 1546–1552.
- (109) Baral, S.; Rafiei Miandashti, A.; Richardson, H. H. *Nanoscale* **2018**, *10*, 941–948.
- (110) Plakhotnik, T.; Gruber, D. *Physical Chemistry Chemical Physics* **2010**, *12*, 9751–9756.
- (111) Laraoui, A.; Aycock-Rizzo, H.; Gao, Y.; Lu, X.; Riedo, E.; Meriles, C. A. *Nature Communications* **2015**, *6*, 8954.
- (112) Plakhotnik, T.; Doherty, M. W.; Manson, N. B. *Physical Review B* **2015**, *92*, 081203.
- (113) Neumann, P.; Jakobi, I.; Dolde, F.; Burk, C.; Reuter, R.; Waldherr, G.; Honert, J.; Wolf, T.; Brunner, A.; Shim, J. H.; Suter, D.; Sumiya, H.; Isoya, J.; Wrachtrup, J. *Nano Letters* **2013**, *13*, PMID: 23721106, 2738–2742.
- (114) Wang, N.; Liu, G.-Q.; Leong, W.-H.; Zeng, H.; Feng, X.; Li, S.-H.; Dolde, F.; Fedder, H.; Wrachtrup, J.; Cui, X.-D.; Yang, S.; Li, Q.; Liu, R.-B. *Physical Review X* **2018**, *8*, 011042.
- (115) Hummel, R. E., *Electronic Properties of Materials*, 4th ed.; Springer-Verlag: New York, 2011.
- (116) Chung, J.; Kim, K.; Hwang, G.; Kwon, O.; Choi, Y. K.; Lee, J. S. *International Journal of Thermal Sciences* **2012**, *62*, 109–113.
- (117) Childs, P. R. N. In *Thermometry at the Nanoscale*, Carlos, L. D., Palacio, F., Eds.; Nanoscience & Nanotechnology; The Royal Society of Chemistry: 2015; Chapter 1, pp 1–22.
- (118) Goodson, K. E.; Asheghi, M. *Microscale Thermophysical Engineering* **1997**, *1*, 225–235.
- (119) Weng, Q.; Komiyama, S.; Yang, L.; An, Z.; Chen, P.; Biehs, S.-A.; Kajihara, Y.; Lu, W. *Science* **2018**, *360*, 775–778.
- (120) Li, L.; Liu, K.; Suen, B.; Liu, Q.; King, A.; Talke, F. E. *Tribology Letters* **2018**, *66*, 26.
- (121) Larkin, P. J. In *Infrared and Raman Spectroscopy (Second Edition)*, Larkin, P. J., Ed., Second Edition; Elsevier: 2018, pp 7–28.
- (122) McCarthy, B.; Zhao, Y.; Grover, R.; Sarid, D. *Applied Physics Letters* **2005**, *86*, 111914.

Bibliography

- (123) Nelson, B. A.; King, W. P. *Sensors and Actuators A: Physical* **2007**, *140*, 51–59.
- (124) Spieser, M.; Rawlings, C.; Lörtscher, E.; Duerig, U.; Knoll, A. W. *Journal of Applied Physics* **2017**, *121*, 174503.
- (125) Quintanilla, M.; Benayas, A.; Naccache, R.; Vetrone, F. **2015**, 124–166.
- (126) Brites, C. D. S.; Fiaczyk, K.; Ramalho, J. F. C. B.; Sójka, M.; Carlos, L. D.; Zych, E. *Advanced Optical Materials* **2018**, *6*, 1701318.
- (127) Tilley, R. J. D. In *Encyclopedia of Color Science and Technology*, Luo, R., Ed.; Springer New York: New York, NY, 2014, pp 1–9.
- (128) Berthel, M.; Mollet, O.; Dantelle, G.; Gacoin, T.; Huant, S.; Drezet, A. *Physical Review B* **2015**, *91*, 035308.
- (129) Schirhagl, R.; Chang, K.; Loretz, M.; Degen, C. L. *Annual Review of Physical Chemistry* **2014**, *65*, 83–105.
- (130) Toyli, D. M.; Christle, D. J.; Alkauskas, A.; Buckley, B. B.; Van de Walle, C. G.; Awschalom, D. D. *Physical Review X* **2012**, *2*, 031001.
- (131) Doherty, M. W.; Acosta, V. M.; Jarmola, A.; Barson, M. S. J.; Manson, N. B.; Budker, D.; Hollenberg, L. C. L. *Physical Review B* **2014**, *90*, 041201.
- (132) Toyli, D. M.; Casas, C. F. d. l.; Christle, D. J.; Dobrovitski, V. V.; Awschalom, D. D. *Proceedings of the National Academy of Sciences* **2013**, *110*, 8417–8421.
- (133) Tetienne, J.-P.; Lombard, A.; Simpson, D. A.; Ritchie, C.; Lu, J.; Mulvaney, P.; Hollenberg, L. C. L. *Nano Letters* **2016**, *16*, 326–333.
- (134) Tzeng, Y.-K.; Tsai, P.-C.; Liu, H.-Y.; Chen, O. Y.; Hsu, H.; Yee, F.-G.; Chang, M.-S.; Chang, H.-C. *Nano Letters* **2015**, *15*, 3945–3952.
- (135) Plakhotnik, T.; Doherty, M. W.; Cole, J. H.; Chapman, R.; Manson, N. B. *Nano Letters* **2014**, *14*, 4989–4996.
- (136) Kumaran, C. R.; Tiwari, B.; Chandran, M.; Bhattacharya, S. S.; Ramachandra Rao, M. S. *Journal of Nanoparticle Research* **2013**, *15*, 1509.
- (137) Efremov, V. P.; Zakatilova, E. I.; Maklashova, I. V.; Shevchenko, N. V. *Journal of Physics: Conference Series* **2018**, *946*, 012107.
- (138) Fan, J.-W.; Cojocar, I.; Becker, J.; Fedotov, I. V.; Alkahtani, M. H. A.; Alajlan, A.; Blakley, S.; Rezaee, M.; Lyamkina, A.; Palyanov, Y. N.; Borzdov, Y. M.; Yang, Y.-P.; Zheltikov, A.; Hemmer, P.; Akimov, A. V. *ACS Photonics* **2018**, *5*, 765–770.
- (139) Nguyen, C. T.; Evans, R. E.; Sipahigil, A.; Bhaskar, M. K.; Sukachev, D. D.; Agafonov, V. N.; Davydov, V. A.; Kulikova, L. F.; Jelezko, F.; Lukin, M. D. *Applied Physics Letters* **2018**, *112*, 203102.
- (140) Zhou, Y.; Wang, J.; Zhang, X.; Li, K.; Cai, J.; Gao, W. *Phys. Rev. Applied* **2017**, *8*, 044015.

-
- (141) Adamas Nanotechnologies Product sheet NV – High brightness., <http://adamasnano.com/products.html> (accessed 08/15/2018).
- (142) Bae, J. H.; Ono, T.; Esashi, M. *Diamond and Related Materials* **2003**, *12*, 2128–2135.
- (143) Li, W.; Mingo, N.; Lindsay, L.; Broido, D. A.; Stewart, D. A.; Katcho, N. A. *Physical Review B* **2012**, *85*, 195436.
- (144) Fletcher, P. C.; Felts, J. R.; Dai, Z.; Jacobs, T. D.; Zeng, H.; Lee, W.; Sheehan, P. E.; Carlisle, J. A.; Carpick, R. W.; King, W. P. *ACS Nano* **2010**, *4*, 3338–3344.
- (145) Appel, P.; Neu, E.; Ganzhorn, M.; Barfuss, A.; Batzer, M.; Gratz, M.; Tschöpe, A.; Maletinsky, P. *Review of Scientific Instruments* **2016**, *87*, 063703.
- (146) Zimmermann, S. T.; Balkenende, D. W. R.; Lavrenova, A.; Weder, C.; Brugger, J. *ACS Applied Materials & Interfaces* **2017**, *9*, 41454–41461.
- (147) Yang, L.; Tan, X.; Wang, Z.; Zhang, X. *Chemical Reviews* **2015**, *115*, 7196–7239.
- (148) Webber, M. J.; Appel, E. A.; Meijer, E. W.; Langer, R. *Nature Materials* **2016**, *15*, 13–26.
- (149) Wang, H.; Ji, X.; Li, Z.; Huang, F. *Advanced Materials* **2017**, *29*, 1606117.
- (150) Balkenende, D. W. R.; Olson, R. A.; Balog, S.; Weder, C.; Montero de Espinosa, L. *Macromolecules* **2016**, *49*, 7877–7885.
- (151) Crenshaw, B. R.; Weder, C. *Advanced Materials* **2005**, *17*, 1471–1476.
- (152) Balkenende, D. W. R.; Monnier, C. A.; Fiore, G. L.; Weder, C. *Nature Communications* **2016**, *7*, 10995.
- (153) Sijbesma, R. P.; Beijer, F. H.; Brunsveld, L.; Folmer, B. J. B.; Hirschberg, J. H. K. K.; Lange, R. F. M.; Lowe, J. K. L.; Meijer, E. W. *Science* **1997**, *278*, 1601–1604.
- (154) Sagara, Y.; Lavrenova, A.; Crochet, A.; Simon, Y. C.; Fromm, K. M.; Weder, C. *Chemistry – A European Journal* **2016**, *22*, 4374–4378.
- (155) Calvino, C.; Neumann, L.; Weder, C.; Schrettl, S. *Journal of Polymer Science Part A: Polymer Chemistry* **2017**, *55*, 640–652.
- (156) Sagara, Y.; Kubo, K.; Nakamura, T.; Tamaoki, N.; Weder, C. *Chemistry of Materials* **2017**, *29*, 1273–1278.
- (157) Lavrenova, A.; Balkenende, D. W. R.; Sagara, Y.; Schrettl, S.; Simon, Y. C.; Weder, C. *Journal of the American Chemical Society* **2017**, *139*, 4302–4305.
- (158) Lott, J.; Ryan, C.; Valle, B.; Johnson, J. R.; Schiraldi, D. A.; Shan, J.; Singer, K. D.; Weder, C. *Advanced Materials* **2011**, *23*, 2425–2429.
- (159) Wei, P.; Li, B.; de Leon, A.; Pentzer, E. *Journal of Materials Chemistry C* **2017**, *5*, 5780–5786.
- (160) Dürig, U. *Journal of Applied Physics* **2005**, *98*, 044906.

Bibliography

- (161) Holzner, F. Thermal Scanning Probe Lithography using Polyphthalaldehyde., Doctoral Thesis, ETH Zürich, 2013.
- (162) Nelson, B. A.; King, W. P. *Nanoscale and Microscale Thermophysical Engineering* **2008**, *12*, 98–115.
- (163) Pozidis, H.; Haberle, W.; Wiesmann, D.; Drechsler, U.; Despont, M.; Albrecht, T. R.; Eleftheriou, E. *IEEE Transactions on Magnetics* **2004**, *40*, 2531–2536.
- (164) Vogler, C.; Abert, C.; Bruckner, F.; Suess, D.; Praetorius, D. *Applied Physics Letters* **2016**, *108*, 102406.
- (165) Omenetto, F. G.; Kaplan, D. L. *Science* **2010**, *329*, 528–531.
- (166) Balčytis, A.; Ryu, M.; Wang, X.; Novelli, F.; Seniutinas, G.; Du, S.; Wang, X.; Li, J.; Davis, J.; Appadoo, D.; Morikawa, J.; Juodkazis, S. *Materials* **2017**, *10*, 356.
- (167) Kim, U.-J.; Park, J.; Kim, H. J.; Wada, M.; Kaplan, D. L. *Biomaterials* **2005**, *26*, 2775–2785.
- (168) Vepari, C.; Kaplan, D. L. *Progress in Polymer Science* **2007**, *32*, 991–1007.
- (169) Hu, X.; Kaplan, D.; Cebe, P. *Macromolecules* **2006**, *39*, 6161–6170.
- (170) Lawrence, B. D.; Cronin-Golomb, M.; Georgakoudi, I.; Kaplan, D. L.; Omenetto, F. G. *Biomacromolecules* **2008**, *9*, 1214–1220.
- (171) Capelli, R.; Amsden, J.; Generali, G.; Toffanin, S.; Benfenati, V.; Muccini, M.; Kaplan, D.; Omenetto, F.; Zamboni, R. *Organic Electronics* **2011**, *12*, 1146–1151.
- (172) Pal, R. K.; Yadavalli, V. K. *Nanotechnology* **2018**, *29*, 335301.
- (173) Tao Hu; Kaplan David L.; Omenetto Fiorenzo G. *Advanced Materials* **2012**, *24*, 2824–2837.
- (174) Perry, H.; Gopinath, A.; Kaplan, D. L.; Dal Negro, L.; Omenetto, F. G. *Advanced Materials* **2008**, *20*, 3070–3072.
- (175) Mondia, J. P.; Amsden, J. J.; Lin, D.; Negro, L. D.; Kaplan, D. L.; Omenetto, F. G. *Advanced Materials* **2010**, *22*, 4596–4599.
- (176) Amsden, J. J.; Domachuk, P.; Gopinath, A.; White, R. D.; Negro, L. D.; Kaplan, D. L.; Omenetto, F. G. *Advanced Materials* **2010**, *22*, 1746–1749.
- (177) Kim, S.; Mitropoulos, A. N.; Spitzberg, J. D.; Tao, H.; Kaplan, D. L.; Omenetto, F. G. *Nature Photonics* **2012**, *6*, 818–823.
- (178) Kurland, N. E.; Dey, T.; Kundu, S. C.; Yadavalli, V. K. *Advanced Materials* **2013**, *25*, 6207–6212.
- (179) Bucciarelli, A.; Pal, R. K.; Maniglio, D.; Quaranta, A.; Mulloni, V.; Motta, A.; Yadavalli, V. K. *Macromolecular Materials and Engineering* **2017**, *302*, 1700110.
- (180) Liu, W. et al. *Advanced Science* **2017**, *4*, 1700191.

-
- (181) Dickerson, M. B.; Dennis, P. B.; Tondiglia, V. P.; Nadeau, L. J.; Singh, K. M.; Drummy, L. F.; Partlow, B. P.; Brown, D. P.; Omenetto, F. G.; Kaplan, D. L.; Naik, R. R. *ACS Biomaterials Science & Engineering* **2017**, *3*, 2064–2075.
- (182) Park, J.; Lee, S.-G.; Marelli, B.; Lee, M.; Kim, T.; Oh, H.-K.; Jeon, H.; Omenetto, F. G.; Kim, S. *RSC Advances* **2016**, *6*, 39330–39334.
- (183) Kim, S.; Marelli, B.; Brenckle, M. A.; Mitropoulos, A. N.; Gil, E.-S.; Tsioris, K.; Tao, H.; Kaplan, D. L.; Omenetto, F. G. *Nature nanotechnology* **2014**, *9*, 306.
- (184) Cebe, P.; Hu, X.; Kaplan, D. L.; Zhuravlev, E.; Wurm, A.; Arbeiter, D.; Schick, C. *Scientific Reports* **2013**, *3*, srep01130.
- (185) Cebe, P.; Partlow, B. P.; Kaplan, D. L.; Wurm, A.; Zhuravlev, E.; Schick, C. *Acta Biomaterialia* **2017**, *55*, 323–332.
- (186) Paul, P. C.; Knoll, A. W.; Holzner, F.; Despont, M.; Duerig, U. *Nanotechnology* **2011**, *22*, 275306.
- (187) Rockwood, D. N.; Preda, R. C.; Yücel, T.; Wang, X.; Lovett, M. L.; Kaplan, D. L. *Nature Protocols* **2011**, *6*, 1612–1631.
- (188) Patsis, G. P.; Constantoudis, V.; Tserepi, A.; Gogolides, E.; Grozev, G. *Journal of Vacuum Science & Technology B: Microelectronics and Nanometer Structures Processing, Measurement, and Phenomena* **2003**, *21*, 1008–1018.
- (189) Altebaeumer, T.; Gotsmann, B.; Pozidis, H.; Knoll, A.; Duerig, U. *Nano Letters* **2008**, *8*, 4398–4403.
- (190) Minoura, N.; Tsukada, M.; Nagura, M. *Polymer* **1990**, *31*, 265–269.
- (191) Yazawa, K.; Ishida, K.; Masunaga, H.; Hikima, T.; Numata, K. *Biomacromolecules* **2016**, *17*, 1057–1066.
- (192) Shulha, H.; Po Foo, C. W.; Kaplan, D. L.; Tsukruk, V. V. *Polymer* **2006**, *47*, 5821–5830.
- (193) Gotsmann, B.; Lantz, M. A.; Knoll, A.; Dürig, U. In *Nanotechnology*, Fuchs, H., Ed.; Nanoprobes, Vol. 6; Wiley-VCH Verlag GmbH & Co: 2009, p 121.
- (194) Morikawa, J.; Ryu, M.; Maximova, K.; Balčytis, A.; Seniutinas, G.; Fan, L.; Mizeikis, V.; Li, J.; Wang, X.; Zamengo, M.; Wang, X.; Juodkasis, S. *RSC Advances* **2016**, *6*, 11863–11869.
- (195) Langtangen, H. P.; Logg, A., *Solving PDEs in Python: The FEniCS Tutorial I*; Simula SpringerBriefs on Computing; Springer International Publishing: 2016.
- (196) Geuzaine, C.; Remacle, J.-F. *International Journal for Numerical Methods in Engineering* **2009**, *79*, 1309–1331.
- (197) Alnæs, M.; Blechta, J.; Hake, J.; Johansson, A.; Kehlet, B.; Logg, A.; Richardson, C.; Ring, J.; Rognes, M.; Wells, G. *Archive of Numerical Software* **2015**, *3*, 9–23.

Bibliography

- (198) Duvigneau, J. Scanning Thermal Lithography for Nanopatterning of Polymers. Transient Heat Transport and Thermal Chemical Functionalization Across the Length Scales., English, Ph.D. Thesis, University of Twente, 2011.
- (199) Center of MicroNanoTechnology (CMI) Manual for SPTS APS., <https://cmi.epfl.ch/etch/APS.php>.
- (200) Tseng, Y.-C.; Peng, Q.; Ocola, L. E.; Czaplewski, D. A.; Elam, J. W.; Darling, S. B. *Journal of Materials Chemistry* **2011**, *21*, 11722–11725.
- (201) Doherty, M. W.; Struzhkin, V. V.; Simpson, D. A.; McGuinness, L. P.; Meng, Y.; Stacey, A.; Karle, T. J.; Hemley, R. J.; Manson, N. B.; Hollenberg, L. C. L.; Prawer, S. *Phys. Rev. Lett.* **2014**, *112*, 047601.
- (202) Chen, X.-D.; Dong, C.-H.; Sun, F.-W.; Zou, C.-L.; Cui, J.-M.; Han, Z.-F.; Guo, G.-C. *Applied Physics Letters* **2011**, *99*, 161903.
- (203) Plakhotnik, T. *Current Opinion in Solid State and Materials Science* **2017**, *21*, 25–34.
- (204) Oeckinghaus, T.; Stöhr, R.; Kolesov, R.; Tisler, J.; Reinhard, F.; Wrachtrup, J. *Review of Scientific Instruments* **2014**, *85*, 073101.
- (205) Roithner Laser Technik GmbH LD-520-50SG., 2012.
- (206) Stelzer, E. H. In *Handbook of Biological Confocal Microscopy*, Pawley, J. B., Ed., 3rd ed.; Springer Science+Business Media: New York, 2006; Chapter 9.
- (207) Dréau, A.; Lesik, M.; Rondin, L.; Spinicelli, P.; Arcizet, O.; Roch, J.-F.; Jacques, V. *Physical Review B* **2011**, *84*, 195204.
- (208) Rawlings, C.; Ryu, Y. K.; Rüegg, M.; Lassaline, N.; Schwemmer, C.; Duerig, U.; Knoll, A. W.; Durrani, Z.; Wang, C.; Liu, D.; Jones, M. E. *Nanotechnology* **2018**, *29*, 505302.
- (209) Schmidt, A. Contact Thermal Lithography., MA thesis, Massachusetts Institute of Technology, 2004.
- (210) Peric, O.; Hannebelle, M.; Adams, J. D.; Fantner, G. E. *Nano Research* **2017**, *10*, 3896–3908.
- (211) Ivády, V.; Simon, T.; Maze, J. R.; Abrikosov, I. A.; Gali, A. *Physical Review B* **2014**, *90*, 235205.

Acronyms

AC Alternating current.

AFM Atomic force microscope.

b-SPL Bias-induced scanning probe lithography.

BPO Benzoyl peroxide.

c-SPL Current-controlled scanning probe lithography.

CAR Chemically amplified resist.

CCD Charge-coupled device.

CMOS Complementary metal-oxide-semiconductor.

DAQ Data acquisition.

DC Direct current.

DUV Deep ultraviolet.

DWF Debey-Waller factor.

EBL Electron-beam lithography.

EPR Electron paramagnetic resonance.

ESR Electron spin resonance.

EUVL Extreme ultraviolet lithography.

FWHM Full width at half maximum.

GEB Gaussian electron-beam.

HSQ Hydrogen silsesquioxane.

Acronyms

- ICP** Inductively coupled plasma.
- ICS** Intercrossing system.
- IR** Infrared.
- LED** Light emitting diode.
- LER** Line edge roughness.
- MRL** Mechanoresponsive luminescent.
- MW** Microwave.
- NIL** Nanoimprint lithography.
- NIR** Near infrared.
- NV** Nitrogen vacancy.
- o-SPL** Oxidation scanning probe lithography.
- ODMR** Optically detected magnetic resonance.
- OPV** Oligo-p-phenylenevinylene.
- PC** Polycarbonate.
- PCM** Phase change material.
- PDMS** Poly(dimethylsiloxane).
- PE** Polyethylene.
- PEAK** Poly(arylether ketone).
- PEET** Plasmon expansion thermometry.
- PET** Poly(ethylene terephthalate).
- PHOST** Poly(hydroxyl styrene).
- PMMA** Poly(methyl methacrylate).
- PPA** Poly(phthalaldehyde).
- PPC** Poly(propylene carbonate).
- PPV** Poly(p-phenylene vinylene).
- PS** Polystyrene.

- PS-BCB** Poly(styrene-r-benzocyclobutene).
- PVD** Physical vapor deposition.
- PVDF** Poly(vinylidene fluoride).
- QD** Quantum dots.
- QSR-5** Sterol-based QSR-5 (negative tone resist).
- RMS** Root mean square.
- RPM** Rounds per minute.
- RT** Room temperature.
- SAM** Self-assembled monolayer.
- SEM** Scanning electron microscopy.
- SNOM** Scanning near-field optical microscopy.
- SPL** Scanning probe lithography.
- SPM** Scanning probe microscopy.
- SThM** Scanning thermal microscopy.
- SU-8** Epoxy based resist.
- t-SPL** Thermal scanning probe lithography.
- T_g** Glass transition temperature.
- tc-SPL** Thermochemical scanning probe lithography.
- TEM** Transmission electron microscopy.
- THP** Tetrahydropyran.
- TRL** Thermoresponsive luminescent.
- UHV** Ultrahigh vacuum.
- Upy** Ureido-4-pyrimidinone.
- UV** Ultraviolet.
- VI** Virtual Instrument.

Acronyms

VS Variable shaped beam.

WLF Williams-Landel-Ferry.

ZFS Zero-field splitting.

Photographic Credits

- Figures 1.1 and 1.2a reprinted with permission from Garcia, R. et al. *Nature Nanotechnology* **2014**, *9*, 577–587
Copyright (2014) Springer Nature
- Figure 1.4a reprinted with permission from Menges, F. et al. *Nature Communications* **2016**, *7*, 10874
Copyright (2016) Springer Nature
- Figure 1.4b reprinted with permission from Shekhawat, G. S. et al. *ACS Nano* **2018**, *12*, 1760–1767
Copyright (2018) American Chemical Society
- Figure 1.5a reprinted with permission from Weng, Q. et al. *Science* **2018**, *360*, 775–778
Copyright (2018) The American Association for the Advancement of Science
- Figure 1.5b reprinted with permission from Li, L. et al. *Tribology Letters* **2018**, *66*, 26
Copyright (2018) Springer Nature
- Figure 1.6a reprinted with permission from Aigouy, L. et al. *Applied Physics Letters* **2005**, *87*, 184105
Copyright (2005) AIP Publishing
- Figure 1.6b from Laraoui, A. et al. *Nature Communications* **2015**, *6*, 8954
under Creative Commons Attribution 4.0 (CC-BY 4.0) license
- Figure 4.3b reprinted with permission from Shao-Chi Yu
Copyright (2018) Shao-Chi Yu

Samuel T. Zimmermann

Education

- 2014–current **PhD in Microsystems and Microelectronics**, EPFL, Lausanne.
2012–2013 **MSc in Materials Science**, ETH, Zurich.
2008–2012 **BSc in Materials Science**, ETH, Zurich.

Master Thesis

- Title *Crack Formation in Aluminosilicate Ceramic Foams*
Supervisors Dr. Philip Sturzenegger (*deCavis AG*), Prof. Joerg F. Löffler

Bachelor thesis

- Title *Electro-chemical Characterization of Yttria-Stabilized Zirconia Micro-Solid Oxide Fuel Cells*
Supervisors Dr. Anna Evans (*Nonmetallic Inorganic Materials, ETH*), Prof. Ludwig J. Gauckler

Experience

- 2013-2014 **Internship (6 months)**, *Organic Functional Materials, Imperial College*, London.
Solution Processing of P(VDF-TrFE)-P₃HT Hetero-Structures for Organic Memory Devices
- 2013 **Lab Assistance**, *Nanometallurgy Laboratory, ETH*, Zurich.
Development of an Automated Visual Crack Detection System for Cyclic Stress Testing
- 2006-2007 **Process Operator Decorative Coatings**, *W. Bloesch AG*, Grenchen.
Development and Production of Decorative PVD Coatings for the Watch Industry
- 2005-2006 **Military Service**, *Group Leader in Medical Troops, Scuole San 42, Airolo*.
Long-Term Service Terminated as Group Leader in Medical Training

Publications

- 2017 S.T. Zimmermann, D.W.R. Balkenende, A. Lavrenova, Ch. Weder, and J. Brugger. Nanopatterning of a stimuli-responsive fluorescent supramolecular polymer by thermal scanning probe lithography. *ACS Applied Materials and Interfaces*, 9, 2017.
- 2015 T. Lenz, D. Zhao, G. Richardson, I. Katsouras, K. Asadi, G. Glasser, S.T. Zimmermann, N. Stingelin, W.S.Ch. Roelofs, M. Kemerink, Blom P.W.M., and D.M. de Leeuw. Microstructured organic ferroelectric thin film capacitors by solution micromolding. *Pysica Status Solidi A*, 212, 2015.

Avenue de Florissant 9 – 1009 Prilly – Switzerland

☎ +41 (0)79 888 3138 • ✉ samuel.zimmermann@protonmail.com
🐦 samtzimmer

Languages

German Native Language
English Fluent
French Intermediate

Computer skills

OS Debian Linux, MS Windows
Software Libre Office, MS Office, RStudio, Inkscape, GIMP, Blender, Gwyddion, FEniCS, Gmsh, LabView, SolidWorks, COMSOL
Languages Python, HTML

